MECHANICAL BEHAVIOR OF SMALL-SCALE CHANNELS IN ACID-ETCHED FRACTURES

A Dissertation

by

JIAYAO DENG

Submitted to the Office of Graduate Studies of
Texas A&M University
in partial fulfillment of the requirements for the degree of

DOCTOR OF PHILOSOPHY

December 2010

Major Subject: Petroleum Engineering

MECHANICAL BEHAVIOR OF SMALL-SCALE CHANNELS IN ACID-ETCHED FRACTURES

A Dissertation

by

JIAYAO DENG

Submitted to the Office of Graduate Studies of
Texas A&M University
in partial fulfillment of the requirements for the degree of

DOCTOR OF PHILOSOPHY

Approved by:

Co-Chairs of Committee,	A. Daniel Hill
	Ding Zhu
Committee Members,	Ahmad Ghassemi
	Amine A. Benzerga
Head of Department,	Stephen A. Holditch

December 2010

Major Subject: Petroleum Engineering

ABSTRACT

Mechanical Behavior of Small-Channels in Acid-etched Fractures. (December 2010)

Jiayao Deng, B.S., Tsinghua University, Beijing, China;

M.S., Tsinghua University, Beijing, China

Co-Chairs of Advisory Committee: Dr. A. Daniel Hill
Dr. Ding Zhu

The conductivity of acid-etched fractures highly depends on spaces along the fracture created by uneven etching of the fracture walls remaining open after fracture closure. Formation heterogeneities such as variations of mineralogy and permeability result in channels that contribute significantly to the fracture conductivity. Current numerical simulators or empirical correlations do not account for this channeling characteristic because of the scale limitations. The purpose of this study is to develop new correlations for conductivity of acid-etched fracturing at the intermediate scale. The new correlations close the gap between laboratory scale measurements and macro scale acid fracture models.

Beginning with acid-etched fracture width profiles and conductivity at zero closure stress obtained by the previous work, I modeled the deformation of the fracture surfaces as closure stress is applied to the fracture. At any cross-section along the fracture, I approximated the fracture shape as being a series of elliptical openings. With the assumption of elastic behavior for the rock, the numerical simulation presents how many elliptical openings remain open and their sizes as a function of the applied stress.

The sections of the fracture that are closed are assigned a conductivity because of small-scale roughness features using a correlation obtained from laboratory measurements of acid fracture conductivity as a function of closure stress. The overall conductivity of the fracture is then obtained by numerically modeling the flow through this heterogeneous system.

The statistical parameters of permeability distribution and the mineralogy distribution, and Young's modulus are the primary aspects that affect the overall conductivity in acid-etched fracturing. A large number of deep, narrow channels through the entire fracture leads to high conductivity when the rock is strong enough to resist closure stress effectively. Based on extensive numerical experiments, I developed the new correlations in three categories to predict the fracture conductivity after closure. Essentially, they are the exponential functions that incorporate the influential parameters. Combined with the correlations for conductivity at zero closure stress from previous work, the new correlations are applicable to a wide range of situations.

DEDICATION

To my parents, sister, wife and daughter

ACKNOWLEDGEMENTS

I would like to express my deepest gratitude to my advisors, Dr. A. Daniel Hill and Dr. Ding Zhu, for their guidance and support throughout the course of this research. As well, I would like to extend my appreciation to Dr. Ahmad Ghassemi and Dr. Amine A. Benzerga for serving as my committee members.

Thanks also go to my colleagues in our research group: Jianye Mou, Maysam Pournik, Luis Antelo, and Cassandra Beatty. I also want to thank my friends and the department faculty and staff for making my time at Texas A&M University a great experience. I would like to acknowledge the financial support from the acid fracturing conductivity JIP and the Crisman Institute in the Harold Vance Department of Petroleum Engineering of Texas A&M University.

Finally, thanks to my mother and father for their encouragement and to my wife for her patience and love.

NOMENCLATURE

a	Major radius of ellipse, L, in. [m]
$\bar{a}$	Average crack half-length, L, in. [m]
A_a	Crack area, L^2, m^2
A	Area of fracture surface, L^2, m^2
A_c	Contact area of fracture surface, L^2, m^2
b	Minor radius of ellipse, L^2, m^2
c	Focus of ellipse, L, in. [m]
c_s	Stress correction factor
E	Young's modulus, m/Lt^2, psi [Pa]
$f_{\text{limestone}}$	Percentage of limestone
F	Body force per unit mass, L/t^2, N/kg
G	Shear modulus, m/Lt^2, psi [Pa]
h	Grid height, L, m
h_a	Asperity height, L, m
h_f	Fracture height, L, in. [m]
k_f	Fracture permeability, L^2, md [m^2]
K	Kurtosis of asperity height distribution
l	Element half-length, L, in. [m]
L	Entire length of cross-section, L, in. [m]
m	Constant

M	Root mean square of asperity height distribution
N	Number of data points
n	Number of cracks
$n(h_a)$	Asperity height distribution function
p	Pressure, m/Lt^2, psi [Pa]
P	Load, m/t^2, Pa-m
q	Flow rate, L^3/t, m^3/s
Q	Total elastic energy, m/Lt^2, Pa
S_{RE}	Rock embedment strength, m/Lt^2, psi [Pa]
T	Transmissivity, L^4, m^4
u	Displacement, L, in. [m]
U	Airy stress function
U_n	Strain energy without crack, mL/t^2, N
U_T	Total strain energy, mL/t^2, N
v	Displacement, L, in. [m]
$\bar{v}$	Average crack closure, L, in. [m]
v_f	Fracture deformation, L, m
V	Acid volume, L^3, $in.^3$
w	Fracture width, L, in. [m]
w_i	Ideal fracture width, L, in. [m]
w_0	Initial fracture width, L, in. [m]
$\overline{w}$	Average fracture width, L, in. [m]

wk_f	Fracture conductivity, L^3, md-ft [m^3]
$(wk_f)_0$	Initial fracture conductivity under zero closure stress, L^3, md-ft
$(wk_f)_{ideal}$	Ideal fracture conductivity, L^3, md-ft [m^3]
x_f	Fracture half-length, L, in.
X	Volumetric dissolving power of acid
z	Individual data point
α	Constant
α_c	Contact ratio
β	Constant
γ	Angle, radian, semivariogram
δ	Additional deformation, L, in. [m]
$\bar{\delta}$	Average additional deformation, L, in. [m]
ε	Strain component
η	Elliptical coordinate
κ	Muskhelishvili's coefficient
μ	Fluid viscosity, m/Lt, cp [Pa-s]
ν	Poisson's ratio
ξ	Elliptical coordinate
$\xi(z)$	Potential function
π	Constant
ρ	Density, m/L^3, kg/m^3

σ	Standard deviation of asperity height distribution
σ_0	Initial closure stress, m/Lt^2, psi [Pa]
σ_c	Closure stress, m/Lt^2, psi [Pa]
σ_e	Effective modulus of asperity, m/Lt^2, psi [Pa]
σ_Y	Rock yield stress, m/Lt^2, psi [Pa]
σ^∞	Far-field stress, m/Lt^2, Pa
τ	Stress component, m/Lt^2, Pa
ϕ	Porosity
$\phi(z)$	Potential function
$\varphi(z)$	Potential function
ω	Analytical function for coordinate transformation

TABLE OF CONTENTS

Page

Page

LIST OF FIGURES

Page

Page

Page

Page

Page

LIST OF TABLES

Page

CHAPTER I

INTRODUCTION

1.1 Background

Acid fracturing is one of the widely used techniques for stimulating well production. It is an alternative to proppant fracturing for limestone or dolomite formations. The purpose of acid fracturing is to bypass a damaged zone around the wellbore and/or stimulate an undamaged formation by altering the flow pattern. This technique has been a successful stimulation technique in oilfields for more than 60 years (Kalfayan, L.J, 2007).

In an acid fracturing treatment, either acid alone is injected into the formation at a high rate, or the acid is preceded by a pad fluid (usually a viscous fluid). The fracture will be short and narrow without a pad fluid because the rate of fluid loss for acid is high. A treatment with a viscous pad fluid prior to the acid is more widely used under normal circumstances. A pad fluid is injected into the formation at pressure built up above the breakdown pressure of the formation. This pressure overcomes compressive earth stresses and the rock's tensile strength to create a hydraulic fracture. Then plain acid, gelled acid, foamed acid, or emulsion containing acid is injected into the fracture to react with the formation. The acid reacts nonuniformly with the fracture walls so that the

---

This dissertation follows the style of *SPE Journal*.

fracture props itself open after closure with the relatively undissolved regions acting as pillars that leave more dissolved regions as open channels. When the injection pressure is withdrawn, the fracture is subjected to the force attempting to close the fracture. The uneven etching along the fracture walls yields the lasting conductivity after closure (Ruffet et al., 1997).

Success of acid fracturing highly depends on the resulting conductivity that is a measure of capacity for fluid flow through an acid-etching fracture. Flow channels created by the acid differentially etching mainly contribute to the fracture conductivity. Thus, the conductivity of the acid fracture is affected by the volume of rock dissolution, the etching pattern, the rock strength, and the closure stress on the fracture. In order to obtain sufficient conductivity after closure, we need to have an adequate amount of rock dissolution and the flow channels as a result of uneven reaction with the rock surface or preferential reaction with minerals heterogeneously placed in the formation. The rock needs to be strong to sustain the closure stress and prevent the channel closure. The carbonate formation with very soft rock is not a good candidate for acid fracturing. The closure stress is a function of the depth. The acid fracture in the shallow formation gives higher conductivity than in a deep one.

In order to design an acid fracturing treatment precisely, a model that can simulate each step of acid fracturing and predict the conductivity is necessary. A good acid fracturing model must be able to describe the fracture geometry and the etching pattern with different acid types, injection conditions and formation characteristics like permeability and lithology. After the acid treatment, the model must incorporate the

mechanical behavior of the fracture under closure stress, determine the channels remaining open, and evaluate the fluid flow capacity through the fracture.

The fracturing process with a pad injection is identical to that employed with proppant fracturing. By using the standard hydraulic fracturing theory, including analytical or numerical calculations, we can determine the fracture geometry as a function of the injection rate and time. The etching pattern is much more difficult to design because the rock dissolution is significantly affected by the leakoff behavior and the rock heterogeneity. The prediction of conductivity is not easy to achieve as well. The etching pattern, rock properties, and closure stress are the major factors that influence largely the conductivity of an acid-etched fracture.

Many researchers (Williams and Nierode, 1972; Nierode et al., 1972; van Domselaar et al., 1973; Coulter et al., 1974; Roberts and Guin, 1975) have studied the fracturing process and acid reaction. Most of them have emphasized on the fracture geometry and the acid penetration distance rather than the fracture conductivity. In industry, some conductivity correlations (Nierode and Kruk, 1973; Williams et al., 1979) founded on laboratory measurements are used to design the acid fracturing treatments based on the experience with the similar formations. Currently, neither a definite mechanism to optimize the conductivity nor an accurate conductivity model exists for the acid-etched fracture.

1.2 Literature Review

Hydraulic fracturing is one of the primary stimulation methods for improving well productivity. For a carbonate formation, two main kinds of hydraulic fracturing exist: proppant fracturing and acid fracturing. Proppant fracturing has been studied for a long time and used widely. This project will focus on acid fracturing. By its own nature, the success of acid fracturing depends on heterogeneous dissolution created by acid. Uneven etching is the main mechanism for maintaining the fracture open to generate conductivity. The objectives of this research are to investigate the effects of mechanical behavior during fracture closure numerically, calculate conductivity that influences acid fracture performance, and develop new conductivity correlations for industrial use. This section will review the literature on these three aspects.

1.2.1 Fracture Closure Models

The first part of this project is to model the closure behavior of acid fractures. I can simplify this process as two rough surfaces coming into contact. Many researchers have developed numerical models to describe fracture closure behavior.

Gangi (1978) proposed his "bed of nails" model (**Fig. 1.1**) to study fracture permeability variation with pressure. He chose the rod-shaped asperities for the model and assumed the height distribution of asperities satisfying a simple power-law variation. Hopkins (1990) developed another similar model, in which the asperities were treated as columns with circular cross-sections. He used the Boussinesq solution to calculate the deformation around the circular contact area and employed Hooke's law for a column to

obtain the deformation of the asperity. Cook (1992) pointed out that the deformation under normal stress of the void space (apertures) adjacent to the asperities was necessary to take into account in addition to the deformation of asperities themselves. Other than the asperities and apertures, the process should include the deformation of the rock matrix near the fracture as well. From Hopkins' model, Lee and Harrison (2001) developed a method that considered both asperity compression and half-space deformation. They also determined the parameters in the empirical equations using nonlinear regression. Although they assume elastic behavior, their model seems appropriate for the nonlinear fracture closure process.

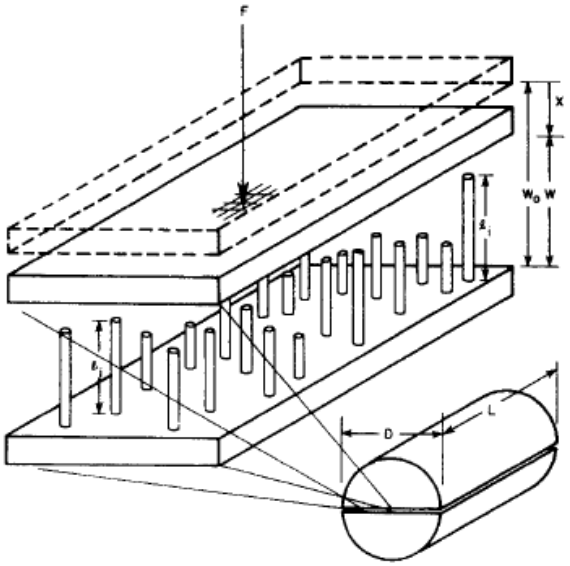

Fig. 1.1—"Bed of nails" model. (From Gangi.)

Another conceptual model proposed by Greenwood and Williamson (1966) treated the fracture surface as a rough elastic surface and used Hertzian contact theory to

analyze the deformation of asperities. They investigated a single fracture surface and showed that the contact deformation depends on the topography of the surface and provided a criterion that indicates whether contact will be elastic or plastic. The surface density of the asperities, the standard deviation of their height distribution, and their mean radius are three topographic properties controlling the contact deformation. Swan (1983) developed a discrete numerical technique to examine the mechanical behavior of a number of different slate fractures. He showed that the peak heights of asperities followed a Gaussian distribution. Brown and Scholz (1985) extended models above for two random, nominally flat elastic surfaces. They pointed out that the deformation depended as much on the details of the surface topography as on the elastic properties of the material. Malama and Kulatilake (2003) derived a new semi-empirical model that can be used to predict fracture deformation behavior under normal compression. Compared with the other available asperity models, the modified exponential model proposed by Malama and Kulatilake (2003) provided the best fit to the experimental data.

The aperture model is an alternative to the asperity model mentioned above. Myer (2000) idealized the noncontacting region by cracks and described the deformation of cracks arranged in simple 2D geometries analytically. Usually, a crack is a very thin elliptical hole when the major axis is much bigger than the minor one. In his model, a collection of cracks, instead of a collection of asperities, represented a fracture (**Fig. 1.2**). The comparison indicated that crack models and asperity models were generally equivalent in capturing the volumetric deformation of the void space in a fracture.

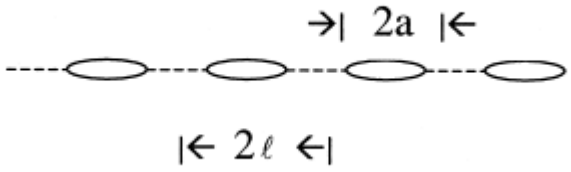

Fig. 1.2—Idealization of fracture by coplanar array of cracks. (From Myer.)

In this project, the laboratory will provide the data that are obtained by scanning the fracture surfaces. To use asperity models, I need to describe the different kinds of data by a certain distribution, which is not easy to identify. Therefore, the simple crack models developed by Myer (2000) are more suitable for my project.

1.2.2 Conductivity Calculation Methodology

The second part of this project is to calculate the conductivity of the closed fracture. In other words, I am going to do the research on fluid flow through two contacting rough surfaces. According to the fundamentals of fluid mechanics, Navier-Stokes equations govern fluid flow in a fracture. In practice, the Navier-Stokes equations have been simplified to more tractable equations, which have been studied by many researchers.

In the steady state, the Navier-Stokes equations can be simplified without considering the gravity effect. Zimmerman and Bodvarsson (1996) solved these equations exactly for a simple case, in which the fracture consisted of two smooth,

parallel walls separated by a uniform aperture. They showed that the permeability of the fracture can be identified as,

$$k_f = \frac{w^2}{12}, \tag{1.1}$$

where w is the fracture width in meter, and k_f is the permeability of the fracture in m^2. They also suggested that the transmissivity is the product of the permeability and area. The well known cubic law represents this relationship,

$$T = k_f A = \frac{h_f w^3}{12}, \tag{1.2}$$

where A is the cross-sectional area in m^2, h is the fracture height in meter, and T is the transmissivity in m^4. In practice, two smooth, parallel walls cannot represent real fracture surfaces, so this model is not accurate enough for a whole fracture.

By definition, conductivity is the product of the fracture permeability and fracture width. It doesn't account for the fracture height. Thus, the cubic law is often written in the form of,

$$wk_f = \frac{w^3}{12}, \tag{1.3}$$

where wk_f is the conductivity in m^3.

The Stokes equations provide another option that derives from the Navier-Stokes equations by ignoring the advective acceleration terms. Many approaches have tried to solve the Stokes equations. One of them was Skjetne et al. (1999) that conducted numerical simulations of flow through simulated fracture apertures. The results showed that flow rate was linear to pressure gradient.

The Stokes equations can be reduced even further to the Reynolds lubrication equation (or Reynolds equation), which requires that the fluctuations of apertures cannot be too rough. However, this simplification is inadequate for fracture flow. Yeo et al. (1998) used the finite element method to solve the Reynolds equation and found that it over predicted the conductivity by 40 to 100%.

Although the cubic law is not suitable at the scale of a single fracture, it holds locally when fluid flows through the subdivided or local fracture voids (Walsh, 1981). This model is referred to as the local cubic-law (LCL) that represents the state of the art for fluid flow simulation in a fracture. Brush and Thomson (2003) created synthetic rough walls to simulate fluid flow through them. By comparison with the Navier-Stokes equations, Stokes equations, and the local cubic-law, they found that the local cubic-law was an acceptable approximation to the Navier-Stokes equations. But Konzuk and Kueper (2004) pointed out that the local cubic-law still over predicted the observed flow rate. It required more investigation into the effect of fracture surface undulation and other causes of abrupt aperture change.

The local cubic-law is our choice to calculate the conductivity in this project, because it represents the state of the art for fluid flow simulation. More importantly, it is feasible according to our computational ability. I believe that the conductivity is proportional to the cube of the aperture in our small scale grids, especially when our grid blocks of simulations are fine enough.

1.2.3 Conductivity Correlations

The final goal of the project is to develop a correlation to estimate the conductivity for an acid fracture at the intermediate scale. The conductivity prediction is difficult because it is a function of the rock strength, heterogeneities present in the rock, the transportation and dissolution of acid, the closure stress, and other variables.

One estimate of the conductivity (Williams et al., 1979) assumed that the fracture walls are uniformly dissolved, leaving an open channel of width, w, defined by,

$$w = \frac{XV}{2x_f h_f (1-\phi)}, \tag{1.4}$$

where X is the acid dissolving power, V is the total volume of acid injected, x_f is the acid penetration distance (i.e. the fracture half-length), h_f is the fracture height, and ϕ is the formation porosity. Therefore, the ideal fracture conductivity is proportional to the cubic power of the channel width,

$$(wk_f)_{ideal} = 7.8\times10^{12}\left(\frac{w}{12}\right)^3, \tag{1.5}$$

where w is the channel width in inch, $(wk_f)_{ideal}$ is the ideal fracture conductivity in md-ft. This approach overestimates the conductivity observed in laboratory, primarily because it doesn't take the closure stress into account.

Nierode and Kruk (1973) developed an empirical correlation for fracture conductivity, which is widely used in industry. At a small scale, they conducted a series of experiments on different rocks acidized by HCl acid. In this experiment-base correlation, the conductivity is a function of rock dissolution, rock strength, and closure stress,

$$wk_f = \alpha \exp(-\beta\sigma_c), \tag{1.6a}$$

$$\alpha = 0.1703 DREC^{0.822}, \tag{1.6b}$$

$$\beta = \begin{cases} (13.9 - 1.3\ln S_{RE}) \times 10^{-3}, \text{ for } 0 < S_{RE} < 20{,}000\, psi \\ (3.8 - 0.28\ln S_{RE}) \times 10^{-3}, \text{ for } 20{,}000 \le S_{RE} \le 500{,}000\, psi \end{cases}, \tag{1.6c}$$

where σ_c is the closure stress in psi, *DREC* is the dissolved rock equivalent conductivity in md-ft, S_{RE} is the rock embedment strength in psi, and wk_f is the conductivity in md-ft. Rock embedment strength, S_{RE}, is a parameter representing the rock strength, which defined as "the force required to push a steel ball bearing into a rock surface to a distance equal to radius of the ball, divided by the projected area of the bearing". Compared with the original publication, the correlation presented here has two differences. The first one is the constant of Eq. 1.6b is 0.1703 instead of 0.265 in the original publication, because the unit for wk_f and *DREC* is md-ft, which is more popular than md-in used originally. The other one is a typographical error occurring in the equation presented here as Eq. 1.6c. The value 13.9 given here is the correct constant rather than 19.9 in the original publication. Although the correlation includes the effect of closure stress, the author ignored the effect of acid leak-off and etching pattern on conductivity. The authors claim that the correlation can predict the lower bound on fracture conductivity.

In order to calculate the dissolved rock equivalent conductivity, *DREC*, I apply the cubic law (Eq. 1.3) directly. The unit conversion results in the different constant, α, in Eq. 1.7. Gong (1997) presented the derivation in Appendix A of his dissertation. In this case,

$$\alpha = 1.47 \times 10^{7} w^{2.466}, \tag{1.7}$$

where *w* is the fracture width in inch. Gomaa and Nasr-El-Din (2009) suggested another expression for *DREC* by material balance after the acid concentration profile was predicted. It is,

$$DREC = 3.11 \times 10^{7} w^{3}, \tag{1.8}$$

where *DREC* presented here is in md-ft instead of md-in in original publication. Substitution into Eq. 1.6b leads to,

$$\alpha = 2.46 \times 10^{5} w^{2.466}, \tag{1.9}$$

where *w* is in inch.

Nasr-El-Din et al. (2008) pointed out the correlation developed by Nierode and Kruk (1973) were lumped together and not separated by lithology. They graphed and evaluated the data again as a lumped set and as individual sets by lithology. The modified correlations kept the same form as the original ones, but made the constants different. The lumped set has the expression as,

$$wk_f = \alpha \exp(-\beta \sigma_c), \tag{1.10a}$$

$$\alpha = 0.5205 DREC^{0.7518}, \tag{1.10b}$$

$$\beta = \begin{cases} (22.463 - 2.193 \ln S_{RE}) \times 10^{-3}, \text{ for } 0 < S_{RE} < 20{,}000\, psi \\ (1.9606 - 0.1056 \ln S_{RE}) \times 10^{-3}, \text{ for } 20{,}000 \le S_{RE} \le 500{,}000\, psi \end{cases}. \tag{1.10c}$$

The correlations pertaining to limestone are,

$$wk_f = \alpha \exp(-\beta \sigma_c), \tag{1.11a}$$

$$\alpha = 0.121 DREC^{0.8746}, \tag{1.11b}$$

$$\beta = \begin{cases} \left(26.567 - 8.6341 \ln S_{RE}\right) \times 10^{-3}, \text{ for } 0 < S_{RE} < 20{,}000\, psi \\ \left(2.9795 - 0.202 \ln S_{RE}\right) \times 10^{-3}, \text{ for } 20{,}000 \le S_{RE} \le 500{,}000\, psi \end{cases}. \tag{1.11c}$$

The correlations pertaining to dolomite are,

$$wk_f = \alpha \exp\left(-\beta \sigma_c\right), \tag{1.12a}$$

$$\alpha = 4.44 DREC^{0.5592}, \tag{1.12b}$$

$$\beta = \begin{cases} \left(8.6383 - 0.7479 \ln S_{RE}\right) \times 10^{-3}, \text{ for } 0 < S_{RE} < 20{,}000\, psi \\ \left(2.3147 - 0.1513 \ln S_{RE}\right) \times 10^{-3}, \text{ for } 20{,}000 \le S_{RE} \le 500{,}000\, psi \end{cases}. \tag{1.12c}$$

In the equations above, wk_f and $DREC$ are all in md-ft. That is the reason why the constants in the expressions of α are different from the original publication.

Pournik (2008) developed another correlation following the same form of the Nierode and Kruk's correlation (Eq. 1.6a). The differences are the description of the constants, α and β. The lithology in his experiments consists of two kinds of rock, limestone and dolomite. The constant, β, is defined as,

$$\beta = -0.0063 + 0.000664 \ln\left(S_{RE}\right). \tag{1.13}$$

The other constant, α, is defined differently relying on the type of rock. For limestone,

$$\alpha = \frac{a_1 \overline{w}^3 \alpha_c}{12}, \tag{1.14}$$

where a_1=0.32, $\bar{w}$ is the average fracture width before closure in inch, α_c is the contact ratio before closure in fraction. In this case, the rock embedment strength, S_{RE}, is in the range between 30,000 and 35,000 psi. For dolomite,

$$\alpha = \frac{\bar{w}^{a_1}}{12}, \tag{1.15}$$

where a_1=3.78. The rock embedment strength, S_{RE}, is around 60,000 psi in this case.

Besides the correlations based on experiments, several researchers have derived some theoretical expressions to predict the fracture conductivity for certain stochastic distributions of asperity height. By using a "bed of nails" model (Fig. 1.1), Gangi (1978) developed a correlation to estimate the fracture permeability with closure stress. The model assumed a simple power-law variation for the asperity height distribution. The product of the fracture permeability and fracture width leads to the conductivity presented as,

$$wk_f = \left(wk_f\right)_0 \left[1 - \left(\frac{\sigma_c}{\sigma_e}\right)^m\right]^3, \tag{1.16}$$

where σ_e is the effective modulus of the asperities defined as,

$$\sigma_e = E\alpha_c = E\frac{A_c}{A}. \tag{1.17}$$

In the expressions above, m is a constant ($0<m<1$) which characterizes the distribution function of the asperity heights, $\alpha_c(=A_c/A)$ is the contact ratio of the fracture surfaces, and E is Young's modulus for the rock. This theoretical correlation showed good agreement with several experimental data on fractured carbonate rocks. However,

the requirement of asperity height distribution is not realistic. The universality of the power-law distribution functions needs further investigation.

Walsh (1981) suggested that 2D heat flow in a medium with constant conductivity was entirely analogous to laminar flow of an incompressible fluid. By this analogy, the author found the conductivity for a fracture where the surfaces have approximately random surface topography by the following equation,

$$wk_f = \left(wk_f\right)_0 \left[1 - \frac{\sqrt{2}M}{w_0} \ln\left(\frac{\sigma_c}{\sigma_0}\right)_e\right]^3, \qquad (1.18)$$

where M is the root mean square of asperity height distribution, w_0 is the initial fracture width under initial closure stress, σ_0, and subscript e refers to effective pressure that is the combination of applied stress and pore pressure. Walsh described the conductivity with respect to the effective pressure, the effect of aperture, and the effect of flow path tortuosity. But for acid fracturing treatment, the initial condition, which is the condition after acid injection but before fracture closure, is not known in practice.

Following an earlier formulation by Walsh (1965), Tsang and Witherspoon (1981) used a dual-concept model, which encompassed a void deformation model for stress-normal closure behavior and a distributed asperity model. The authors used a collection of flat voids between contacting asperities to represent a fracture. The closure behavior results from the deformation of these voids rather than the deformation of asperities as modeled by others. But this model also requires asperity height distribution. Once the roughness characteristics are available, the statistical average width is a

function of normal deformation and effective normal stress. Then the authors used the cubic law (Eq. 1.3) to calculate the fracture conductivity as,

$$wk_f = \frac{w^3}{12} = \frac{1}{12}\left[\frac{\int_0^{w_0-v_f}\left(w_0 - v_f - h_a\right)^3 n(h_a)dh_a}{\int_0^{w_0} n(h_a)dh_a}\right], \tag{1.19}$$

where w_0 is the maximum width at zero closure stress, v_f is the fracture deformation, h_a is the asperity height, and $n(h_a)$ is the asperity height distribution function. The unit of wk_f is m^3 if the SI unit applies in the expression above. The model showed good agreement with some experimental data. But it needs more efforts to investigate the key parameters extracted from the experiments.

By assuming an exponential distribution of asperity height and peak-to-peak contacts for the asperities, Swan (1983) developed another model to predict fracture conductivity. The expression is similar to the model of Walsh (1981). The contact area and the normal stiffness are proportional to the normal stress. Combining the roughness and closure behavior, the conductivity has the expression,

$$wk_f = \left(wk_f\right)_0\left[1 - \frac{\alpha}{w_0} - \frac{\sigma}{w_0}\ln\left(\sigma_c\right)\right]^2, \tag{1.20}$$

where α is a constant and σ is the standard deviation of the asperity heights. The parameters in this model need to be fixed by experimental data.

Gong et al. (1999) considered the effect of etching pattern and rock strength after acid treatment. The etching pattern is a strong function of acid contact time while acid leak-off doesn't play an important role. The correlation also takes the plastic deformation of asperities into account. Therefore, the conductivity prediction depends on

initial fracture conductivity, fracture wall roughness, rock yield stress, and closure stress as,

$$wk_f = \left(wk_f\right)_0 \left[1 - \frac{4+K}{5+K}\left(\frac{2\sigma_c}{c_s\sigma_Y}\right)^{1/(4+K)}\right]^6, \qquad (1.21)$$

where $(wk_f)_0$ is the initial fracture conductivity under no closure stress, K is the kurtosis of asperity height distribution, σ_Y is the rock yield stress, and c_s is the stress correction factor, which is empirically determined by roughness or asperity shape. In reality, this model is not easy to apply, because some of the parameters, such as surface roughness after acid injection and rock yield stress, are not attainable in field conditions.

Except for the empirical correlation by Nierode and Kruk (1973), other models mentioned above ask for the fracture topography as input. During an acid fracturing treatment, the instantaneous status of fracture surfaces after acidizing is nearly impossible to capture. In addition, the uneven distribution of the asperities on the fracture surface creates high permeable region. However, these open spaces do not uniformly spread out on the facture surfaces. In practice, connected void spaces between contacting asperities lead to channels. Some channels will keep open even under high closure stresses. Hakami and Larsson (1996) demonstrated this point of view by their experimental work on natural fractures. They pointed out all fractures exhibited "channeling" to some extent. Current correlations are not accurate enough to predict the fracture permeability, because further research on the "degree of channeling" is necessary.

1.3 Problem Description

During the procedure of acid fracturing, the fracture closure occurs after the fracture propagation. The fracture closure research in this dissertation is the second part of a project investigating acid fracture performance.

First of all, an introduction of the whole project is necessary. The success of acid fracturing depends upon heterogeneous dissolution along the fracture faces. Conductivity after fracture closure results from uneven etching, because asperities created by acid hold as pillars to keep a fracture open. Small channels or wormholes are likely to form to enhance production. Such features are sometimes seen in laboratory tests of acid fracture conductivity (Beg et al. 1998), but this is not common or easily repeatable because the breadth of the fracture in lab tests is typically only an inch or two. Meanwhile, this heterogeneity is unlikely to occur at the scale of typical acid fracture simulations, in which the length scale is much larger than the scale of the heterogeneities. Small channels or wormholes have the widths on the order from inches to a few feet. Therefore, the channels created by the acid can be predicted by modeling a fracture domain that is on the order of a few feet in extent in both height and length.

Current fracture models have a larger length scale than channels that are on the order of inches in breadth. So they must then extrapolate laboratory-based correlations of acid fracture conductivity, measured on samples that are a few inches in each direction, to the macro scale of the fracture propagation model. This modeling approach does not incorporate the effects of channeling on fracture conductivity or the larger scale stress

effects that result from rock removal in an acid fracture. Thus, current models are not good enough at estimating acid fracture performance accurately or effectively.

In this dissertation, I introduce an entirely new approach to acid fracture modeling that uses intermediate scale simulation of acid transport and dissolution, and rock elastic deformation under closure stress, to close the gap between laboratory scale measurements and macro scale acid fracture models. From extensive simulations, I develop a new correlation of acid fracture conductivity that takes the heterogeneous features into account. The new correlation is appropriate for a macro-scale fracture model. I also incorporate the effect of the rock removal along the fracture face on the local stress condition in the macro scale fracture model. Current models of the acid fracturing process do not include this major effect.

This modeling work consists of two parts. The first half is to model acid transport and heterogeneous dissolution at intermediate scale. Two rough surfaces are created at the end of this simulation. The second half, which is also my research topic in this proposal, is investigating the effects of in-situ stresses on the fracture closure behavior. After modeling the rock deformation, I calculate the conductivity of an acid fracture numerically. Based on extensive simulations, new empirical correlations of the acid fracture conductivity at intermediate scale are developed.

1.4 Objectives

The research work in this dissertation investigates mechanical effects on conductivity of acid-etched fractures at intermediate scale. It accomplishes the following objectives:

1. Simulating 2D elastic closure behavior of acid fractures and obtaining fracture width profile after closure.

2. Estimating conductivity numerically after acid-fracture closure by using the local cubic-law (LCL) and comparing results with the experimental data.

3. Developing a new set of conductivity correlations at intermediate scale to close the gap between laboratory scale measurements and macro scale acid fracture models.

CHAPTER II

ANALYTICAL MODELS OF ACID FRACTURE CLOSURE

Fracture surfaces etched by acid consist of two uneven walls. When they come into contact, the rock will deform under closure stress. It is difficult to understand the closure process directly and completely. So I started from a simple problem: an elliptical opening, known as a crack, in an infinite rock mass subject to closure stress. The analytical solution to the problem has been fully studied and derived. I can get a basic concept of the closure behavior for a single, small opening from the derivation.

In numerical simulation, an acid fracture is divided into a certain amount of cross-sections along the fracture length. **Fig. 2.1** shows a cross-section selected from an acid-etched fracture. Every cross-section has many small openings along the fracture height after some rock asperities touch. The openings interact with each other during the closure. The analytical solution to an elliptical opening is not precise enough to describe it. Therefore, I continue to study a scenario with elliptical openings in an infinite rock mass under closure stresses. The analytical solution will be derived and shown in this chapter.

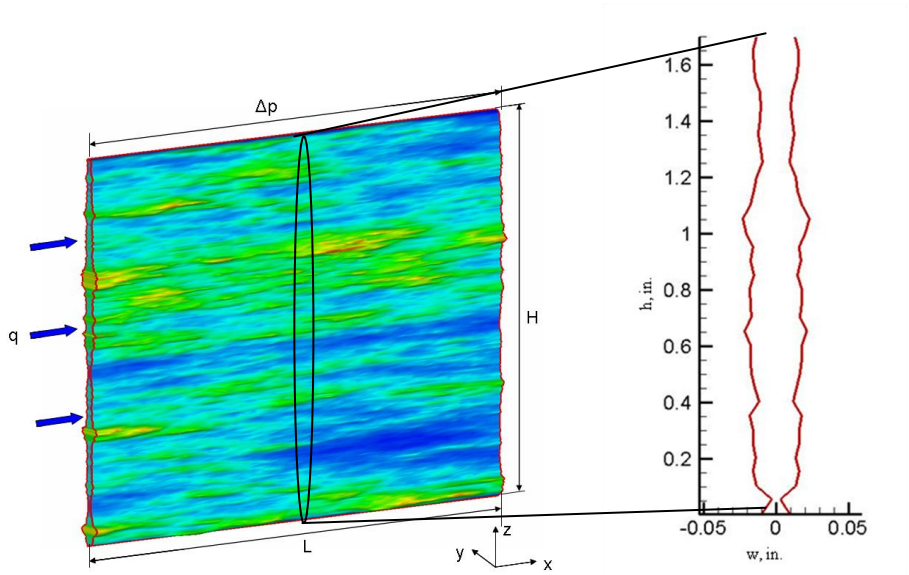

Fig. 2.1—A cross-section selected from an acid etched fracture.

By the approach of elliptical openings on every cross-section, I am able to investigate the closure behavior along the entire fracture. The deformation of the rock can be estimated. The openings under closure stresses contribute to the flow capacity of the fracture. Based on the model developed by Mou et al. (2007), the numerical calculation with the local cubic law gives the conductivity for the fracture after the width profile after closure is obtained.

In this chapter, I will introduce the methodology of the closure model and conductivity calculation.

2.1 Deformation of an Elliptical Opening

The closure behavior of a fracture can be analogous to the wellbore stability problem. Fjaer et al. (2008) presented the analytical solutions, which included the stress

and deformation distribution around the wellbore, to perform the stability analysis. However, the real fracture is never created as a cylinder like the wellbore. The cylinder will not be closed even under extremely high closure stresses unless the rock fails and it crushes. An ellipse cross-section fracture is more realistic than a circular one to describe the deformation of a fracture. Then I derived the analytical solution for the deformation of an elliptical opening in an infinite rock mass as follow.

Jaeger et al. (2007) presented the derivation of this analytical solution based on Airy stress function and complex variable method (Appendix A). I briefly review it below. I assume that the shape of fracture cross-section is an ellipse, which leads to a 2D problem, and consider a traction-free elliptical hole (**Fig. 2.2**) in an infinite rock mass with the major radius a and minor radius b. A far-field stress, σ^{∞}, acts in a direction rotated from the major axis Ox of the ellipse by an angle γ. Because the application of Cartesian or polar coordinates on elliptical problems is complex, the transformation from Cartesian coordinates, (x, y), to elliptical coordinates, (ξ, η), is necessary.

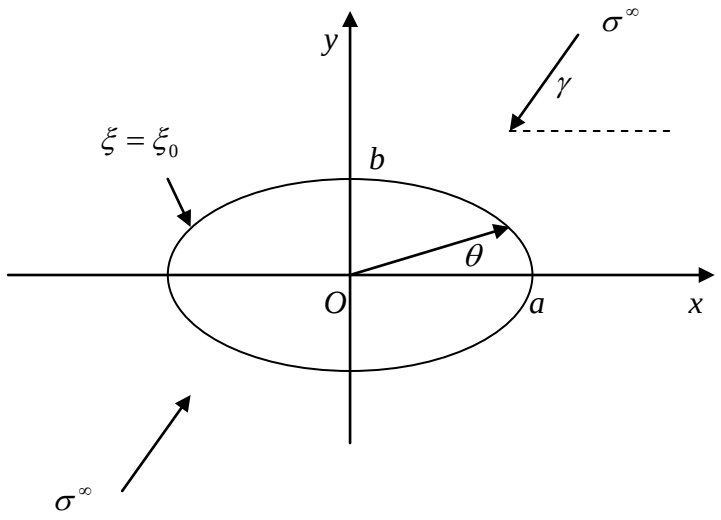

Fig. 2.2—An elliptical hole in an infinite rock mass. (From Jaeger et al.)

The definition of a transformation is,

$$z = \omega(\zeta), \tag{2.1}$$

where ω is an analytic function. This transformation maps points $\zeta = \xi + i\eta$ in the ζ-plane into points $z = x + iy$ in the *z*-plane. Consider the specific mapping as below,

$$z = x + iy = c\cosh\zeta = c\cosh(\xi + i\eta), \tag{2.2}$$

where *c* is the focus of the ellipse. Note that Eq. 2.2 is equivalent to Eq. 2.3,

$$x = c\cosh\xi\cos\eta\,,\ y = c\sinh\xi\sin\eta\,. \tag{2.3}$$

Notice that the curve in the *z*-plane that corresponds to $\xi = \xi_0$ satisfies the equation,

$$\frac{x^2}{(c\cosh\xi_0)^2} + \frac{y^2}{(c\sinh\xi_0)^2} = 1. \tag{2.4}$$

Therefore an ellipse having semiaxes,

$$a = c\cosh\xi_0,\ b = c\sinh\ \xi_0. \tag{2.5}$$

Based on the Airy stress function and complex variable method (Appendix A), the displacements in the new coordinates, u_ξ and u_η is,

$$2G\left(u_\xi + iu_\eta\right) = \left[\kappa\phi(z) - z\overline{\phi'(z)} - \overline{\psi(z)}\right]\left[\overline{\omega'(\zeta)}/\,\omega'(\zeta)\right]^{1/2}, \tag{2.6}$$

where G is the shear modulus, κ is Muskhelishvili's coefficient defined as,

$$\kappa = \begin{cases} 3-4\nu, \text{for plane strain} \\ \dfrac{3-\nu}{1+\nu}, \text{for plane stress} \end{cases}. \tag{2.7}$$

ν is Poisson's ratio in Eq. 2.7. Using the transformation, I can calculate the displacement in Cartesian coordinates,

$$2G(u+iv) = \kappa\phi(z) - z\overline{\phi'(z)} - \overline{\psi(z)}. \tag{2.8}$$

The potentials $\phi(z)$ and $\psi(z)$ (Maugis, 1992) that satisfy the stress boundary conditions are

$$4\phi(z) = \sigma^\infty c\left[e^{2(\xi_0+i\gamma)}\cosh\zeta + \left(1-e^{2(\xi_0+i\gamma)}\right)\sinh\ \zeta\right], \tag{2.9 a}$$

$$4\psi(z) = -\sigma^\infty c\left[\cosh 2\xi_0 - \cos 2\gamma + e^{2\xi_0}\sinh\ 2(\zeta-\xi_0-i\gamma)\right]/\sinh\ \zeta\,. \tag{2.9b}$$

I calculate the terms in Eq. 2.8,

$$\overline{\phi'(z)} = \frac{1}{4}\sigma^\infty\left\{e^{2\xi_0-2i\gamma} + \left(1-e^{2\xi_0-2i\gamma}\right)\coth(\xi-i\eta)\right\}. \tag{2.10}$$

Then,

$$
\begin{aligned}
&\kappa\phi(z) - z\overline{\phi'(z)} - \overline{\psi(z)} \\
&= \frac{1}{4}\sigma^{\infty} c \cosh(\xi + i\eta) e^{2\xi_0} (2i \sin(2\gamma)) + \frac{1}{4}\sigma^{\infty} c\left(1 - e^{2\xi_0 + 2i\gamma}\right) \sinh(\xi + i\eta) \\
&- \frac{1}{4}\sigma^{\infty} c\left(1 - e^{2\xi_0 - 2i\eta}\right) \alpha(\cosh(2\xi) + \cos(2\eta)) \sinh(\xi + i\eta) \\
&+ \frac{2}{4}\sigma^{\infty} c\alpha \sinh(\xi - i\eta)\left(\cosh(2\xi_0) - \cos(2\gamma) + e^{2\xi_0} \sinh 2(\xi - \xi_0 + i\eta - i\gamma)\right)
\end{aligned}
\quad , \tag{2.11}
$$

where $\alpha = (\cosh 2\xi - \cos 2\eta)^{-1}$.

Substitution of Eq. 2.11 into Eq. 2.8 yields the displacements in *x* and *y* directions, respectively. The displacement in *x* direction, *u*, is the real part of the solution, while the displacement in *y* direction, *v*, is the imaginary part.

$$
\begin{aligned}
u &= \mathrm{Re}\left[\frac{1}{2G}\left(\kappa\phi(z) - z\overline{\phi'(z)} - \overline{\psi(z)}\right)\right] \\
&= \frac{\sigma^{\infty} c}{8G[\cos(2\eta) - \cosh(2\xi)]} \{\cosh\xi [e^{2\xi_0} \kappa \sin\eta \cos(2\eta) \sin(2\gamma) \\
&+ e^{2\xi_0} \cos(2\gamma) \cos(2\eta) \cos\eta (\kappa - 1) \\
&- e^{2\xi_0} \cosh(2\xi)(\kappa \sin\eta \sin(2\gamma) + (\kappa - 1)\cos(2\gamma)\cos\eta) \\
&- 4e^{2\xi_0} \cos\gamma \cos^2\eta \sin\gamma \sin\eta - 2e^{2\xi_0} \sin\eta \cosh(2(\xi - \xi_0)) \sin(2(\eta - \gamma)) \\
&+ \cos\eta \sinh(2\xi) - e^{2\xi_0} \cos(2\gamma) \cos\eta \sinh(2\xi)] \\
&- \sinh\xi [-2\cos(2\gamma)\cos\eta - \kappa\cos(2\eta)\cos\eta \\
&+ e^{2\xi_0} \kappa \cos\eta \cos(2\eta) \cos(2\gamma) + 2\cosh(2\xi_0)\cos\eta \\
&+ (1 + \kappa) e^{2\xi_0} \cos(2\eta) \sin(2\gamma) \sin\eta - 2e^{2\xi_0} \cos(2\gamma) \sin^2\eta \cos\eta \\
&- \cosh(2\xi)[e^{2\xi_0}(1 + \kappa)\sin\eta \sin(2\gamma) + \kappa(-1 + e^{2\xi_0} \cos(2\gamma))\cos\eta] \\
&+ \sin\eta \sin(2\eta) + e^{2\xi_0} \sin\eta \sin(2\gamma) \sinh(2\xi) \\
&+ 2e^{2\xi_0} \cos(2(\eta - \gamma)) \cos\eta \sinh(2(\xi - \xi_0))]\}
\end{aligned}
\quad , \tag{2.12 a}
$$

$$
\begin{aligned}
v &= \mathrm{Im}\left[\frac{1}{2G}\left(\kappa\phi(z) - z\overline{\phi'(z)} - \overline{\psi(z)}\right)\right] \\
&= \frac{\sigma^{\infty} c}{8G\left[\cos(2\eta) - \cosh(2\xi)\right]}\Big\{-\sinh\xi\Big[e^{2\xi_0}\kappa\cos\eta\cos(2\eta)\sin(2\gamma) \\
&+ e^{2\xi_0}\cos(2\gamma)\cos(2\eta)\sin\eta(1-\kappa) \\
&- e^{2\xi_0}\cosh(2\xi)(\kappa\cos\eta\sin(2\gamma) - (\kappa-1)\cos(2\gamma)\sin\eta) \\
&+ e^{2\xi_0}\sin(2\gamma)\sin\eta\sin(2\eta) - 2e^{2\xi_0}\cos\eta\cosh(2(\xi-\xi_0))\sin(2(\eta-\gamma)) \\
&- \sin\eta\sinh(2\xi) + e^{2\xi_0}\cos(2\gamma)\sin\eta\sinh(2\xi)\Big] \\
&+ \cosh\xi\Big[e^{2\xi_0}\cos\eta\cos(2\eta)\sin(2\gamma)(1+\kappa) + 2\cos(2\gamma)\sin\eta \\
&- 2e^{2\xi_0}\cos(2\gamma)\cos^2\eta\sin\eta + \kappa\cos(2\eta)\sin\eta - e^{2\xi_0}\kappa\cos(2\gamma)\cos(2\eta)\sin\eta \\
&- 2\cosh(2\xi_0)\sin\eta \\
&- \cosh(2\xi)\Big[e^{2\xi_0}(1+\kappa)\cos\eta\sin(2\gamma) - \kappa\left(-1 + e^{2\xi_0}\cos(2\gamma)\right)\sin\eta\Big] \\
&+ \cos\eta\sin(2\eta) + e^{2\xi_0}\cos\eta\sin(2\gamma)\sinh(2\xi) \\
&- 2e^{2\xi_0}\cos(2(\eta-\gamma))\sin\eta\sinh(2(\xi-\xi_0))\Big\}
\end{aligned}
\qquad (2.12b)
$$

The most important case is that a far-field stress, σ^{∞}, acts perpendicular to the crack. With $\gamma = \pi/2$ and $\xi_0 = 0$ to represent a thin crack, the displacement at the surface of the crack is found by setting $\xi = \xi_0 = 0$, in which case $\zeta = i\eta$, $\cosh\zeta = \cos\eta = x/c$. By substituting all these conditions in to Eq. 2.12b, the normal displacement of the crack face is in the form of,

$$
v = \frac{(\kappa+1)\sigma^{\infty}}{4G}\left(a^2 - x^2\right)^{1/2}, \qquad (2.13)
$$

where I have made use of the fact that, for a thin crack, the focal distance *c* coincides with the crack half-length, *a*.

Generally, two in-situ stresses have effects on fracture closure: vertical (overburden) stress and horizontal (minimum) stress. For most cases, plane strain

condition will be valid because the dimension of fracture length is much larger than the dimension of fracture width. From Eq. 2.7, I have Muskhelishvili's coefficient, κ, for the plane strain condition. Once the elliptical hole is able to stay open, the superposition of normal displacement caused by each in-situ stress leads to the total displacement of the fracture surface. When $\gamma = 0$, $\xi = \xi_0$, and $\kappa = 3 - 4\nu$, the normal displacement caused by vertical stress is,

$$v_1 = -\frac{c(1-\nu)}{2G}\sigma_v \sin\eta \sinh\xi_0 . \tag{2.14}$$

When $\gamma = \frac{\pi}{2}$, $\xi = \xi_0$, and $\kappa = 3 - 4\nu$, the normal displacement caused by horizontal stress is,

$$v_2 = \frac{c(1-\nu)}{2G}\sigma_h \sin\eta(2\cosh\xi_0 + \sinh\xi_0). \tag{2.15}$$

The total normal displacement of the crack surface is the summation of Eq. 2.14 and Eq. 2.15, which leads to Eq. 2.16,

$$v = v_1 + v_2 = \frac{c(1-\nu)}{2G}\sin\eta(2\sigma_h \cosh\xi_0 + \sigma_h \sinh\xi_0 - \sigma_v \sinh\xi_0). \tag{2.16}$$

When considering a crack having a small but finite value of ξ_0, from Eq. 2.5, we can see that $b/a = \tanh\xi_0 \cong \xi_0$. So ξ_0 essentially represents the aspect ratio of the crack in its unstressed state.

For a crack, the major axis of the ellipse is much larger than the minor axis, so the vertical closure stress has much less effect on closure behavior than the horizontal

one. Therefore, the vertical stress is negligible. Eq. 2.13 is good enough to represent the displacement. From Eq. 2.4, the initial shape of the crack can be described by,

$$y = \xi_0 \left(a^2 - x^2\right)^{1/2}. \tag{2.17}$$

The crack will be fully close along its entire length when the displacement, *v*, calculated by Eq. 2.13 is equal to y in Eq. 2.17, which yields

$$\sigma^{\infty} = \frac{4G\xi_0}{\kappa + 1}. \tag{2.18}$$

For plane strain case, the pressure required to close a crack of initial aspect ratio ξ_0 is

$$\sigma^{\infty}(\text{closure}) = \frac{G\xi_0}{1-\nu}. \tag{2.19}$$

I use Eq. 2.19 to determine if the closure stress is big enough to close the ellipse. When the ellipse keeps open, Eq. 2.16 can give the normal displacement under closure stresses in both the vertical and horizontal directions.

2.2 Deformation of Elliptical Openings in Line

Apparently, a single ellipse is not able to represent a whole fracture, because the fracture surfaces are rough and many asperities will come into contact under certain closure stresses. For analytical purpose, I still consider one cross-section of a fracture, which means a 2D problem. Those contacting asperities separate the fracture into a collection of cracks with length much larger than width. Therefore, I will introduce the analytical solution (Myer, 2000) to calculate the deformation of cracks.

As shown in Fig. 1.2, a collection of coplanar cracks is subject to the far-field closure stress, σ_c. I investigate one of elements with one crack (**Fig. 2.3**), because the cracks distribute periodically. The total deformation at a large distance from the crack is ΔL. Compared to the element without crack, we observe an additional deformation called δ. Distribution of the additional deformation over the length of crack gives the average displacement of the crack surface, which is defined as the average crack closure, $\bar{v}$.

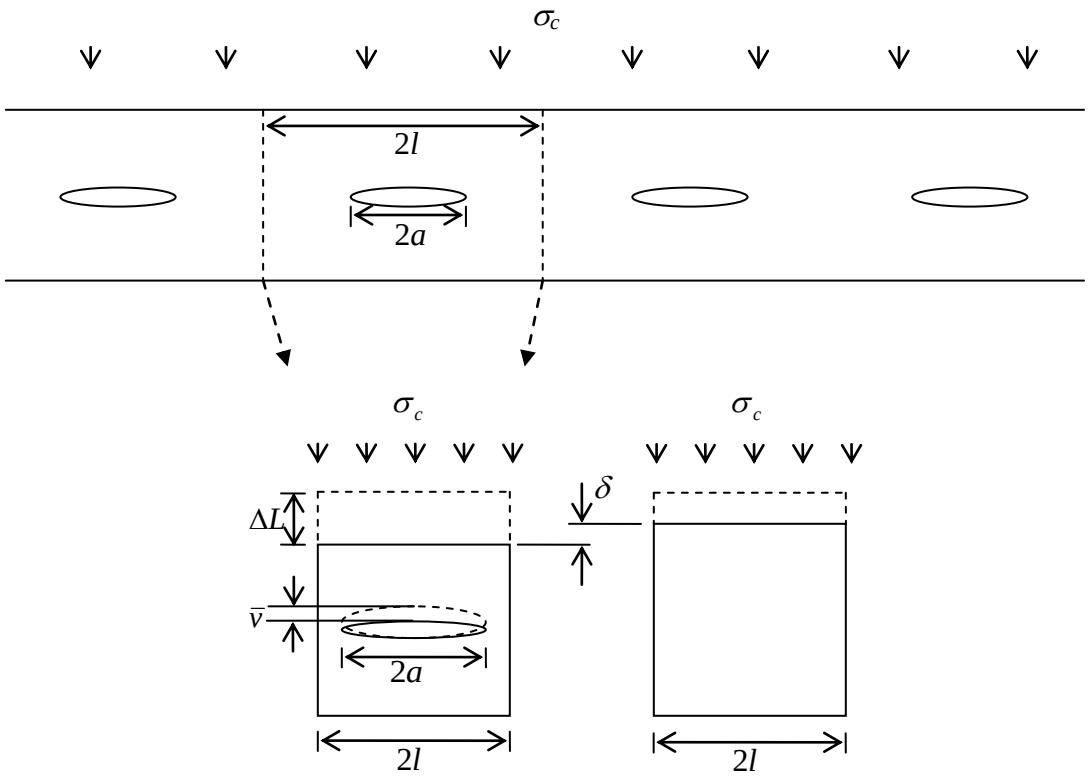

Fig. 2.3—Deformation of elemental volume with and without a crack. (After Myer.)

Myer (2000) presented the analytical solution to this problem. Appendix B provides a brief introduction about the strain energy method used to obtain the solution. The additional deformation, δ, because of the crack is,

$$\delta = \frac{-4\sigma_c l}{\pi G}(1-\nu)\left[\ln\left(\cos\frac{\pi a}{2l}\right)\right], \tag{2.20}$$

where G is the shear modulus, ν is Poisson's ratio, a is the half length of the crack, and l is the half length of the element. I do not use the absolute value of the cosine function as the original publication does. Because the crack length is always smaller than element length in my cases, the absolute value is not necessary in the expression.

If the element length is much larger than the crack length, which means the interaction between cracks is negligible, I rewrite Eq. 2.20 by taking the leading terms in the expansion of the trigonometric and natural logarithm functions,

$$\delta = \frac{\sigma_c(1-\nu)\pi a^2}{2Gl}. \tag{2.21}$$

By definition, δ is an additional displacement at a large distance from the cracks. In order to obtain the crack closure at the crack surface, I distribute the deformation over the crack length shown as,

$$\bar{v} = \frac{\Delta V}{2a} = \frac{2l\delta}{2a} = \frac{\sigma_c(1-\nu)\pi a}{2G}. \tag{2.22}$$

The closure behavior of the separate cracks in this case ought to be the same as the single elliptical hole deformation, because the interaction between cracks is negligible. I examine the similarity from Eq. 2.13. For plane strain condition, the crack closure in terms of the position, x, is,

$$v = \frac{(\kappa+1)\sigma^{\infty}}{4G}\left(a^2 - x^2\right)^{1/2} = \frac{(1-\nu)\sigma_c}{G}\left(a^2 - x^2\right)^{1/2}. \tag{2.23}$$

The average closure along the crack length is,

$$\bar{v} = \frac{\Delta V}{2a} = \frac{2\int_{-a}^{a} v\,dx}{2a} = \frac{\sigma_c(1-\nu)\pi a}{2G}. \tag{2.24}$$

Comparison of Eq. 2.22 and Eq. 2.24 leads to the same crack closure. It also validates the correctness of the solution to a collection of cracks.

The cracks caused by acid fracturing treatment are of varying sizes. In order to use the analytical solution, the average crack half-length, $\bar{a}$, is defined by,

$$\bar{a} = \frac{\sum_{i=1}^{n} a_i}{n}, \tag{2.25}$$

where n is the number of cracks over the entire length, L. Then the contact ratio, α_c, is,

$$\alpha_c = 1 - \frac{\sum_{i=1}^{n} 2a_i}{L}. \tag{2.26}$$

Rewriting Eq. 2.20 and Eq. 2.21 yields the average additional displacements, $\bar{\delta}$, in terms of average crack half-length and contact ratio,

$$\bar{\delta} = \frac{4\sigma_c \bar{a}}{\pi G}\frac{\nu - 1}{1-\alpha_c}\left\{\ln\left[\cos\frac{(1-\alpha_c)\pi}{2}\right]\right\}, \tag{2.27}$$

$$\bar{\delta} = \frac{\pi\sigma_c \bar{a}}{2G}(1-\nu)(1-\alpha_c). \tag{2.28}$$

Notice that the constant 2 in Eq. 2.26 or Eq. 2.28 is not seen in the equations originally published by Myer (2000). The author might make some mistake. My

derivation yields these 2's in the equations. Finally, I have the average crack closure with respect to contact ratio shown as,

$$\bar{v} = \frac{\bar{\delta}}{1-\alpha_c}. \tag{2.29}$$

The equation above is not rigorous for acid-etched fractures. But it is valid when the variations in crack size and spacing are small.

The deformation calculation for a collection of cracks is one of 2D aperture models. By comparison with the asperity models introduced in the literature review, Myer (2000) pointed out that the results were very close. The array of cracks can represent the fracture geometry. This crack model is basically equivalent to the asperity models in capturing the volumetric deformation of void space. Therefore, I will use this analytical 2D model to calculate fracture closure in this project.

2.3 Closure Behavior of an Acid Fracture

As mentioned previously, the analytical approach is on every cross-section along fracture surface. In order to demonstrate the method, I selected a typical cross-section from an experimental core sample. Pournik (2008) pumped acid between two dolomite rock samples. The acid treatment created surface roughness which was measured with a laser profilometer which scans the rock surface to obtain the fracture width distribution. **Fig. 2.4** shows the geometry for one cross-section of the rough surfaces. The fracture height is 1.7 inches of this cross-section, while the fracture width for this cross-section is

on the order of 10^{-2} inches. Notice that the scale of the *x*-axis is greatly exaggerated for demonstration. The fracture is subject to a closure stress of 3,000 psi.

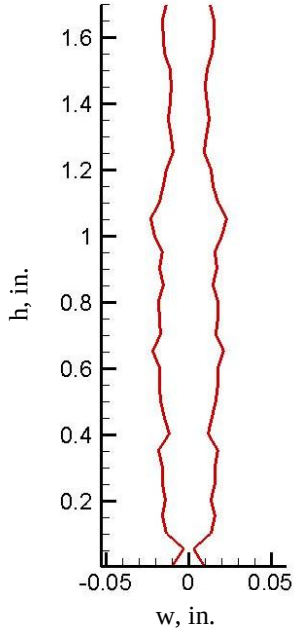

Fig. 2.4—Width profile of a fracture's cross-section.

The cross-section touches and deforms under the closure stress. First of all, I generate an ellipse to approximate the geometry of the cross-section (**Fig. 2.5**). The major axis of the ellipse is the fracture height while the minor axis is equal to the maximum fracture width. The problem becomes that an elliptical opening in an infinite rock mass is subject to a far-field stress. By using the Airy stress function and complex theory introduced in the previous section, the deformation for an ellipse has been solved analytically (Jaeger et al., 2007). According to Eq. 2.13, the normal closure of the elliptical face is found to be

$$\Delta w = \frac{(\kappa+1)\sigma_c}{2G}\left(a^2 - x^2\right)^{1/2}. \qquad (2.30)$$

For the consistency of the units, I define Δw as the closure, which is the same as v in Eq. 2.13. By applying the plane strain condition, the substitution of Eq. 2.7 in Eq. 2.30 yields

$$\Delta w = \frac{2(1-\nu)\sigma_c}{G}\left(a^2 - x^2\right)^{1/2}. \tag{2.31}$$

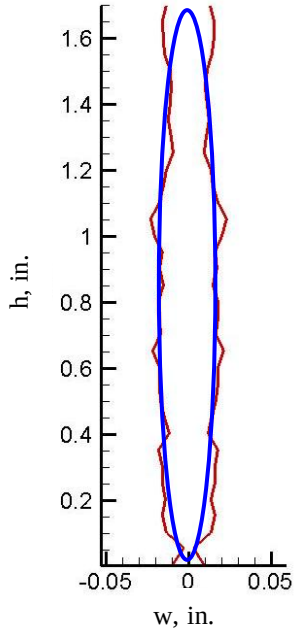

Fig. 2.5—Fracture's cross-section approximated by an ellipse.

Ideally, the ellipse keeps open under the closure stress if the closure obtained by Eq. 2.31 is smaller than the ellipse width. Subtracting the closure from the original width for each data point, ($w_i - \Delta w$), where i is 35 for this particular case, yields the width profile after the closure. But most likely, it is not the case. In Fig. 2.4, the fracture height is several hundred times larger than the fracture width. When the closure calculated by Eq. 2.31 exceeds the length of the ellipse minor axis, this ellipse tends to be closed along

its entire length. That happens commonly for most acid fracture cross-sections. Therefore, the narrowest points, which are the highest asperities, come into contact first and act as pillars to support the fracture (**Fig. 2.6**). The subtraction, ($w_i - w_{\min}$), leads to the new width profile for the next calculation step. By following the same procedure, I generate smaller ellipses to approximate the irregular shapes. However, Eq. 2.31 is not able to deal with multiple ellipses because they affect each other during the closure process.

Myer (2000) presented the analytical solutions for a collection of ellipses as introduced above. He idealized the noncontacting region by ellipses and described the deformation of ellipses by the strain energy method. The average ellipse closure with respect to contact ratio is obtained by Eq. 2.27,

$$\overline{\Delta w} = \frac{4\sigma_c \bar{a}}{\pi G} \frac{\nu - 1}{(1-\alpha_c)^2} \left\{ \ln\left[\cos\frac{(1-\alpha_c)\pi}{2} \right] \right\} \tag{2.32}$$

where $\overline{\Delta w}$ has the same definition of $\bar{\delta}$ in Eq. 2.27 for the consistency of the units.

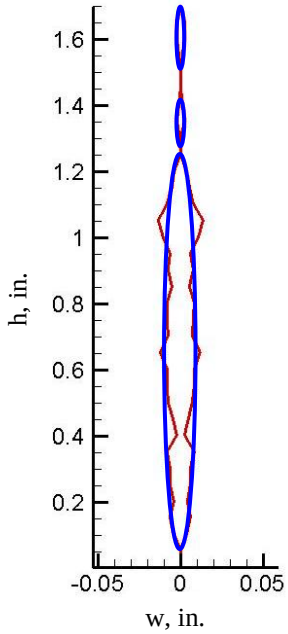

Fig. 2.6—Fracture's cross-section approximated by multiple ellipses.

A comparison of the deformation calculated by Eq. 2.32 and the average fracture width determines if these ellipses can keep open. If the deformation is larger than the narrowest width, ($\overline{\Delta w} > w_{\min}$), more asperities come into contact. I conduct the subtraction for each point, ($w_i - w_{\min}$), to get the new width profile for the next calculation step. As more and more asperities touch, ellipses become smaller and smaller. Meanwhile, the displacement decreases dramatically as the contact ratio is higher. Some of ellipses are totally closed because the deformations exceed the ellipse widths. I repeat this procedure as long as the contact happens. The transitional process of the closure is shown in **Fig. 2.7**.

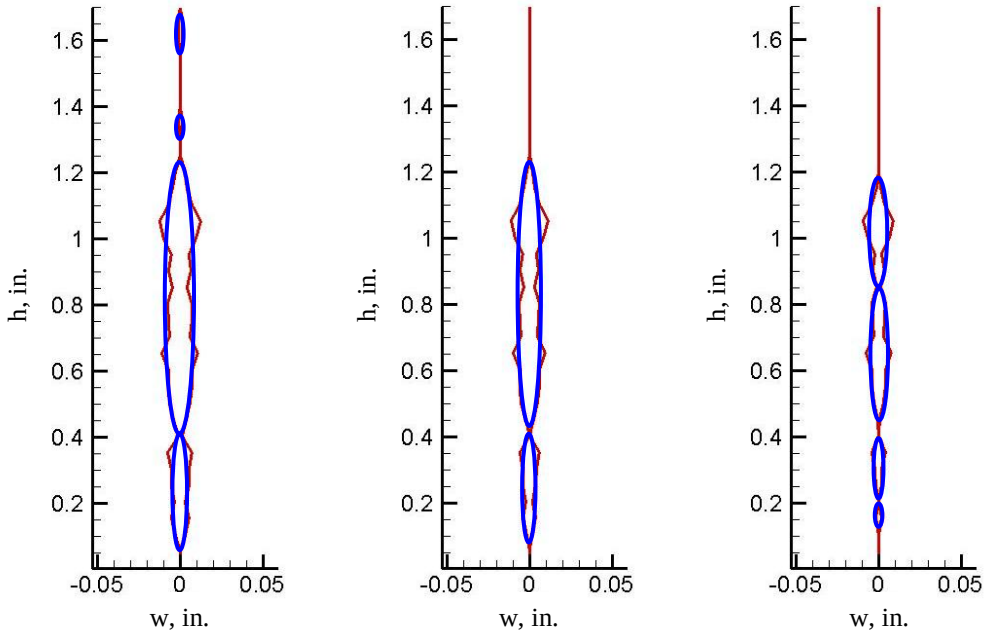

Fig. 2.7—Transitional process of closure simulated by analytical theory.

Finally, some large ellipses remain open even when a high closure stress is applied. At this stage, the average closure calculated by Eq. 2.32 is smaller than the narrowest width, ($\overline{\Delta w} < w_{\min}$). Then, the width for each point minus the average deformation, ($w_i - \overline{\Delta w}$), comes up with the width profile after the fracture closure shown in **Fig. 2.8**.

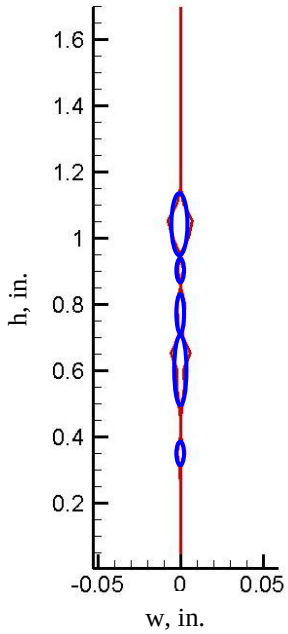

Fig. 2.8—Width profile for a fracture cross-section after closure.

To clarify the procedure, I plot the flow chart shown in **Fig. 2.9**. This approach gives a criterion to find openings for each cross-section of an acid fracture. If every cross-section has some openings after closure, channels exist through the fracture surfaces because I assume that the geometries of the adjacent cross-section are similar and ignore the mechanical effects between them. Therefore, the deformation for the entire fracture is attainable. I will use the method introduced above to obtain width distributions for different acid fractures under closure stress.

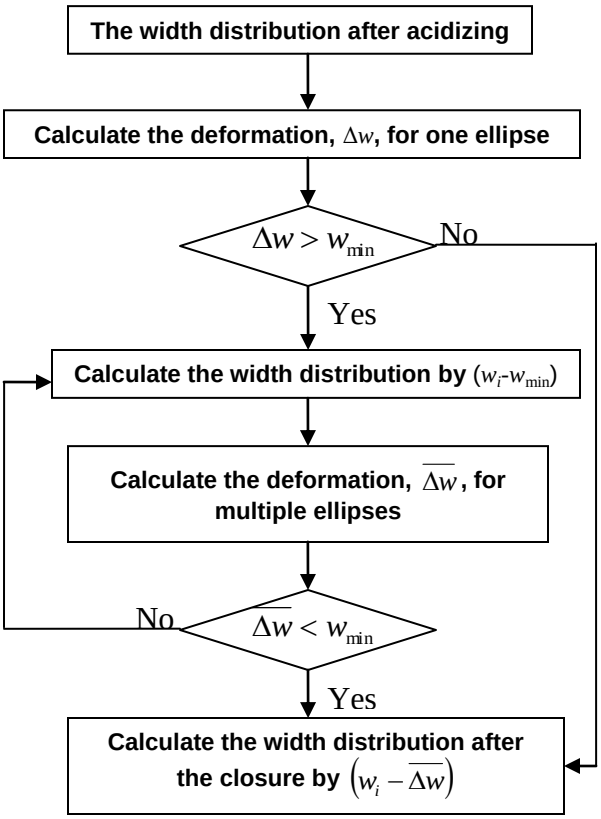

Fig. 2.9—Flow chart of fracture closure calculation.

The application of the procedure on every cross-section along the fracture leads to the width distribution after closure. **Fig. 2.10** shows the width distribution of one fracture wall at the experimental scale after acidizing but before closure. The previous example is one cross-section picked from this profile. Because the experimental design neglects the effect of gravity, the fracture is shown laterally instead of vertically. The fracture length is approximately 6 in., while the fracture height, which is the width in the figure, is about 1.7 in.

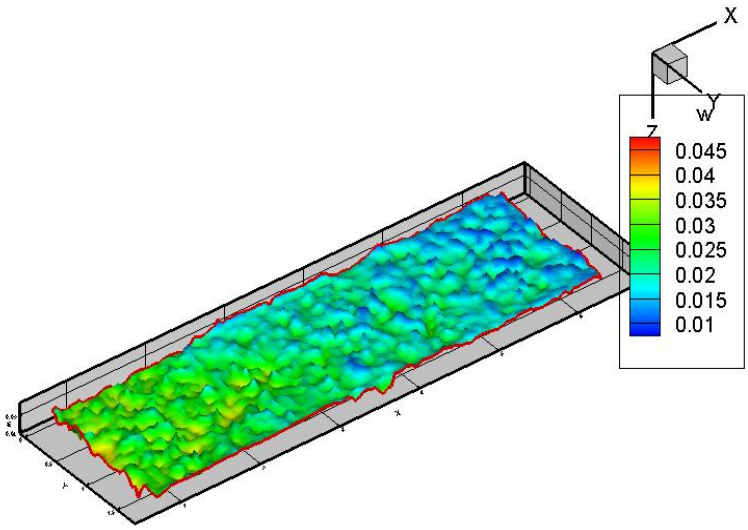

Fig. 2.10—Width distribution before closure.

After the application of the procedure, the width distribution of the fracture under 3000 psi closure stress is obtained as shown in **Fig. 2.11**. The dark blue area indicates that the rock at this point comes into contact and no space is left open. By the comparison with the distribution before closure, the rougher area around the inlet has more open space left, while the outlet area with less acid contact has more rock contacting. The channels do not form in this case because the roughness is the main feature resulting from the acid treatment at this experimental scale. But some conductivity from the openings is still possible. In the next section, I will introduce the methodology to calculate the conductivity for an acid fracture.

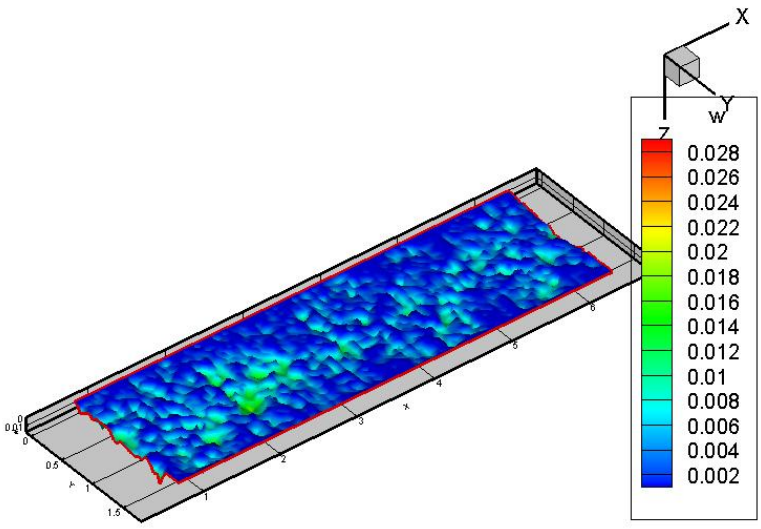

Fig. 2.11—Width distribution after closure.

2.4 Conductivity of Acid Fracture

For steady state flow, Zimmerman and Bodvarsson (1996) introduced exact solutions to the simplified Navier-Stokes equations for a simple case, in which the fracture consisted of two smooth, parallel walls separated by a uniform aperture. They showed that the permeability of the fracture can be identified as

$$k_f = \frac{w^2}{12}, \qquad (2.33)$$

where w is the fracture width, k_f is the permeability of the fracture. By definition, conductivity is the product of fracture permeability and fracture width. Thus, the cubic law is often written in the form of

$$C_f = k_f w = \frac{w^3}{12}. \qquad (2.34)$$

The cubic law can exactly give the conductivity of a fracture with two smooth, parallel walls separated by a uniform aperture. But it is not a good solution for a real fracture etched by acid. **Fig. 2.12** shows an example to compare the results from measurements and calculations by the cubic law. The laboratory provides the conductivity under different closure stresses for a fracture. I use the closure model to compute the width distribution after the fracture is closed numerically, and then substitute the average width of the fracture into the cubic law (Eq. 2.34) to calculate the conductivity. According to Fig. 2.12, the conductivity under high closure stress has the close estimate by both methods. However, the laboratory obtains high conductivity for low closure stress cases while the cubic law underestimates the values significantly. The conductivity by the cubic law looks linear to the increment of closure stress. It is not true because the rock will fail at certain high confining pressure. The experimental curve shows this failure between 2,000 psi and 3,000 psi. Therefore, the cubic law in terms of the average width after closure is not able to perform the conductivity calculation precisely.

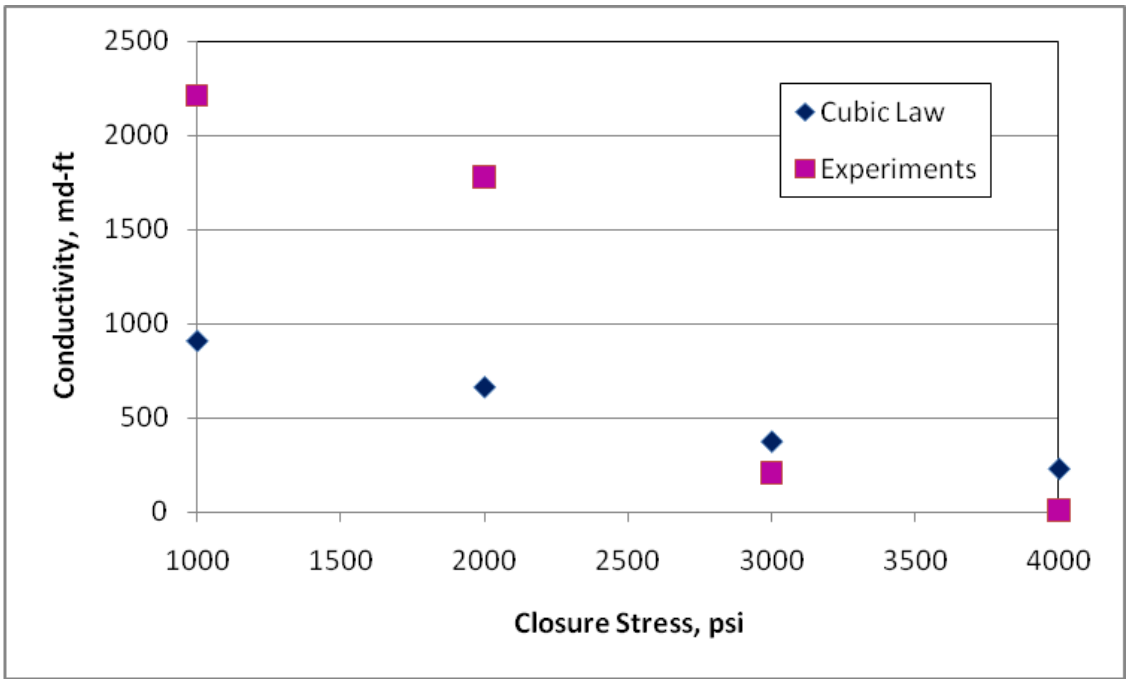

Fig. 2.12—Comparison between experimental results and calculations by the cubic law.

Apparently, the cubic law can't predict conductivity precisely for a fracture etched by acid unevenly. However, it holds locally when fluid flows through the subdivided or local fracture voids (Walsh, 1981), because a grid block is so small that two fracture surfaces in this grid block can be approximated as being be parallel to each other. This model is referred to as the local cubic-law that represents the state of the art for fluid flow simulation in a fracture. Brush and Thomson (2003) created synthetic rough walls to simulate fluid flow through them. By comparison with the Navier-Stokes equations, Stokes equations, and local cubic-law, they found that the local cubic-law was an acceptable approximation to the Navier-Stokes equations. Therefore, I use this algorithm to calculate conductivity for acid fractures with rough surfaces.

For each grid block, I can calculate flow rates in two directions along the fracture height and length according to the local cubic-law as:

$$q_x = \frac{k_f w h_x}{\mu}\frac{dp}{dx} = \frac{w^3 h_x}{12\mu}\frac{\partial p}{\partial x}, \tag{2.35}$$

$$q_y = \frac{k_f w h_y}{\mu}\frac{dp}{dy} = \frac{w^3 h_y}{12\mu}\frac{\partial p}{\partial y}, \tag{2.36}$$

where q is the flow rate, h is the grid length, μ is the fluid viscosity, and p is the pressure. The fracture closure models provide a width, w, under closure stress for each grid block. It is much smaller than the fracture length and height, so the flow perpendicular to the fracture surface is negligible. The 2D mass balance equation is expressed as

$$\frac{\partial q_x}{\partial x} + \frac{\partial q_y}{\partial y} = 0. \tag{2.37}$$

Substitution of Eqs. 2.35 and 2.36 into Eq. 2.37 yields the partial differential equation

$$\frac{\partial}{\partial x}\left(w^3 \frac{\partial p}{\partial x}\right) + \frac{\partial}{\partial y}\left(w^3 \frac{\partial p}{\partial y}\right) = 0. \tag{2.38}$$

I discretize the equation and solve it numerically. The flow chart for the conductivity calculation is shown in **Fig. 2.13**. With the width profile after fracture closure, I can calculate the pressure drop all along the flow path. The flow rate is then achievable by the local cubic-law (Eqs. 2.35 and 2.36). Finally, Eq. 2.39 gives the overall conductivity for the acid etched fracture.

$$C_f = \frac{q\mu x_f}{h_f \Delta p}, \tag{2.39}$$

where x_f is the fracture length and h_f is the fracture height.

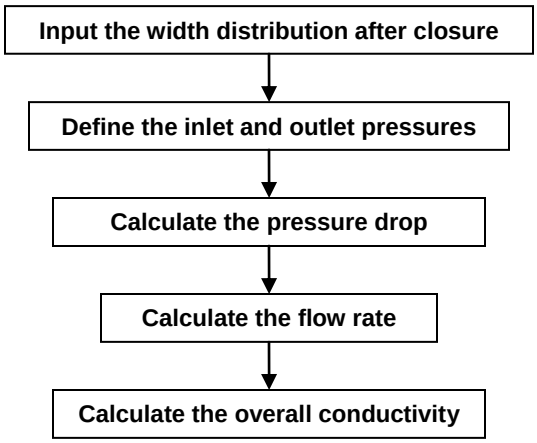

Fig. 2.13—Flow chart of conductivity calculation.

The application of the numerical conductivity calculation on the laboratory core samples makes it possible to compare with the measured results. I still select the same example as in section 2.3 to demonstrate the comparison. As shown in **Fig. 14a**, the width profile calculated by the analytical solution is a 2D illustration, which is the same width profile as in Fig. 2.11. After the fluid injection is modeled numerically, the 2D flow velocity profile, which is **Fig. 14b**, is also attainable. The red regions represent the high velocity while the blue regions represent the low velocity or even no flow. From these two profiles, the velocity is generally large in the area where the fracture width is small, because the mass balance requires the flow rate that is the product of the flow velocity and the area of cross-section to be the same all through the fracture. A large width leads to a large cross-section area that reduces velocity. In this case, the largest width occurs in the area between 2 and 3 in. Clearly, the velocity is lower than other areas. Also, the etching near the inlet is more intensive than near the outlet, so the velocity becomes larger along the fracture. However, fluid flows towards the direction

with the smallest resistance. Thus, when we look into one single cross-section, the velocity at wider spot is still relatively larger than other narrower spots. Therefore, the flow velocity profile is reasonable based on the explanations. It also validates the conductivity calculation method introduced previously.

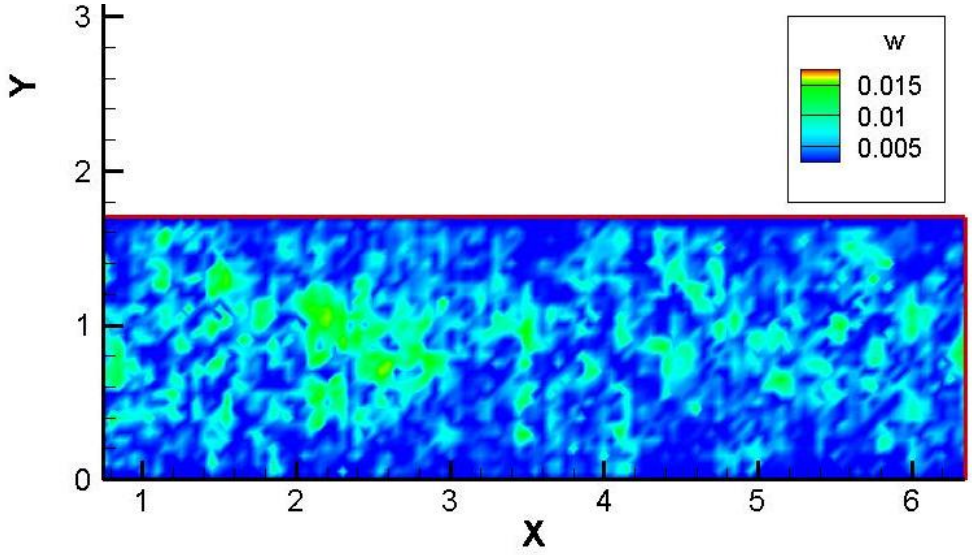

(a) Width Profile after Closure

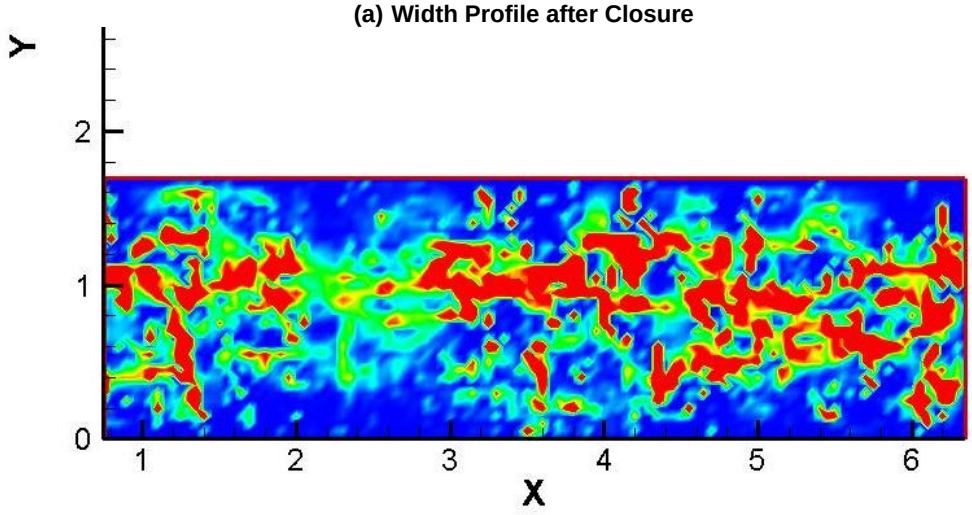

(b) Flow Velocity Profile

Fig. 2.14—Comparison between width profile and flow velocity after closure.

I generate the pressure drop curve by the program I developed for conductivity calculation (**Fig. 2.15**). The *x*-axis is the distance from the inlet of the fracture. It starts from 0.75 to 6.35, because the beginning and the end of the core sample does not have the same boundary as the rest. The inlet pressure is 10,000 Pa while the outlet pressure is set to zero. According to this curve, the slope in the first half is plain in general, especially during the section between 2 and 3 in. It is corresponding to the analysis above. The bigger width creates a high conductive flow path for fluid. Low resistance leads to low pressure drops. In contrast, the pressure drop for the second half of fracture declines much faster. Thus, small aperture results in high resistance for fluid flow. But high flow rate caused by high resistance yields a sharp pressure drop.

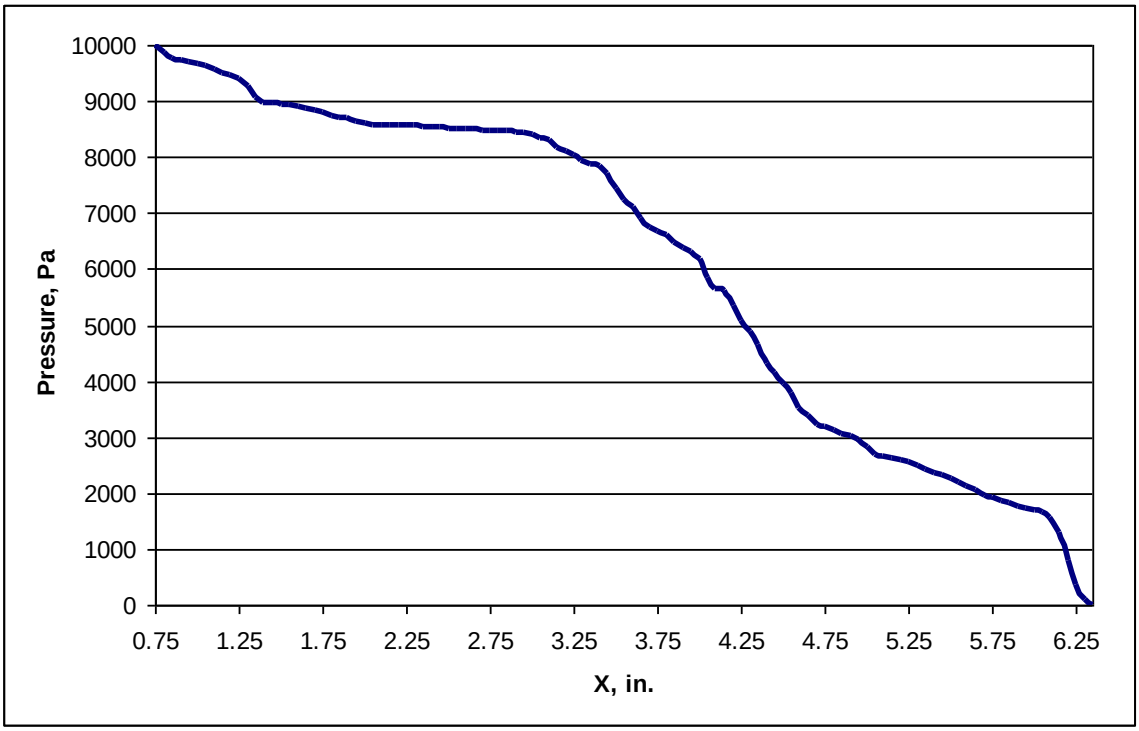

Fig. 2.15—Pressure drop curve used in conductivity calculation.

In the next chapter, I will use the methods introduced above on different scales of acid fractures: the experimental scale and the intermediate scale. The width profiles after closure and the conductivity of acid fractures will be presented and compared.

CHAPTER III

APPLICATIONS OF MODELS ON DIFFERENT SCALES

Nierode and Kruk (1973) developed the most widely used correlation of acid fracture conductivity based on the experimental data from laboratory tests. Many researchers (Williams, et al. 1979, Anderson and Fredrickson, 1989, Van Domelen, 1992) also conducted numerous experiments to investigate the acid fracture conductivity under different conditions. In the first section of this chapter, I will apply the analytical solutions introduced in Chapter II on some width profiles from the lab (Pournik, 2008) and compare with the experimental results. The second section of this chapter will continue to study the acid fracture conductivity after closure at the intermediate scale based on the work accomplished by Mou et al. (2009, 2010a, 2010b). The intermediate scale simulation on rock deformation and conductivity calculation will close the gap between laboratory scale measurements and macro scale acid fracture models.

3.1 Acid Fracture Closure on Experimental Scale

After obtaining the analytical solutions for a single ellipse and a collection of cracks, I apply them to approach the deformation of acid-etched fracture created in our laboratory. The plots of width distribution after deformation show the effect of closure stress. Comparison of numerical and experimental results present the accuracy of this method.

3.1.1 Experimental Conditions

The laboratory apparatus built by Zou (2005) has been used to conduct a variety of experiments on different kinds of rock. At small scale, they acidized core samples and measured the conductivity under different closure stresses. The publications (Melendez et al. 2007; Pournik et al. 2007; Malagon et al. 2008; Antelo et al. 2009) present the experimental results. I will apply the analytical solutions derived above to the lab cases. The comparison between the numerical model and experiment is used to validate the simulation.

An introduction of the experimental procedure is necessary. The core sample prepared in the lab has a surface approximately 7 in. long by 1.7 in. wide, with a thickness around 3 in. shown in **Fig. 3.1**. Pournik (2008) placed the rock samples inside a modified API conductivity cell and used a pump to allow injection at different rates. Cylindrical ceramic radiant heaters and a back pressure regulator were also installed to control the temperature and leakoff to represent field conditions appropriately. Acid injection and rock surface etching started after the desired cell pressure, leakoff rate, and temperature were achieved. After the acid treatment, a profilometer scans the rough surfaces created by the acid and outputs the width profiles (Antelo et al., 2009). In order to measure the fracture conductivity, they apply closure stress and flow nitrogen between two acid etched core samples and record the pressure drop across the fracture. The closure stress is in increments of 1,000 psi, starting from 1,000 to 6,000 psi. Based on the measurements, the Forchheimer's equation for flow through a porous medium yielded the conductivity values of the closed fractures.

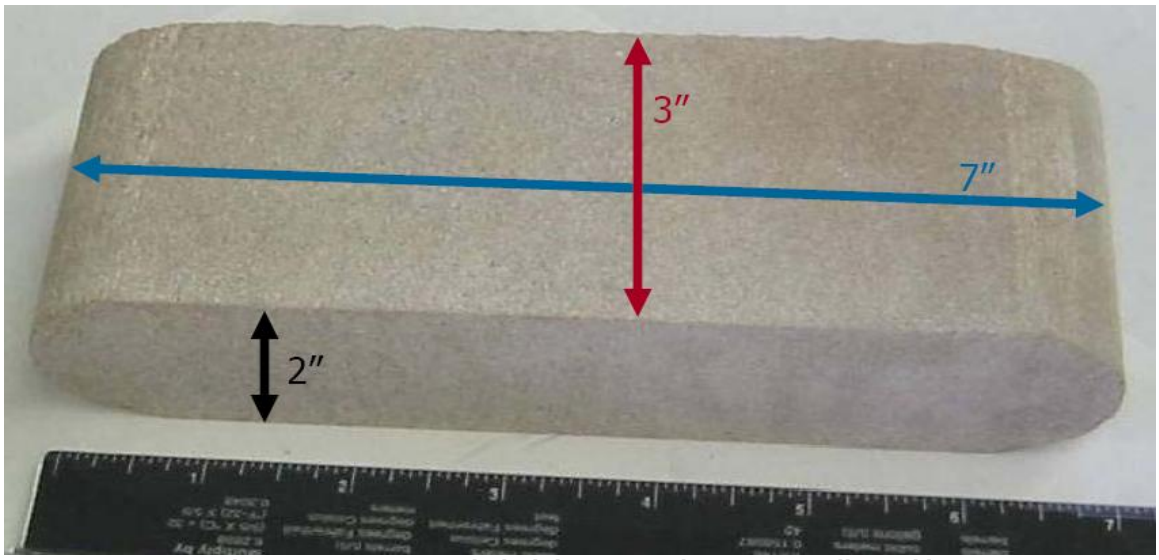

Fig. 3.1—Core sample in laboratory. (From Pournik et al.)

By using the profilometer (Antelo et al. 2009), the laboratory provides the width profiles after acid treatment but before fracture closure, so I can use cracks to approximately describe the geometry of fracture cross-sections. The fracture height is about 1.7 in. while the fracture width is on the order of 10^{-2} in., which is similar to the shape of a crack defined previously. **Fig. 3.2** is one of the outputs from the profilometer. From the previous description, the analytical solutions are able to give the width profile after closure and calculate the conductivity for the acid fracture. Therefore, I will continue to model the deformation of other experimental cases and present the results.

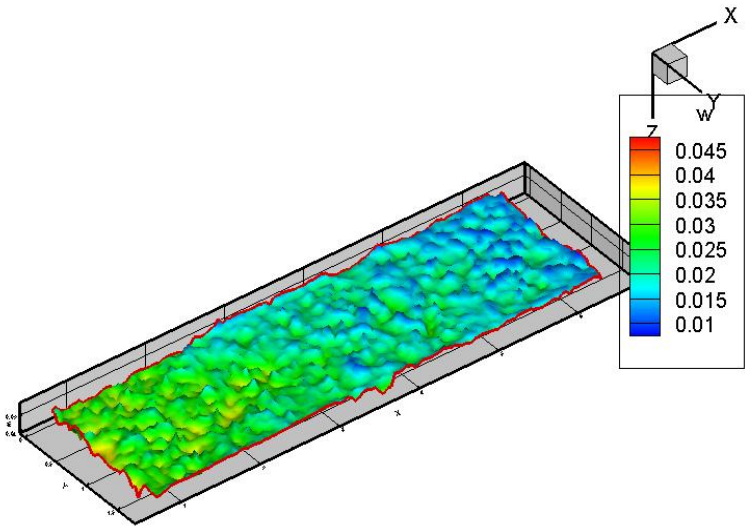

Fig. 3.2—Width distribution before closure.

3.1.2 Modeling Closure Behavior

The laboratory gives the basic width information for five core samples listed in **Table 3.1**. 3,000 psi is the closure stress applied on every fracture. After the fractures are closed, I plot the width distribution at the same scale as in the experiments. **Fig. 3.3** demonstrates one of two fracture surfaces for these five samples before and after closure respectively. The laboratory scans the profile before closure while I plot the profile after closure based on the calculations.

TABLE 3.1—WIDTH INFORMATION FOR FIVE DOLOMITE CORE SAMPLES

Core samples	Acid contact time, min	Width before closure, in.				Width after closure, in.	
		Maximum	Minimum	Average	SD, σ	Maximum	Average
CD1	20	0.170	0.012	0.038	0.011	0.035	0.0030
CD2	20	0.163	0.007	0.023	0.008	0.029	0.0030
CD3	30	0.289	0.010	0.037	0.013	0.107	0.0056
CD4	10	0.283	0.015	0.027	0.006	0.045	0.0018
CD5	30	0.142	0.013	0.032	0.007	0.025	0.0036

The acid contact time in Table 3.1 shows the different acid injection conditions. The longer the acid contact time is, the rougher the fracture surfaces are. σ is the standard deviation of asperities before closure, which describes the dispersion of the widths on either side of the average values. The minimum width after closure is apparently zero, so I did not list it in the table.

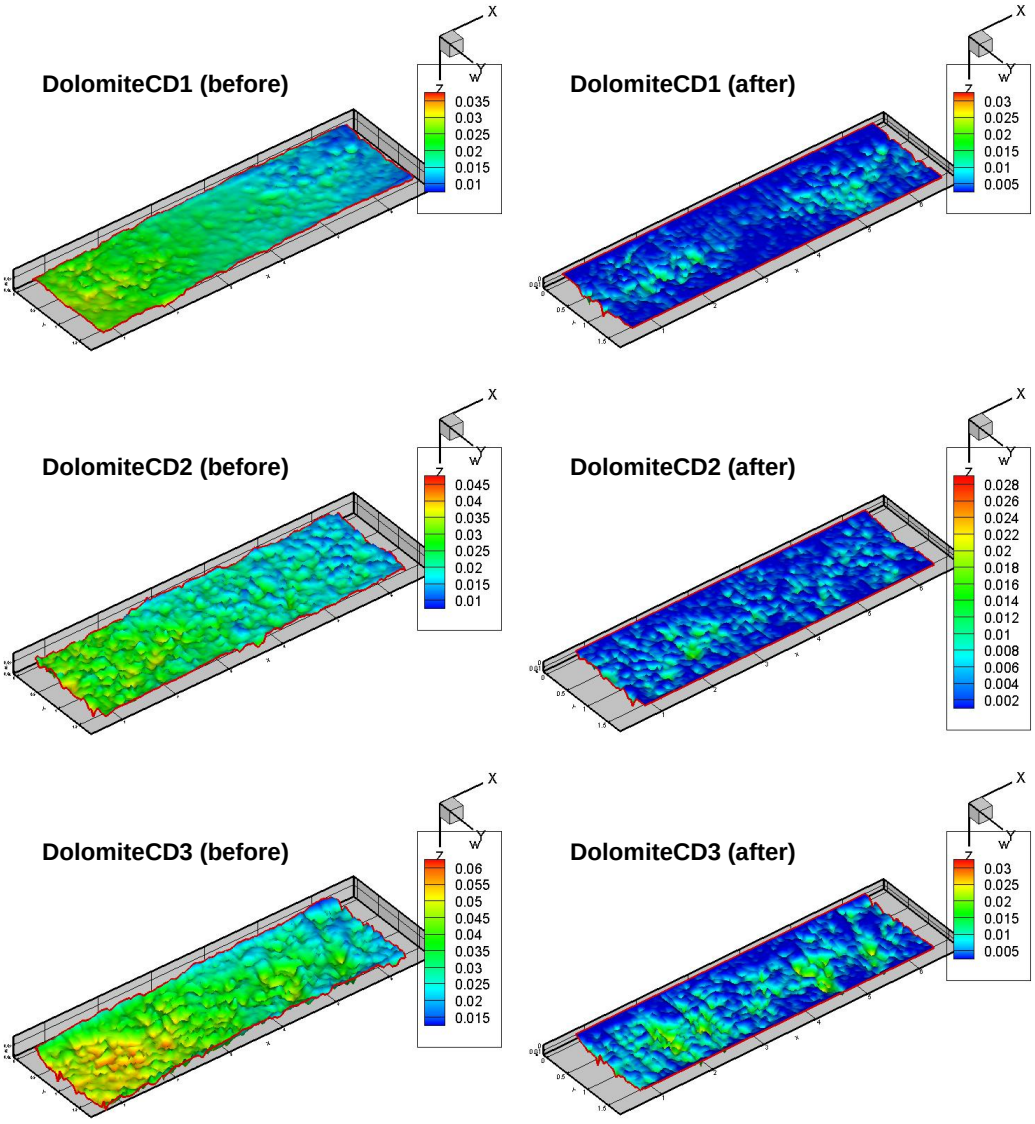

Fig. 3.3—Width profiles of fracture surfaces before and after closure.

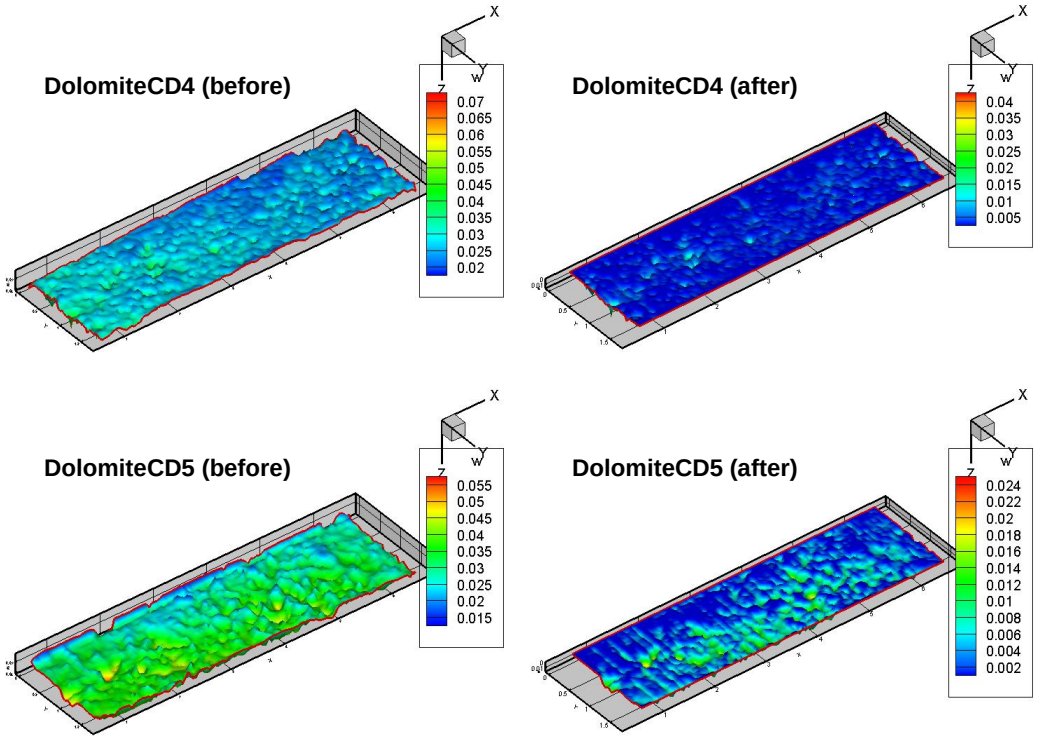

Fig. 3.3 Continued

CD1 and CD2 are comparable because they have the same acid contact time, 20 minutes. However, their etching patterns are different from each other. The standard deviation of CD1, 0.011, is higher than the one of CD2, 0.008. But CD1 has rough regions near inlet and outlet while the middle region is much flatter (Fig. 3.3). It leads to more closure and fewer openings left in the middle of fracture. Relatively, the etching pattern of CD2 is more continuous all through the fracture. The average width after closure is the same as the one of CD1 despite the lower standard deviation and average width before closure. More importantly, the channels formed in CD2 were more continuous than in CD1. I can imagine that the conductivity of CD2 will be higher.

CD3 and CD5 have longer injection history than CD1 and CD2. Their etching patterns are also similar to each other from the plots. But according to Table 3.1, the standard deviation of CD5, 0.007, is much smaller than the one of CD3, 0.013. It means that the surfaces of CD3 are rougher than CD5. Under closure stress, more asperities in CD3 will prevent the fracture from closing. Therefore, the average and maximum widths after closure of CD3 are much higher than CD5. If channels connect the openings through the fracture, I expect that the conductivity of CD3 will be higher as well.

The acid injection into CD4 is short, so the fracture surfaces are much evener than other core samples. After the deformation under closure stress, 3,000 psi, CD4 is almost closed everywhere except at some disconnected apertures. Thus, it is not a good acid fracturing treatment.

From the discussion above, the analytical calculation for a series of 2D cracks performs well on the whole fracture, though I ignore the effects between cross-sections. Actually, some closed strips caused by neglecting do not look reasonable in a fracture. But the big apertures and high asperities still create the openings after closure, while the small and thin cracks are totally closed under high stress. The connected openings generate the channels that will contribute a lot on conductivity of a fracture. Therefore, I will calculate the conductivity for these core samples and compare with the experimental results.

3.1.3 Comparison with Experimental Results

To test the validity of the model of fracture closure and resulting conductivity developed, I modeled some of the experiments reported by Pournik (2008). Among all the experiments, I use one dolomite sample, CD2, to illustrate our simulation first. The width profile scanned by the profilometer after the acid etching in the lab is shown in **Fig. 3.4**. The *x* axis represents the fracture length direction while the *y* axis represents the height direction. As the acid dissolves the rock along the fracture length direction, the etching occurring near the acid inlet is obviously much larger than at the fracture outlet area. From the measured surface profiles, when the two core surface are just contacting each other, the average width of the fracture is 0.023 inch, the maximum width is 0.163 inch, and the standard deviation of the width distribution is 0.008.

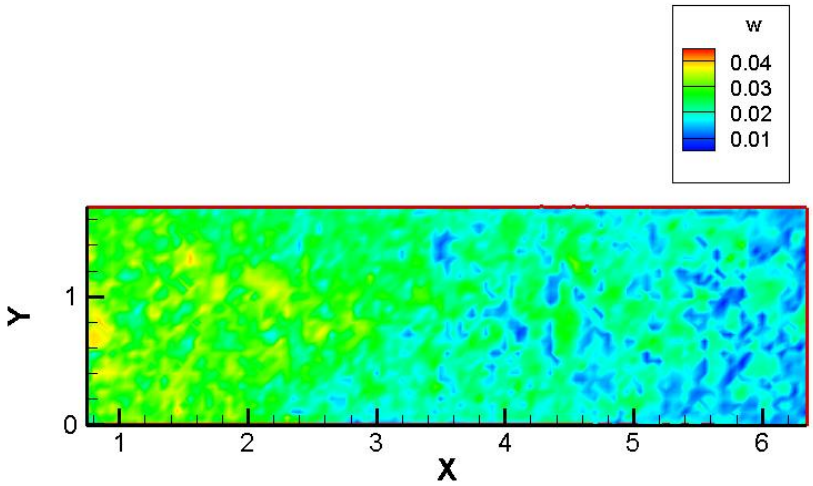

Fig. 3.4—Width profile scanned in the lab.

Applying the closure models, I calculated the deformations of the fracture under different closure stresses ranging from 1,000 to 4,000 psi. **Figs. 3.5 through 3.8** show

the width profiles accordingly after the fracture closure. The average widths and maximum widths for the width profiles are shown in **Table 3.2**. At low closure stress (Figs. 3.5 and 3.6), the numerical model overestimates the conductivity, while it yields a slightly lower conductivity at the high closure stress (Fig. 3.7 and 3.8) compared with the experimental measurements. But generally, this good agreement in conductivity between experiments and simulations suggests that our approximation of cross-section along the fracture being a series of elliptical openings in mechanical equilibrium with the closure stress is a reasonable model of acid-etched fractures. After obtaining the width profiles after fracture closure, I applied the numerical conductivity calculation introduced previously to compare with the measured results.

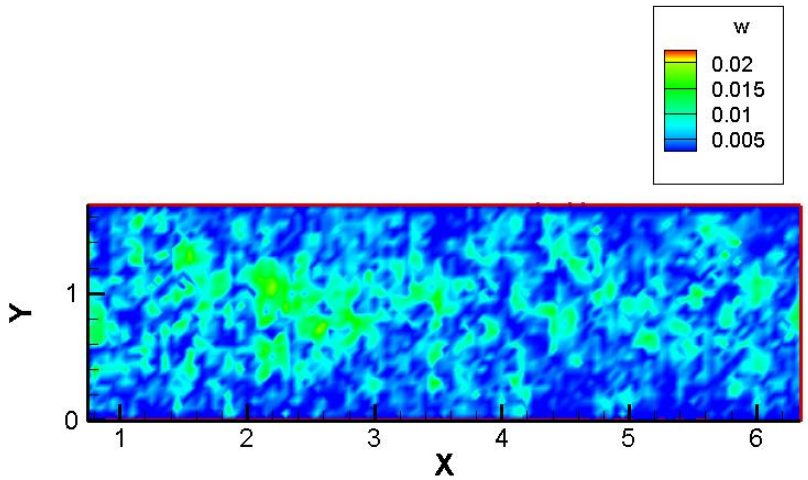

Fig. 3.5—Width profiles of fracture surfaces under closure stress 1,000 psi.

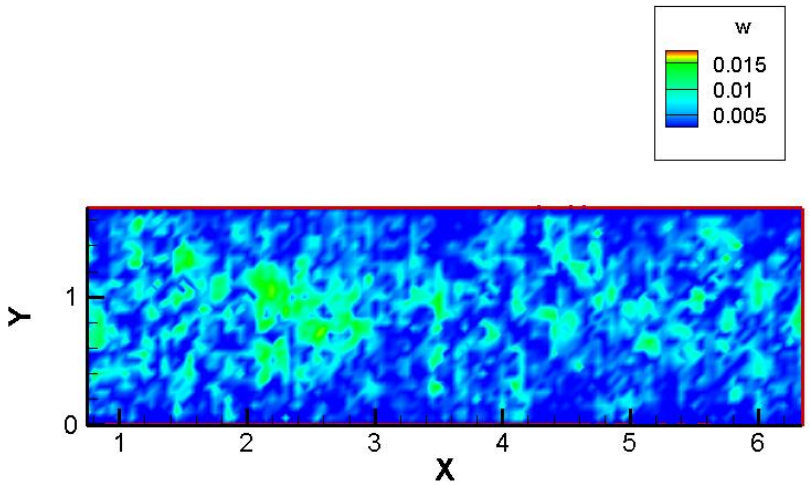

Fig. 3.6—Width profiles of fracture surfaces under closure stress 2,000 psi.

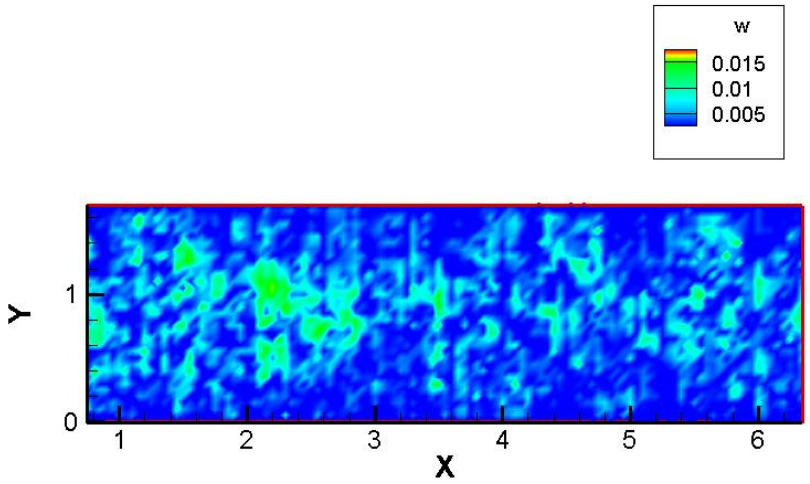

Fig. 3.7—Width profiles of fracture surfaces under closure stress 3,000 psi.

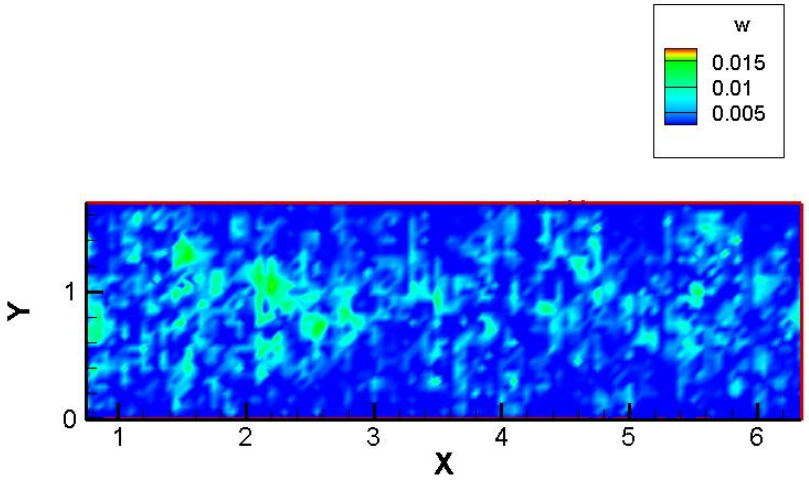

Fig. 3.8—Width profiles of fracture surfaces under closure stress 4,000 psi.

TABLE 3.2—WIDTH AND CONDUCTIVITY WITH RESPECT TO CLOSURE STRESSES FOR DOLOMITE CORE SAMPLE				
Closure stress, psi	Width after closure, in.		Conductivity, md-ft.	
	Maximum	Average	Experiment	Simulation
1,000	0.0432	0.0090	2,210	2,614
2,000	0.0408	0.0075	1,779	1,698
3,000	0.0402	0.0060	206	189
4,000	0.0397	0.0049	206	10

Table 3.2 gives the average and maximum fracture widths from the model and the experiments, and predicted fracture conductivities for each closure stress. The conductivities from the model and from the experiment are also plotted in **Fig. 3.9**. The conductivities predicted by the model compare well with the conductivity measured in the experiments.

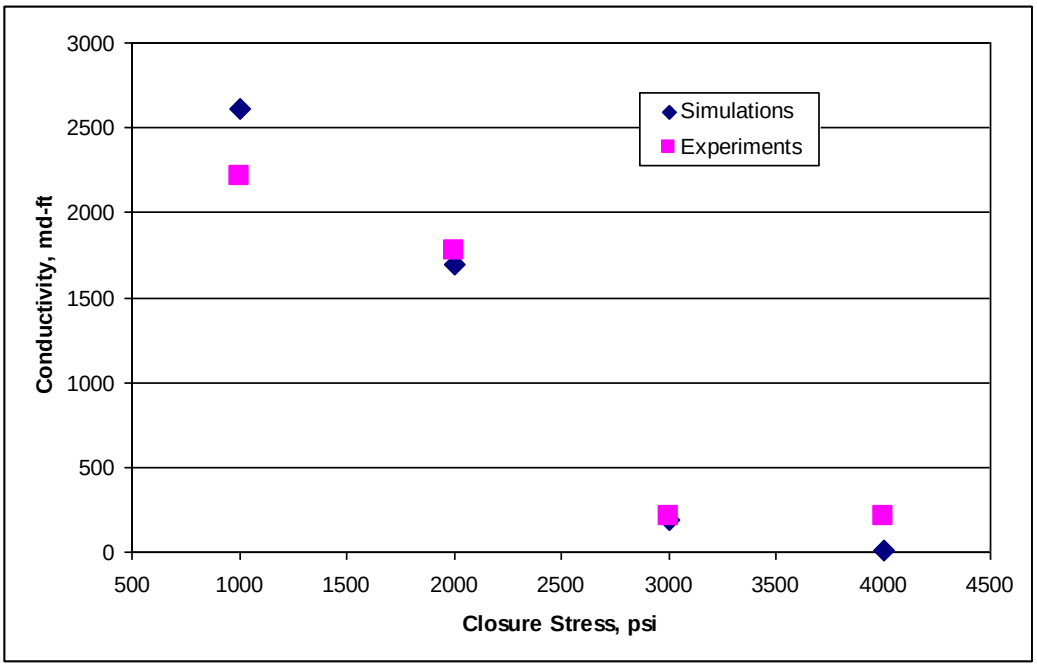

Fig. 3.9—Fracture conductivity changes with respect to various closure stresses.

An obvious conductivity drop happens between 2,000 psi and 3,000 psi. Because contacting asperities reach the yield strength, a small compression can result in a large closure at this time. The more closure happens, the lower the conductivity is. Thus, the conductivity drops quickly in this period. I also observe this feature for many other core samples in the laboratory, though it is not always occurring.

Furthermore, the beginnings of two curves do not match well either. The simulated conductivity is higher and the slope is bigger. I can simply use the cubic law to estimate the initial conductivity, which is the conductivity under zero closure stress before closure. The initial width of CD2 after acid treatment is 0.023 in. according to Table 3.1. By the cubic law, the cube of average width divided by 12 yields 36,318 md-ft. This number may be too high for two rough surfaces, because the cubic law is only valid for two parallel, smooth surfaces. But it gives the basic concept of initial

conductivity. If the curve follows the experimental trend, it will definitely overestimate the initial conductivity. In contrary, the trend of the simulation curve approaches better.

CD2 is a good example to illustrate that the closure model and the conductivity calculation perform well at the experimental scale. I also conduct the same procedure on other core samples from the laboratory. **Table 3.3** summarizes the results I have obtained. As mentioned previously, CD4 has a short acid treatment before closure. It is not comparable with other core samples because of the evener surfaces. Thus, I do not list it in the table.

TABLE 3.3—CONDUCTIVITY COMPARISON BETWEEN EXPERIMENTS AND SIMULATIONS

Core samples	Acid contact time, min	Method	Closure stress, psi			
			1,000	2,000	3,000	4,000
CD1	20	Experiment	4,230	3,959	3,193	4,468
		Simulation	5,319	1,422	166	13
CD2	20	Experiment	2,210	1,779	206	206
		Simulation	2,614	1,698	189	10
CD3	30	Experiment	2,745	2,447	2,341	2,097
		Simulation	16,382	7,507	3,520	1,457
CD5	30	Experiment	943	1,019	808	122
		Simulation	2,768	450	319	-

In order to present the comparison clearly, I also plotted the conductivity with respect to the closure stress (**Figs. 3.10 through 3.13**) for each case in the table above. When the closure stress is low, the simulation estimates the higher conductivity than the experiment does. The reason is similar as the previous explanation for CD2 (Fig. 3.11). Under high closure stress, the conductivities calculated are lower than the ones measured. The reason is some small openings are fully closed in the simulation, while they can be captured in the experiments. CD3 (Fig. 3.12) has higher conductivity than

CD5 (Fig. 3.13) no matter whether the results are from experiments or simulations. It meets the expectation when I analyzed their deformations in previous section. The standard deviation and the width after closure for CD3 are both larger than CD5 according to Table 3.1. Although the rock type and acid contact time are the same in this case, the different etching patterns results in different closure behaviors, which yield different conductivities.

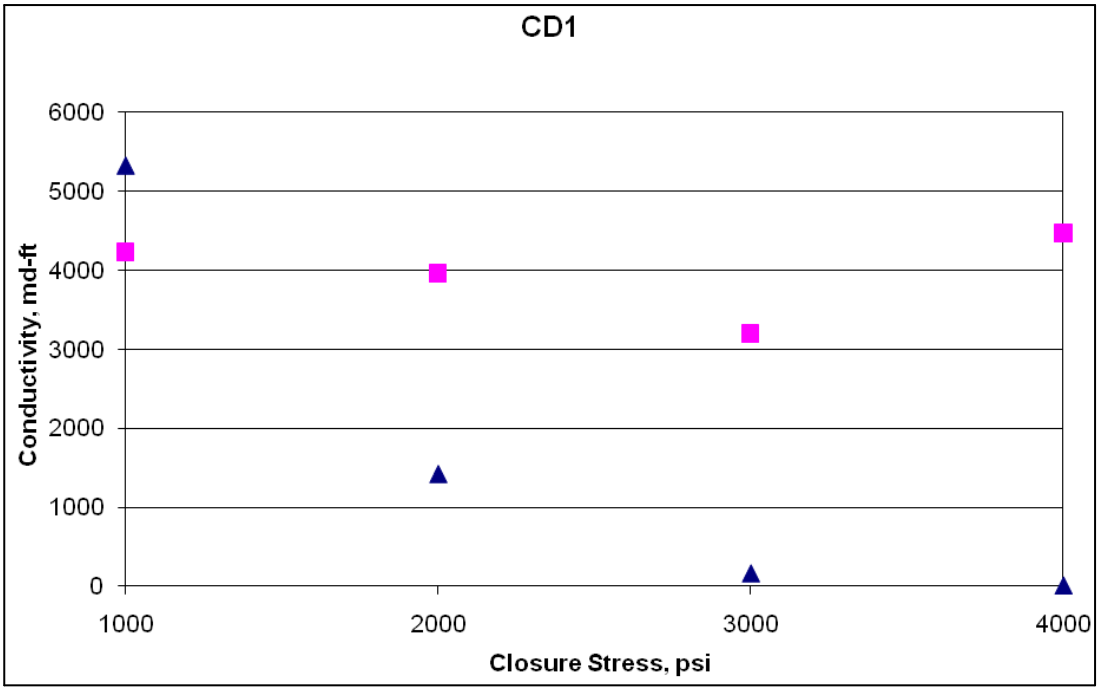

Fig. 3.10—Fracture conductivity comparison for CD1.

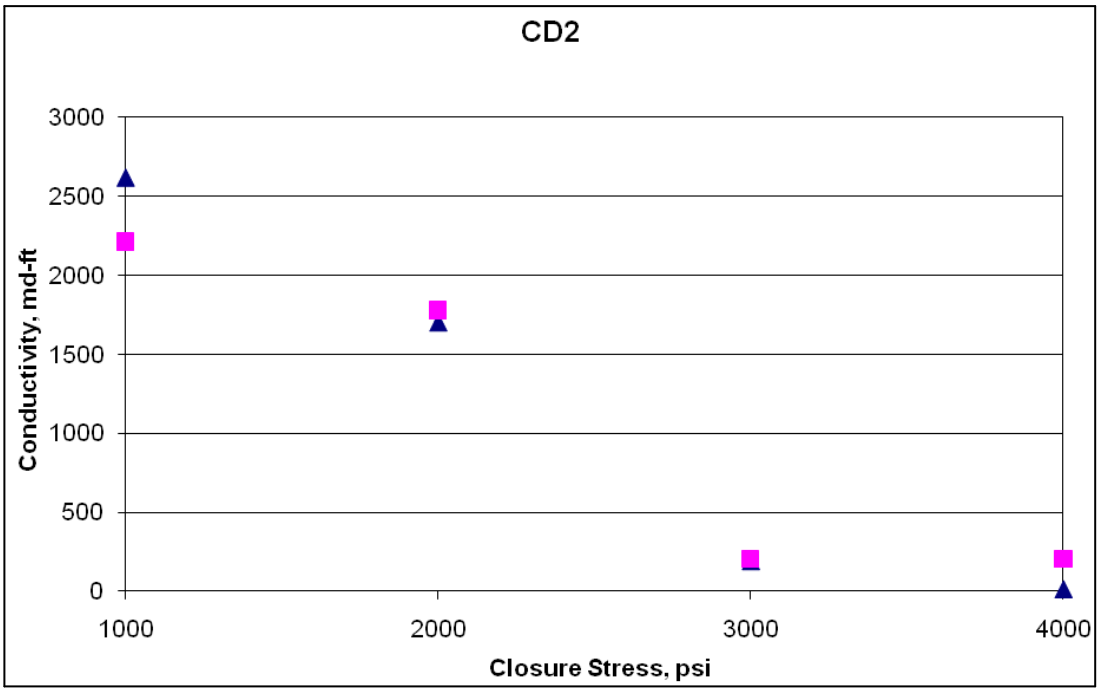

Fig. 3.11—Fracture conductivity comparison for CD2.

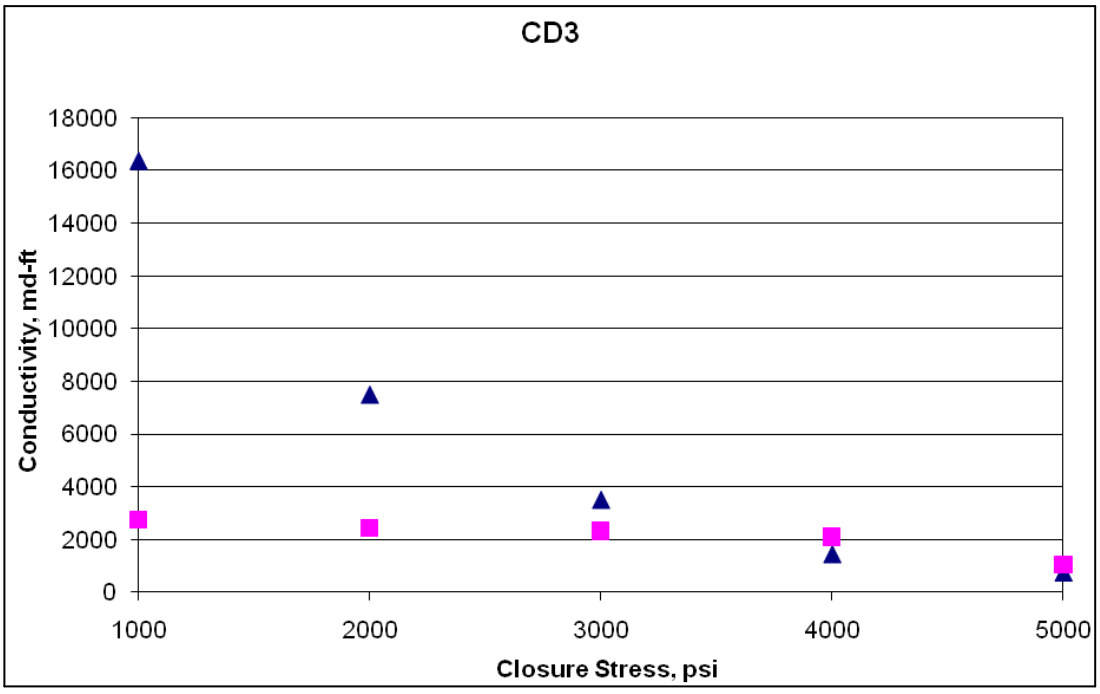

Fig. 3.12—Fracture conductivity comparison for CD3.

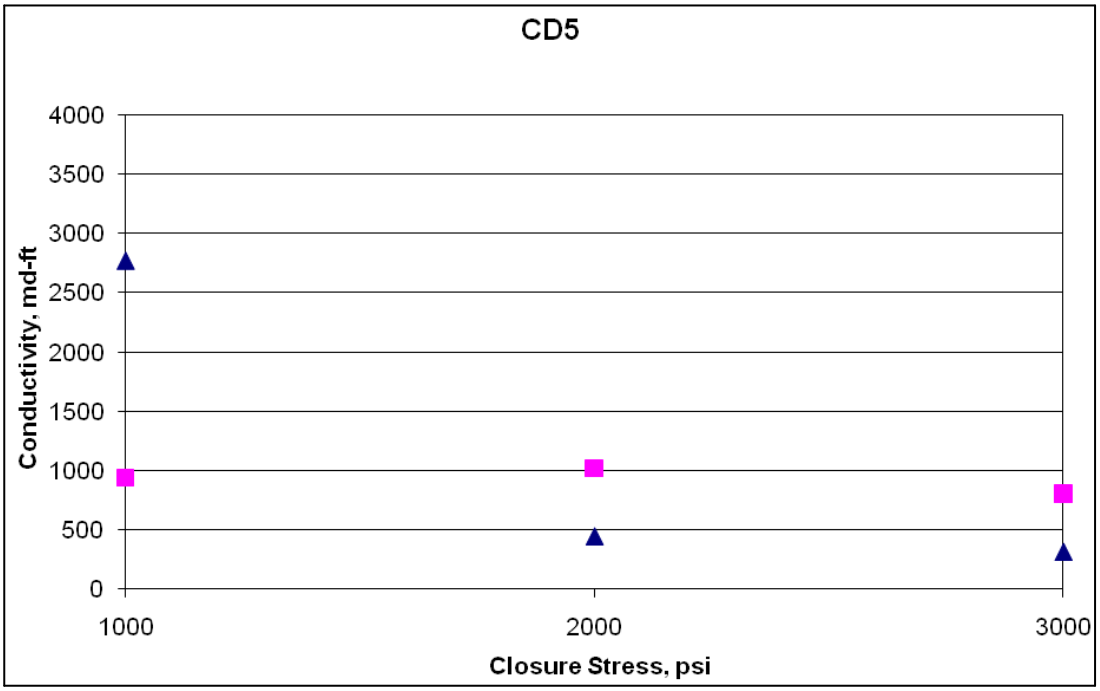

Fig. 3.13—Fracture conductivity comparison for CD5.

From the discussion above, the 2D analytical solution approaches the deformation of acid-etched fracture well, even though the effects between cross-sections are neglected. It captures most of the big openings, which will be connected to form a channel for petroleum fluid. But it does not take some permeable zones into account because of the smaller scale. That causes the underestimate of conductivity after closure. Also, the local cubic-law applies to the prediction of fracture conductivity. The flow rate change and the pressure drop trend are reasonable. And the conductivities calculated by the local cubic-law are in the proper range compared with the experimental results.

3.2 Acid Fracture Closure on Intermediate Scale

The success of the model at the experimental scale is convincing to scale up to a larger fracture domain, which is 10 by 10 feet. Mou (2009) has run many numerical experiments to simulate acid fractures and provide width distributions after acid injections for a fixed period of time. He also calculated fracture conductivities at zero closure stress by numerically bringing fracture surfaces into contact and modeling fluid flow at a fixed pressure drop along the fracture. I continue this work by investigating the mechanical behavior under closure stress and computing the conductivities for these acid fractures.

3.2.1 Fracture Surface Characterization

The introduction to the process of creating fractures is necessary because many parameters have effects on the mechanical behavior during closure. Mou et al. (2009) modeled the acid etched fractures based on the distributions of permeability and mineralogy across the fracture surface. The characterization of these fields includes average permeability, $\bar{k}$, normalized correlation lengths, $\lambda_{D,x}$, $\lambda_{D,z}$, and normalized standard deviation, σ_D. The horizontal correlation length, $\lambda_{D,x}$, is a ratio of permeability correlation length in the horizontal direction to the fracture domain size, which is 10 feet in the Mou (2009) model. So it is defined as,

$$\lambda_{D,x} = \frac{\lambda_x}{10}. \tag{3.1}$$

The vertical correlation length, $\lambda_{D,z}$, is also a ratio of permeability correlation length to the domain size, but it is specific to the vertical direction,

$$\lambda_{D,z} = \frac{\lambda_z}{10}. \tag{3.2}$$

These correlation lengths quantify how strongly the permeability trends in a horizontal and vertical direction. The normalized standard deviation, σ_D, is expressed mathematically as:

$$\sigma_D = \frac{\sigma(\ln(k))}{\ln(\bar{k})}, \tag{3.3}$$

where $\sigma(\ln(k))$ is the standard deviation of the natural logarithm of permeability. The normalized standard deviation, σ_D, measures the dispersion of the permeability distribution. In this study, the average permeability is possibly less, equal, or greater than 1 md. Eq. 3.3 stands for the cases with the average permeability greater than 1 md. When it is equal to 1 md,

$$\sigma_D = \frac{\sigma(\ln(k))}{\ln(10)}. \tag{3.4}$$

When it is less than 1 md,

$$\sigma_D = \frac{\sigma(|\ln(k)|)}{|\ln(\bar{k})|}. \tag{3.5}$$

The correlation length represents the correlation strength in a certain direction, which is defined as the distance from which no further correlation of a physical property exists associated with that point. It can be quantified by using the semivariogram model (Hardy and Beier, 1994). The theoretical semivariogram, γ, is defined as one half of the

variance of the differences in sample grades between points separated by a distance, *h* (Royle, et al. 1980). It can be mathematically expressed as,

$$\gamma(h) = \frac{1}{2}\frac{1}{(N-h)}\sum_{i=1}^{N-h}(z_i - z_{i+h})^2 , \qquad (3.6)$$

where $\gamma(h)$ is the variance, N is the number of data points, z_i are individual data points, z_{i+h} are individual data point located distance, h, away from z_i.

Beatty (2010) shows an example of a variogram that plots variability within a dataset with respect to location of the data (**Fig. 3.14**). Each point on the variogram represents the relationship between data pairs from the original dataset separated by distance, *h*. As the distance increases, the similarity of two separated permeability measurements decreases. Eventually, the curve reaches a plateau. The correlation length can be visually interpreted from the variogram by the lag where the sill is reached. This lag distance is the correlation length of the sampled data points. (Isaaks and Srivastava, 1989).

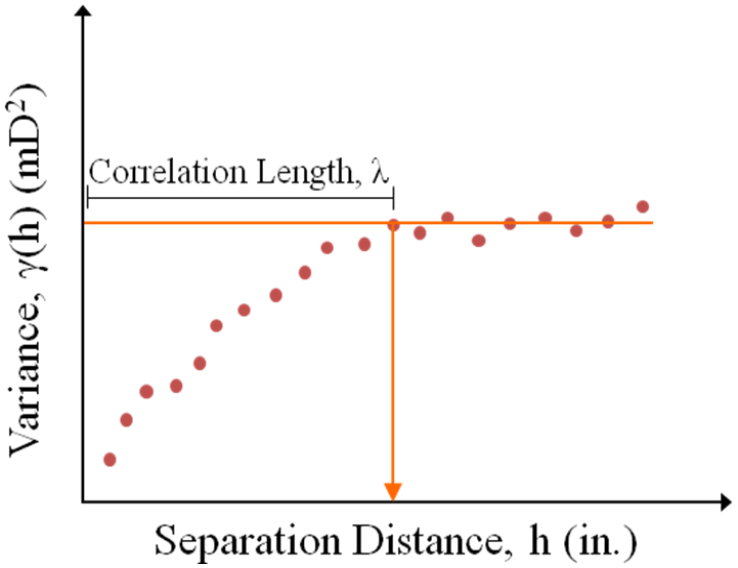

Fig. 3.14—Variogram example (From Beatty).

Based on these statistical parameters of the permeability and mineralogy fields, Mou et al. (2009) generated two fracture surfaces and developed a 3D intermediate-scale acid fracture model to numerically simulate the acid fracturing process, including acid transport inside the fracture, acid leakoff into the formation, and acid/rock reaction on the fracture surfaces. The higher average permeability leads to the higher leakoff that results in more dissolution of rock. The form of the channels in a fracture highly depends on the correlation lengths in both directions of the permeability distribution. High horizontal correlation length and low vertical correlation length yield long and narrow channels. The standard deviation of the permeability field determines the roughness of the etched rock surface. The fracture width profiles after acidizing obtained from the acidizing model serve as the inputs in our fracture closure model.

3.2.2 Base Conductivity

The intermediate scale of the simulation is an important factor during the closure of an acid fracture. **Table 3.4** shows the scale comparison between experiments and simulations. The fracture height in our lab is about 1.7 inches that is scanned 34 points by the profilometer. The simulation domain is 10 feet by 10 feet with 256 grid blocks along the fracture height direction. Thus, the grid height for the experimental samples is 0.05 inch, while the grid height for the simulations is 0.47 inch, which is almost ten times higher than the experimental height. But the average widths after acidizing for both cases are very close to each other.

TABLE 3.4—SCALE COMPARISON BETWEEN EXPERIMENTS AND SIMULATIONS

	Fracture Height, in.	Grid Blocks	Grid Height, in.	Average Width, in.
Experiments	1.7	34	0.05	0.05
Simulations	120	256	0.47	0.04

When considering 20 grid blocks from each scale, I can use one ellipse to approach the shape. The height of 20 grids at the experimental scale is 1 inch, while the height at the simulation scale is about 9.4 inches. The analytical solution (Eq. 2.31) in Chapter II gives the deformation under the closure stress. Assume that the Poisson's ratio, ν, is 0.3, the shear modulus of rock, G, is 4×10^5 psi, the closure stress is 3,000 psi, and let x equal to 0. For the experimental case,

$$\Delta w_1 = \frac{2(1-\nu)\sigma_c}{G}\left(a^2 - x^2\right)^{1/2} = \frac{(2)(1-0.3)(3000)(1)}{4\times10^5} = 0.01in. \qquad (3.7)$$

For the numerical simulation,

$$\Delta w_2 = \frac{2(1-\nu)\sigma_c}{G}\left(a^2 - x^2\right)^{1/2} = \frac{(2)(1-0.3)(3000)(9.4)}{4\times10^5} = 0.099in. \qquad (3.8)$$

Compare these two numbers with the average width in Table 3.4. Δw_1 is smaller than 0.05 inch, while Δw_2 is bigger than 0.04 inch. With the same amount of grid blocks, the fracture at the experimental scale is left open while the one at the simulation scale is closed under the same closure stress. This synthetic example indicates that the intermediate-scale simulation fails to capture some information at the small experimental scale, because with the same order of the average width, the size of the intermediate-scale grid is much larger than the one at small scale. Therefore, compensation at the small scale for the numerical simulation is necessary.

Observe that the size of a grid block in the numerical simulation is in inch as that is at the same order as the experimental one. Thus, I assign conductivity, which is named base conductivity, in the closed grid of simulation when calculating the conductivity for the intermediate-scale fracture. Next, I will introduce the method of obtaining the base conductivity.

In the literature review, I introduce some correlations based on experiments. One of the most widely used correlations (Eq. 1.6) was developed by Nierode and Kruk (1973). According to the data they published, the ideal fracture width is approximately 0.06 inch in average. In the intermediate-scale simulation by Mou (2009), the average fracture width after acidizing ranges from 0.02 to 0.08 inch.

The definitions for these two kinds of width are not the same. The ideal width, w_i, as known as the dissolved rock equivalent width, which is in the Nierode and Kruk's

correlation is defined as the ratio of dissolved rock volume to fracture surface area. In contract, the fracture width, $\overline{w}$, in Mou's work is the average width after two fracture surfaces come into contact at zero closure stress. **Fig. 3.15** is a 2D example showing the difference between these two definitions. The width in Fig. 3.15a is the ideal width after acidizing. Once the highest asperities at 0.05 inch height come into contact (in the circle in Fig. 3.15b), the width at this moment is the average width. So for one acid fracture, the ideal fracture width after the acid treatment is always larger than the average width occurring at the contact.

In order to inject acid into a fracture numerically, Mou (2009) presumed a small width between two fracture walls during acidizing. Then he simulated the acid transport and rock dissolution to obtain two rough surfaces etched by acid. Because of the presumed width, the breadth between two fracture walls is higher than the expectation. After the subtraction of the distance between two highest asperities, the average width becomes comparable to the ideal width in the experiments. Thus, I substitute the average width from numerical simulation for the ideal width in the empirical correlation to achieve the base conductivity.

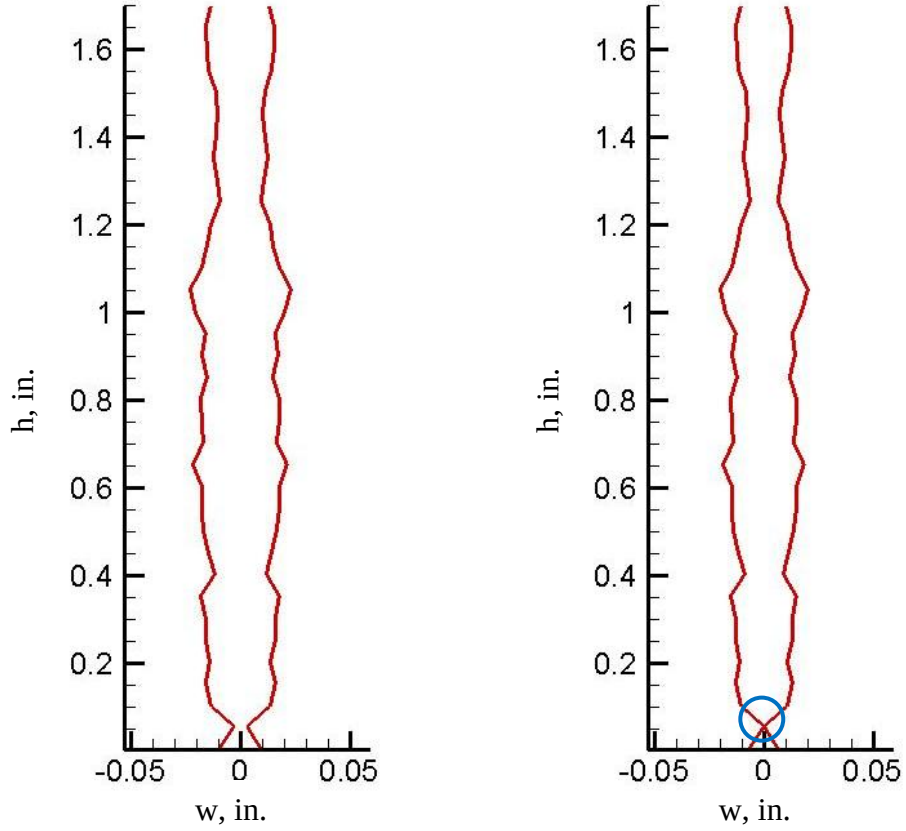

(a) Ideal Width **(b) Average Width**

Fig. 3.15—Example showing difference between ideal width and average width.

Another concern of base conductivity calculation is on rock strength. The empirical correlations based on experiments utilizes rock embedment strength, S_{RE}, while the numerical simulation employs the Young's modulus, E, to represent the rock strength. With the purpose of incorporating the base conductivity in the intermediate-scale simulation, the relationship between rock embedment strength and the Young's modulus needs to be explored. Our lab provided some rock strength measurements on numerous rock samples, including cream chalk, Indiana limestone, and San Andres

dolomite. The measurement data yields a linear relationship between the two types of rock strength,

$$S_{RE} = 0.0201E - 25137. \quad (3.9)$$

The rock embedment strength and the Young's modulus in the equation are both in psi. Notice that this relationship is based on the inadequate data the lab provided. The application of it is not universal. In practice, a better way to estimate rock strength is to measure the rock embedment strength, S_{RE}, and the Young's modulus, E, for the specific core samples in the rock mechanics lab.

With the average width from numerical simulation and the rock strength measurements, the empirical correlation developed by Nierode and Kruk (Eq. 1.6) provides base conductivity for the closed areas in the intermediate-scale simulation. The observation of the experimental width profile presented previously indicates the base conductivity accounts for the effect of roughness at the small scale. Additionally, the numerical simulation at the intermediate scale mostly captures the larger scale features, such as channels. Both roughness and channels contribute to the overall conductivity for a successful acid fracture. Therefore, the base conductivity plays an important role in the calculation.

3.2.3 Effect of Permeability Distribution

Different correlation lengths of permeability distributions result in different etching patterns, on which the fracture closure behavior highly depends. I show two examples of width profiles respectively for intermediate scale fractures before and after

closure. The average permeability for each case is 0.1 md. The only difference is the normalized correlation length in the horizontal direction. The first synthetic fracture shown in **Fig. 3.16** has a low normalized correlation length, $\lambda_{D,x}$=0.0156, in the horizontal direction. I observe that the openings in the fracture created by the Mou's models (2007) are isolated as a result of the weakly correlated permeability distribution. Under the different closure stresses, the closure models predict the width distributions. **Fig. 3.17** shows the width profiles under 1,000 and 5,000 psi closure stresses. More asperities touch and deform as the closure stress increases. The channels become even shorter and fewer openings are left.

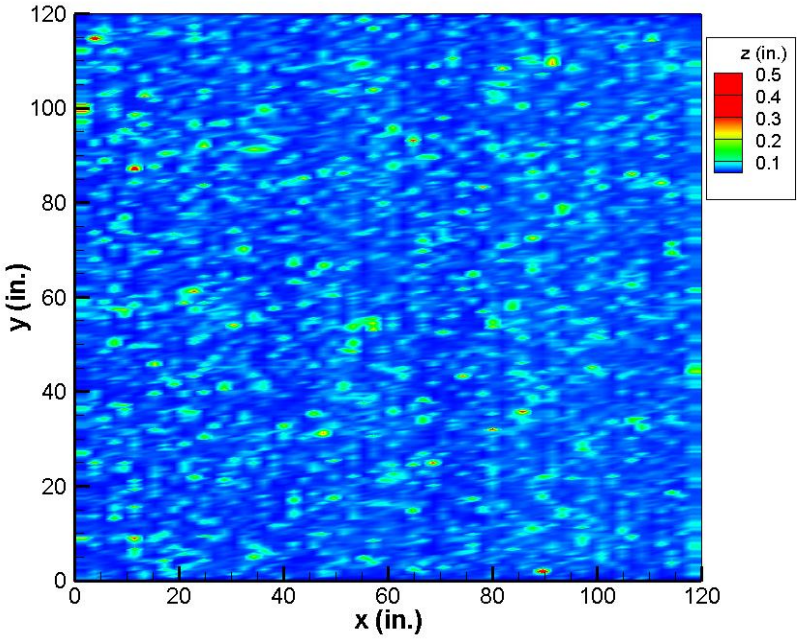

Fig. 3.16—Width profile after acidizing with a low horizontal correlation length at zero closure stress.

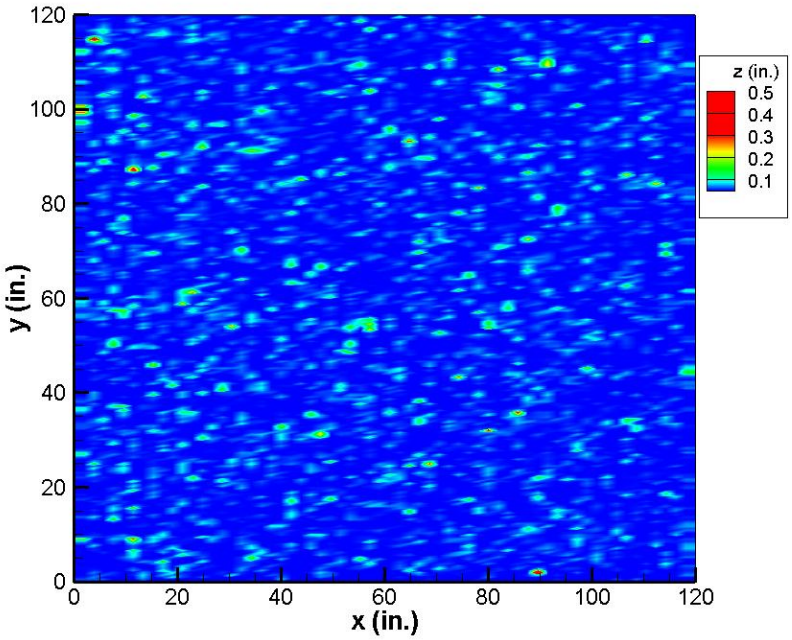

(a)—Closure Stress: 1000 psi

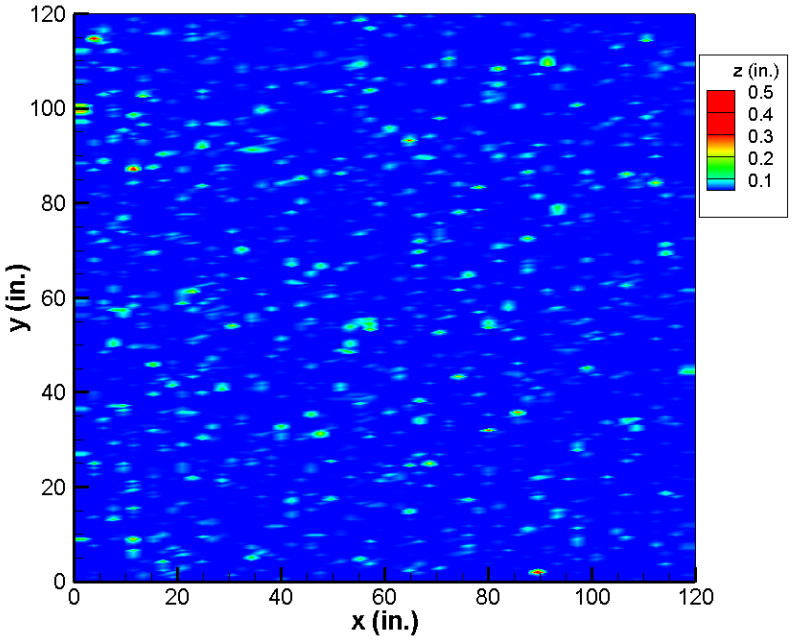

(b)—Closure Stress: 5000 psi

Fig. 3.17—Width profile under different closure stresses with a low horizontal correlation length.

In the second synthetic example shown in **Fig. 3.18**, many long, straight channels go through the whole fracture, because the normalized correlation length in the horizontal direction is $\lambda_{D,x}$=0.5, which is much higher than the first example shown in Fig. 3.16. The apertures are connected laterally to form long channels. The width profiles for closure stresses of 1,000 and 5,000 psi are shown in **Fig. 3.19**. The channels become shorter and narrower as the closure stress increases. Compared with the short, isolated openings in Fig. 3.17, these channels contribute more to the fracture conductivity, because the fluid flow in the channels is easier than between two rough surfaces.

From the figures above, I observe that the widths at some grids are zero and the apertures are closed completely in numerical simulations. In this case, the isolated channels do not result in any conductivity. However, that is not the case in reality. The intermediate simulator misses some information at small scale during the closure process, because the simulation domain for the intermediate scale is 10 by 10 feet. Every grid block is in inches, which is at the same order as the experimental one. The roughness observed in the lab also contributes to the fracture conductivity. Thus, I assign base conductivity, which was described in previous section, in those closed grids accounting for small-scale roughness features when calculating the conductivity for intermediate scale fractures.

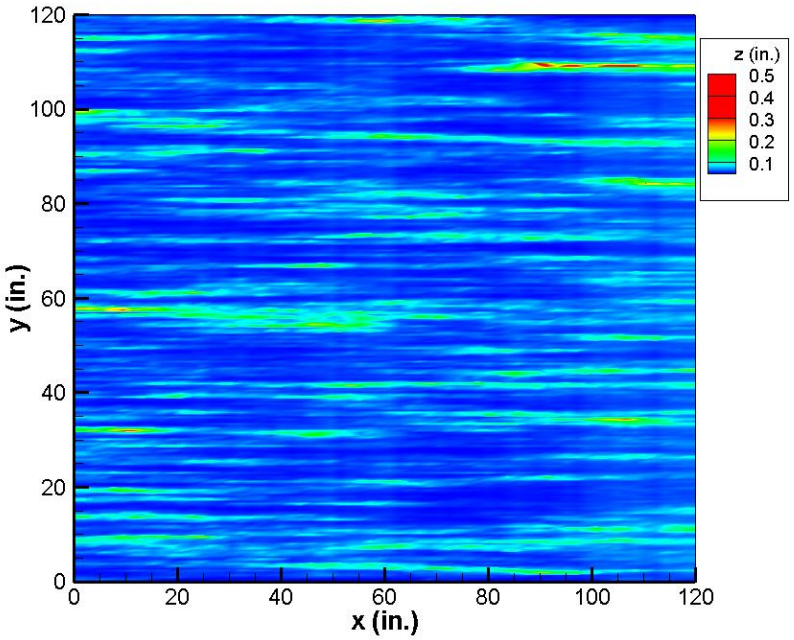

Fig. 3.18—Width profile after acidizing with a high horizontal correlation length at zero closure stress.

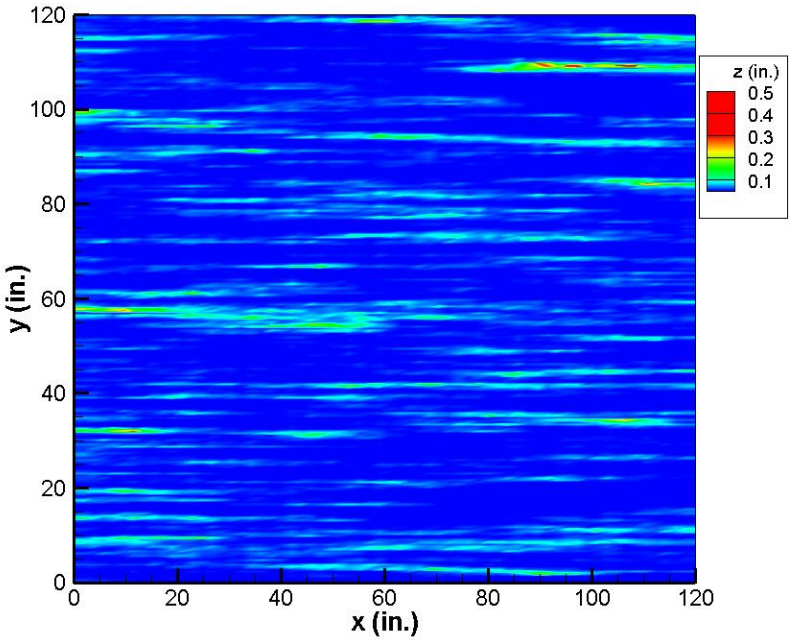

(a)—Closure Stress: 1000 psi

Fig. 3.19—Width profile under different closure stresses with a high horizontal correlation length.

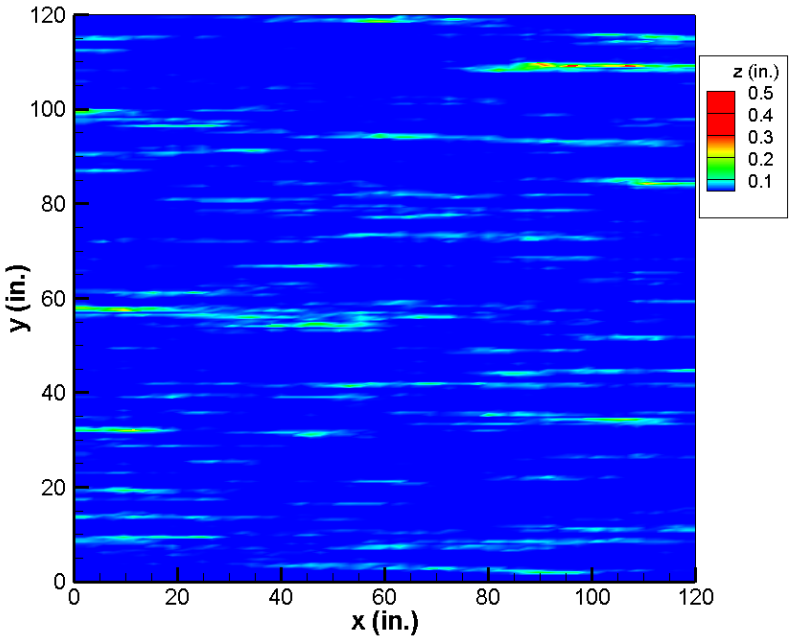

(b)—Closure Stress: 5000 psi

Fig. 3.19 Continued

After the application of the base conductivity, I compute the fracture conductivity for the two examples above. **Figs. 3.20 and 3.21** show conductivity curves with respect to closure stresses in semilog plots for acid fractures corresponding to the cases. **Table 3.5** shows the calculated values. The only difference between these two cases is the horizontal correlation length. When the correlation length is low (Fig. 3.20, $\lambda_{D,x}$=0.0156), the fracture conductivity is getting close to the base conductivity especially under high closure stresses. In Fig. 3.21, the horizontal correlation length for permeability field is $\lambda_{D,x}$=0.5, which means channels go through the entire fracture. The channels result in higher conductivities, even though the base conductivities are smaller than the low correlation length case. Considering the logarithm scale, I observe that the

channel flow dominates in the fracture. Therefore, the contribution of channels to the fracture conductivity highly depends on correlation lengths of permeability distributions.

TABLE 3.5—FRACTURE CONDUCTIVITY WITH RESPECT TO CLSOURE STRESSES AT INTERMEDIATE SCALE

Closure Stress, psi	Low Horizontal Correlation Length		High Horizontal Correlation Length	
	Base Cond., md-ft	Fracture Cond., md-ft	Base Cond., md-ft	Fracture Cond., md-ft
0	17,535	355,782	19,072	2,669,092
300	13,513	69,415	14,698	996,398
1,000	7,358	19,961	8,002	355,692
2,000	3,087	6,246	3,358	117,822
3,000	1,295	2,211	1,409	41,116
4,000	543	861	591	13,428
5,000	228	337	248	4,909

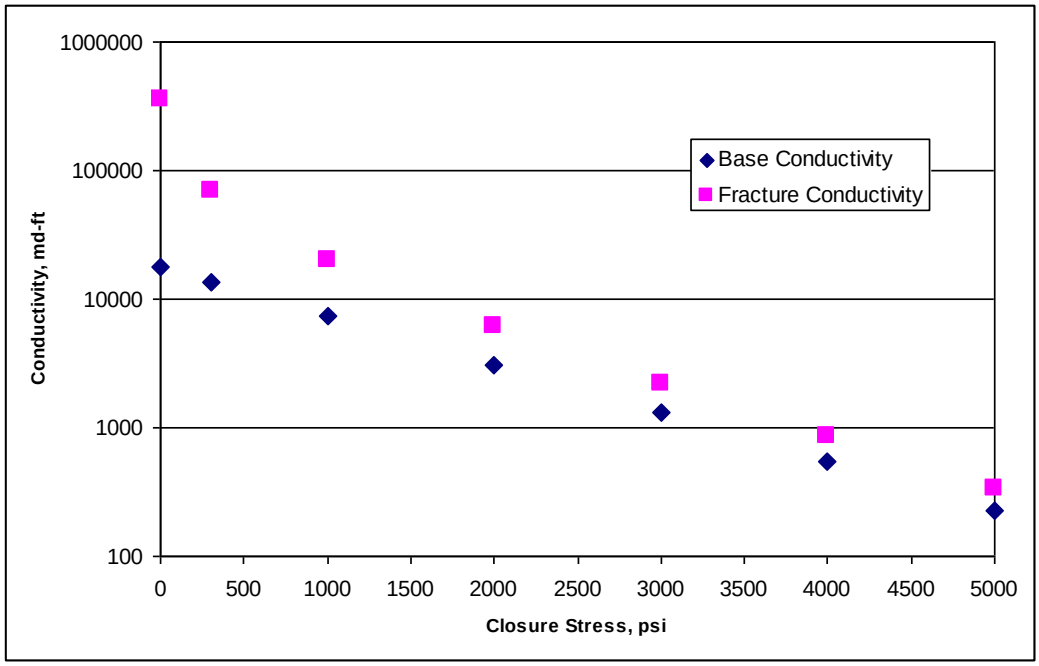

Fig. 3.20—Fracture conductivity with respect to closure stresses with low horizontal correlation length.

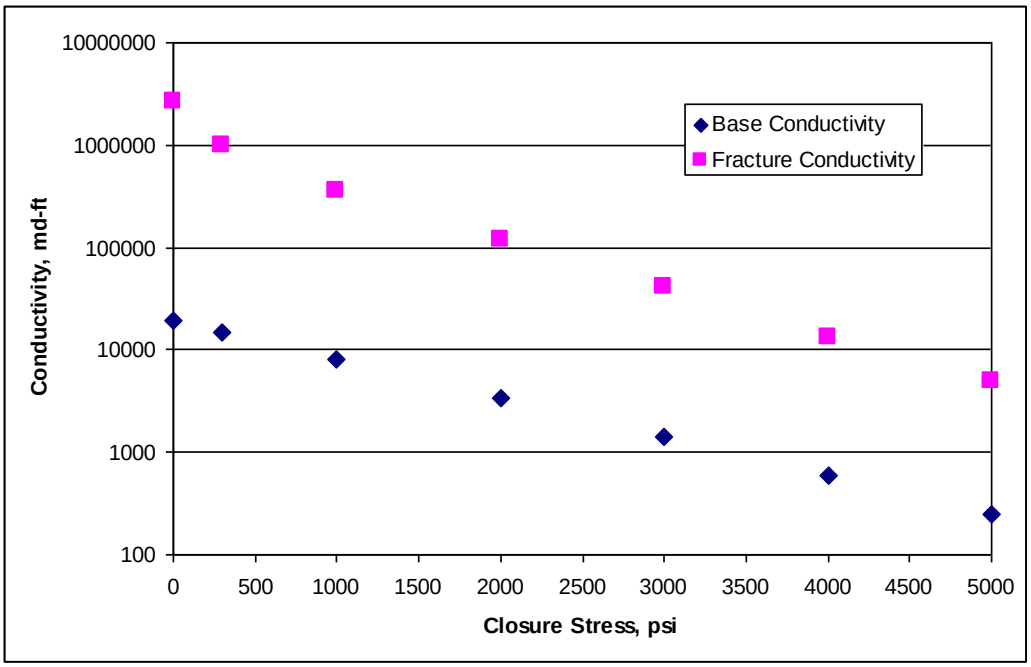

Fig. 3.21—Fracture conductivity with respect to closure stresses with high horizontal correlation length.

In order to show the effect of the normalized horizontal correlation length on the overall conductivity more clearly, **Fig. 3.22** presents the relationship between them under the same closure stress of 5,000 psi. Notice that the plot axes are logarithm scales. The convex curve in the log-log plot implies that the horizontal correlation length affects the conductivity significantly. The higher horizontal correlation length leads to the formation of more channels. The channels going through the fracture are the main contribution to the overall conductivity.

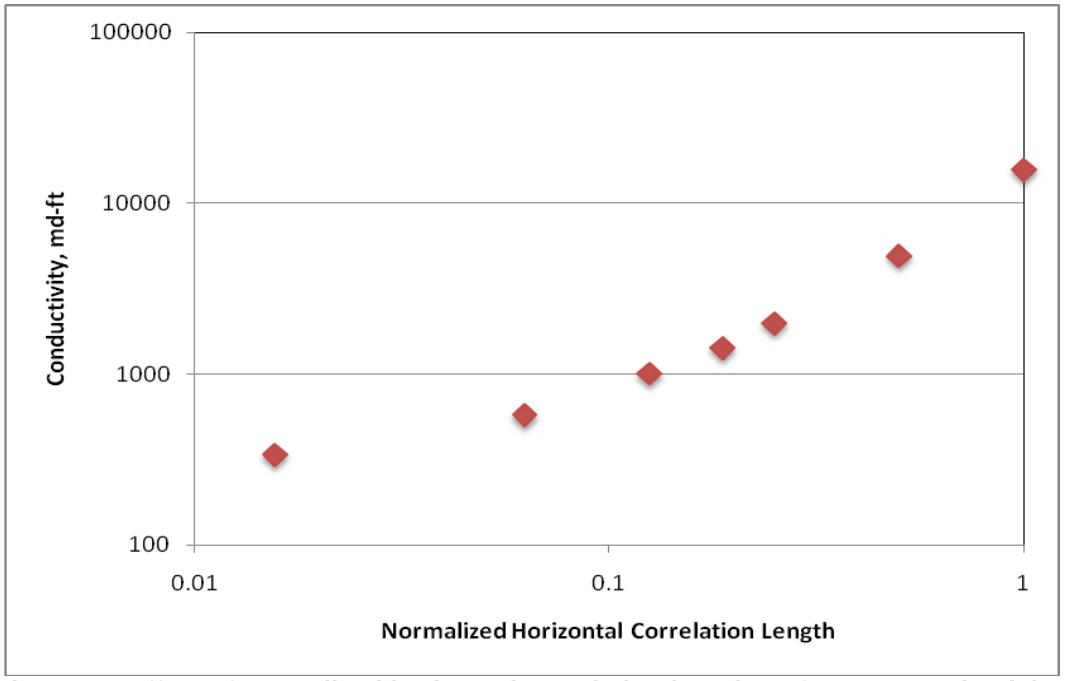

Fig. 3.22—Effect of normalized horizontal correlation length on fracture conductivity.

Vertical correlation length is another key parameter that influences the etching pattern and the closure behavior. The following two examples show the difference between two cases with low and high vertical correlation lengths. The average permeability for each case is 0.1 md, and the horizontal correlation length is 0.25. The first synthetic case (**Fig. 3.23**) has a low vertical correlation length, $\lambda_{D,z}$=0.004. The channels etched by acid are very narrow because of the weakly correlated permeability in the vertical direction. With the same order of the fracture width, the narrower channels are more difficult to close. Therefore, a lot of channels are still open under the closure stress of 3,000 psi as shown in **Fig. 3.24**.

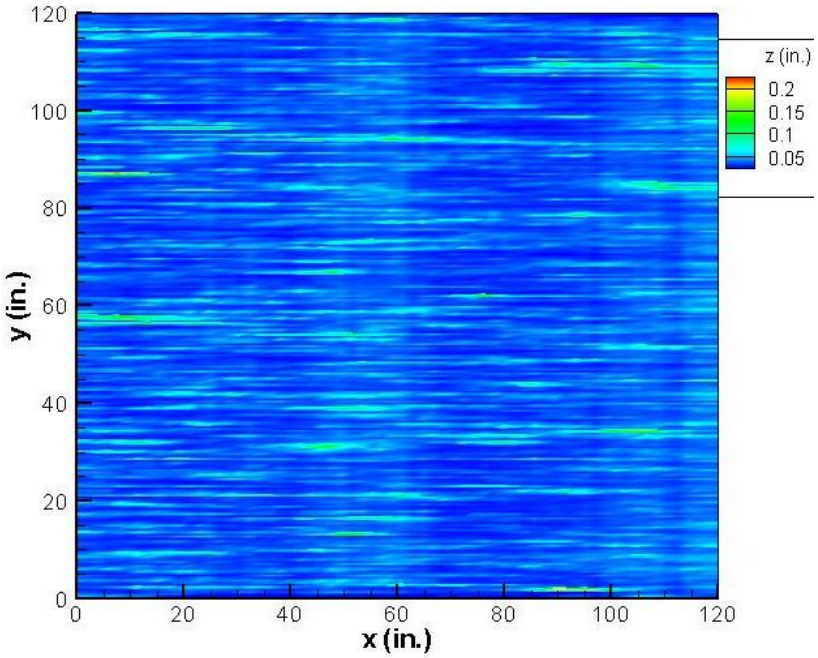

Fig. 3.23—Width profile after acidizing with a low vertical correlation length at zero closure stress.

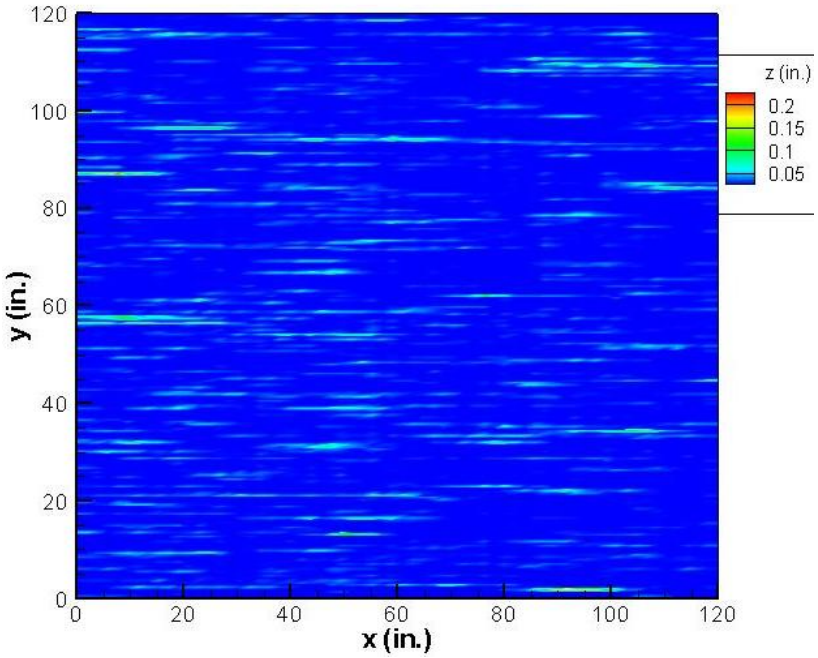

Fig. 3.24—Width profile under the closure stress 3,000 psi with a low vertical correlation length.

In contrast to the first case, the second one has a permeability distribution with a high vertical correlation length, $\lambda_{D,z}$=0.25. Even though the horizontal correlation length for both cases is the same, $\lambda_{D,x}$=0.25, the acid etched fracture (**Fig. 3.25**) has more vugs than channels. It results in the low elliptical aspect ratio when I simulate the closure behavior of every cross-section approached by ellipses. That is the reason why only few openings are observed under the same closure stress of 3,000 psi as shown in **Fig. 3.26**. In this case, the roughness is the main contributor to the conductivity while the isolated vugs play an insignificant role.

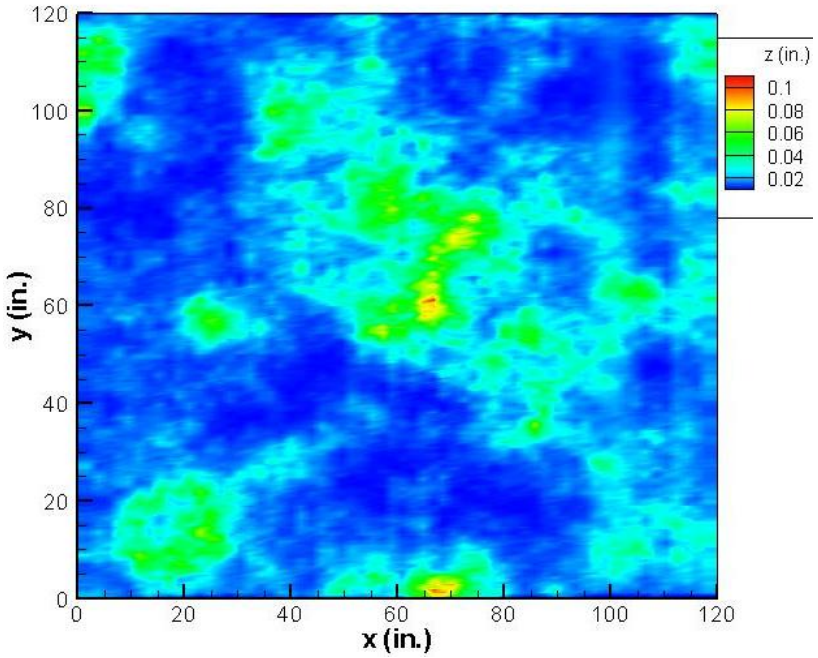

Fig. 3.25—Width profile after acidizing with a high vertical correlation length at zero closure stress.

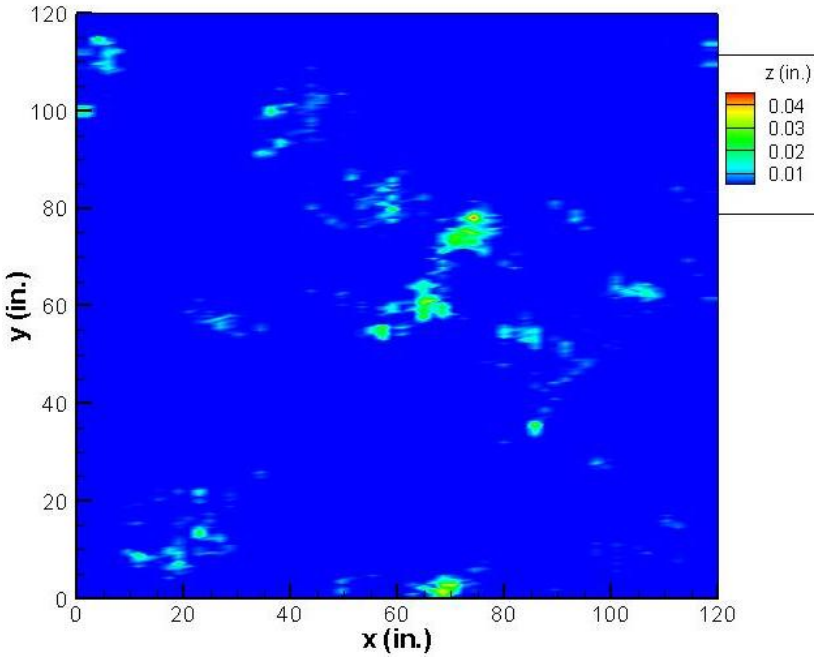

Fig. 3.26—Width profile under the closure stress 3,000 psi with a high vertical correlation length.

The conductivity comparison of these two synthetic cases in **Fig. 3.27** reveals the discussion above. Especially under low closure stress, the conductivity of the low vertical correlation length case decreases slower than the high vertical correlation length case, because the narrow channels in the first case remain open. The wide "channels" in the second case crush even under low closure stress. The conductivity change under high closure stress is mainly caused by the deformation of the roughness. So the changing trend is similar to each other. But under the same closure stress, the difference of the conductivities is the result of the different amount of open channels for each fracture.

The effect of vertical correlation length on overall fracture conductivity is shown in **Fig. 3.28**. The cases in the plot have the same horizontal correlation length 0.25 and closure stress 3,000 psi. In the log-log plot, the relationship looks nearly linear.

Compared with the horizontal correlation length, the vertical one has the inverse effect on the conductivity. Both of them influence the etching pattern and closure behavior significantly. But in practice, the vertical correlation length is normally very small as a result of the feature of laminations in sedimentary carbonate rocks.

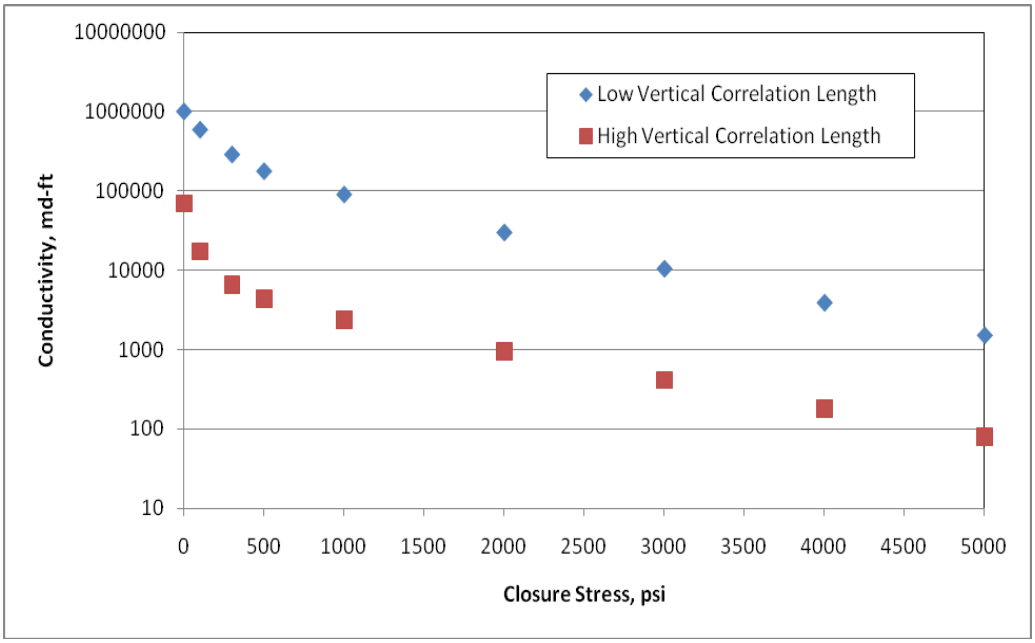

Fig. 3.27—Conductivity comparison with different vertical correlation lengths.

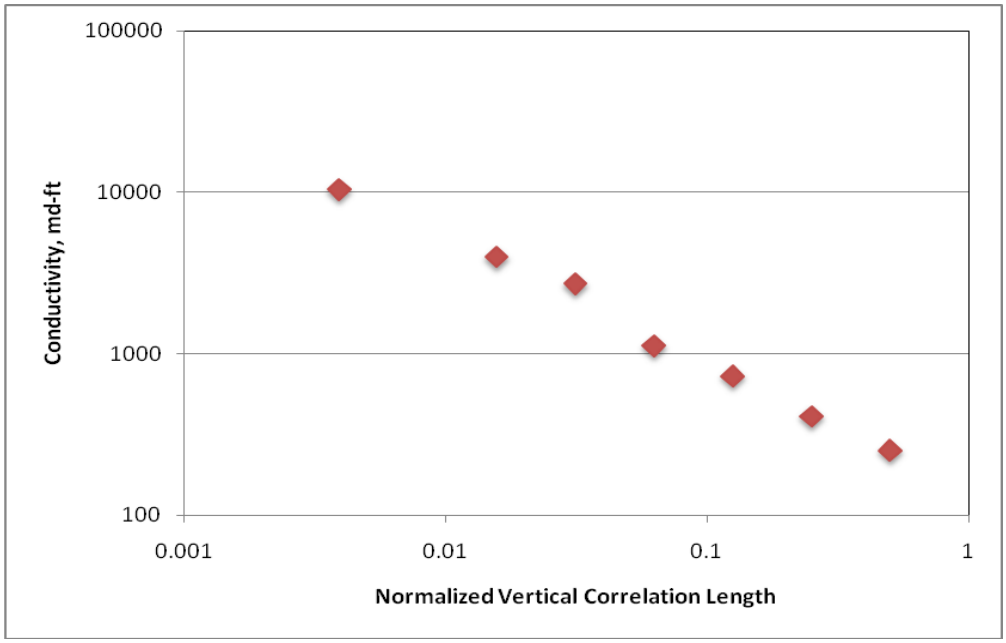

Fig. 3.28—Effect of normalized vertical correlation length on fracture conductivity.

Normalized standard deviation is one of the statistical parameters that characterize the permeability distribution. It represents the permeability variation from the average permeability. The following two examples illustrate the effect of normalized standard deviation on overall fracture conductivity. Except for the standard deviation, they have the same average permeability of 0.1 md, vertical correlation length of 0.016, and horizontal correlation length of 0.5. Young's modulus is 3 Mpsi for both examples. The case shown in **Fig. 3.29** has a low standard deviation, σ_D=0.1. **Fig. 3.30** presents the width distribution after closure under closure stress of 3,000 psi.

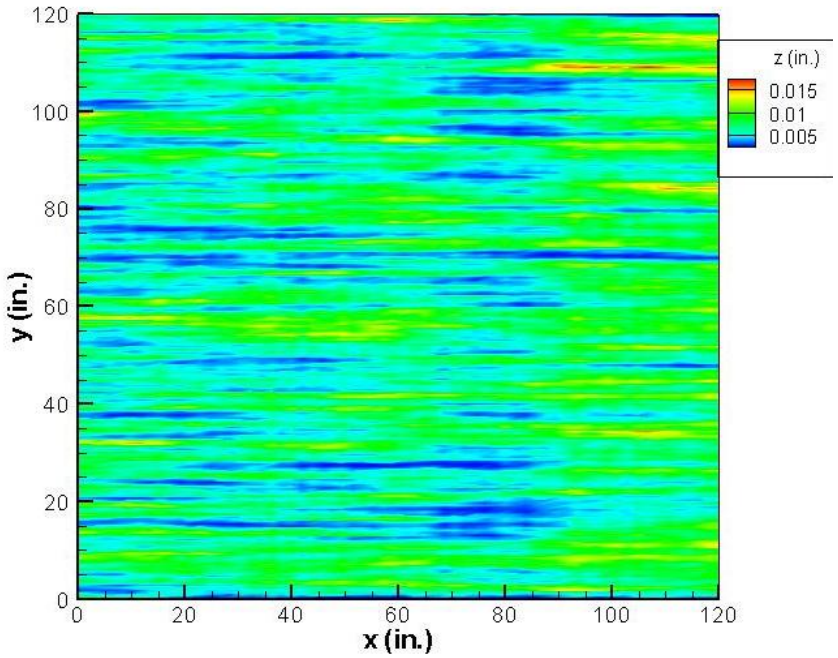

Fig. 3.29—Width profile after acidizing with a low standard deviation at zero closure stress.

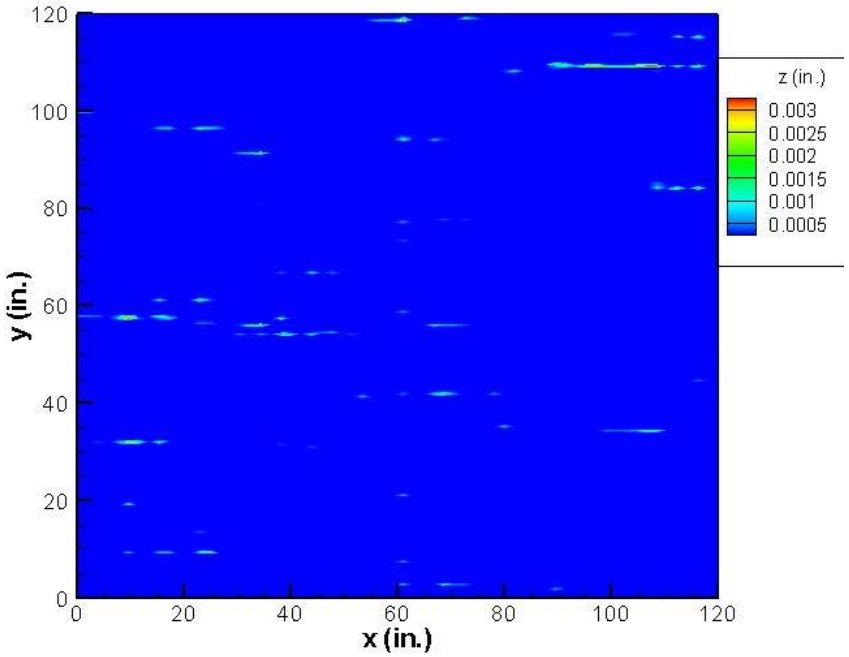

Fig. 3.30—Width profile under the closure stress 3,000 psi with a low standard deviation.

Compared to the case with high standard deviation, σ_D=0.5, shown in **Fig. 3.31**, the greener profile of the first case demonstrates that the width does not vary much from the average width around 0.01 inches. The high standard deviation yields the bluer width profile for the second case below. Obviously, the channel depth for the second case is greater. So under the same closure stress, the channels in the first fracture are easier to close while more openings are left for the fluid flow in the second fracture (**Fig. 3.32**). The higher overall conductivity can be expected for the second case with high standard deviation.

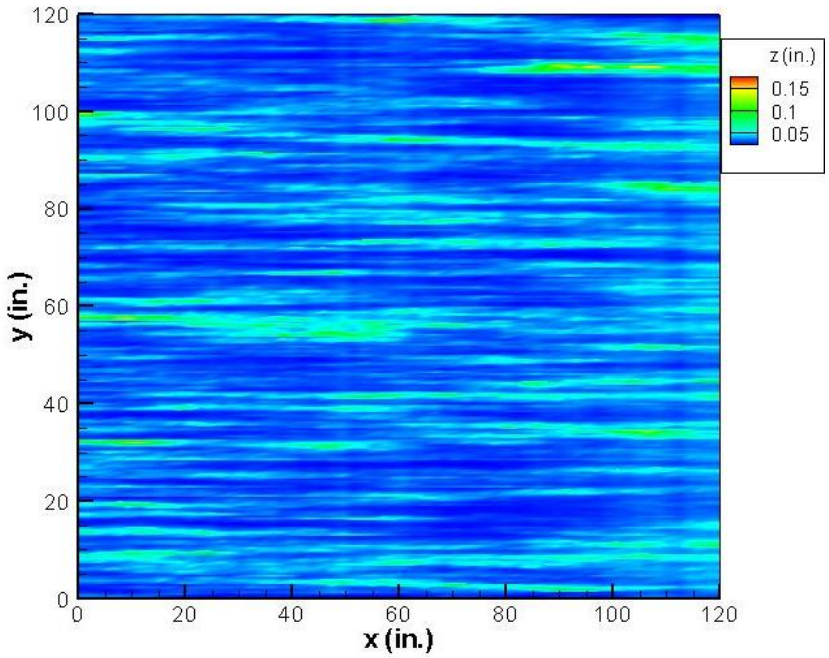

Fig. 3.31—Width profile after acidizing with a high standard deviation at zero closure stress.

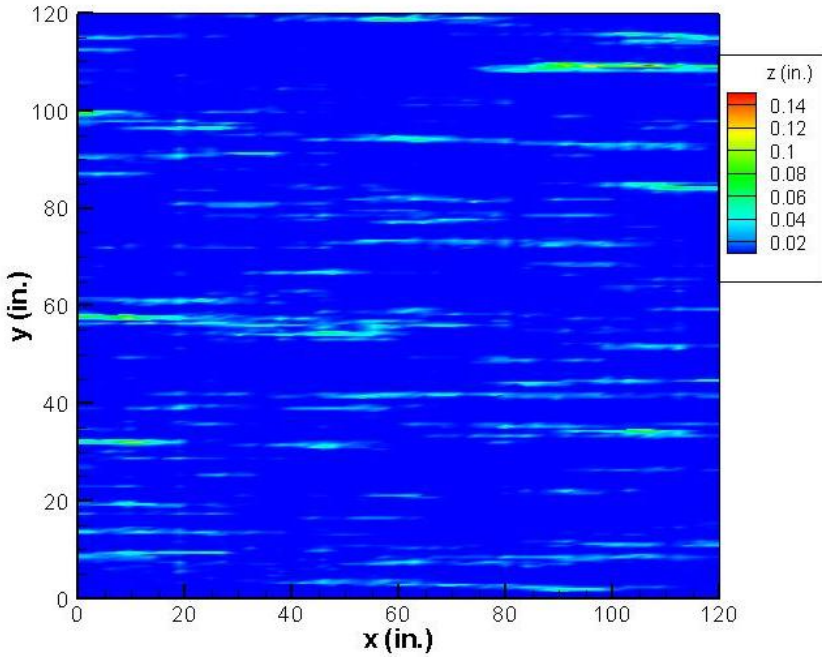

Fig. 3.32—Width profile under the closure stress 3,000 psi with a high standard deviation.

The conductivity with respect to the closure stress for the examples above is also plotted in **Fig. 3.33**. The conductivity of the low standard deviation case declines dramatically even under low closure stress. The relatively even fracture surfaces become flat quickly. In contrast, the high standard deviation case maintains the fracture conductivity quite well with many channels remaining open.

In **Fig. 3.34**, I present the conductivity versus the normalized standard deviation. On the semi log plot, the relationship between them is almost linear. If normalized standard deviation is higher, etching pattern will be more uneven, and channels will be deeper. Rough fracture surfaces and deep channels are the most important features that favor high overall conductivity for an acid fracture.

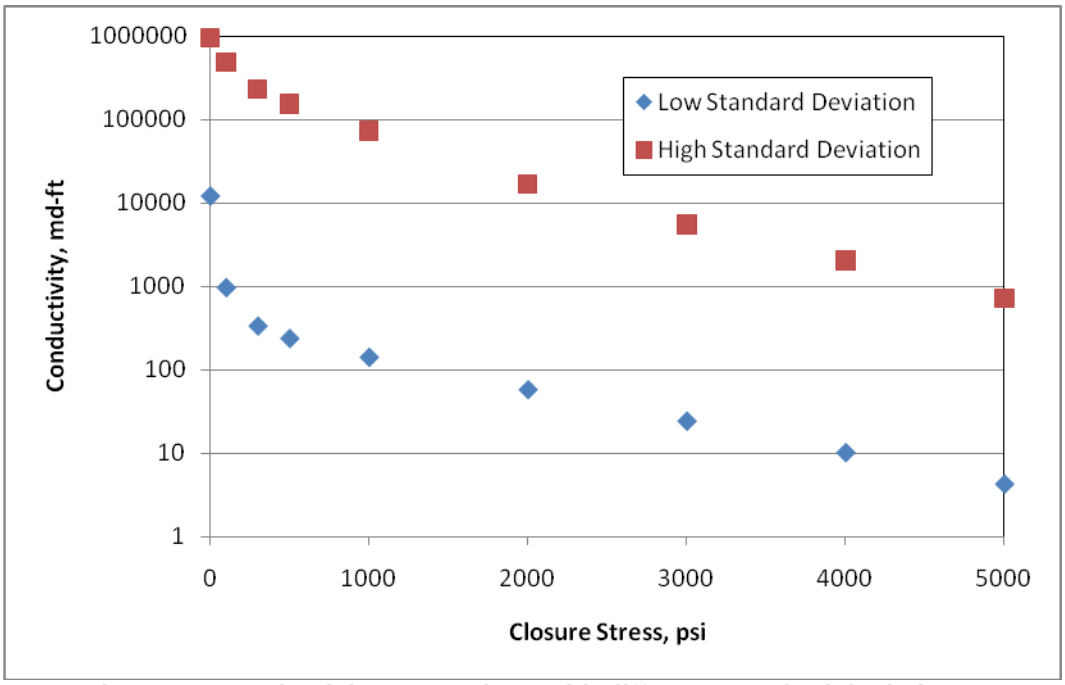

Fig. 3.33—Conductivity comparison with different standard deviations.

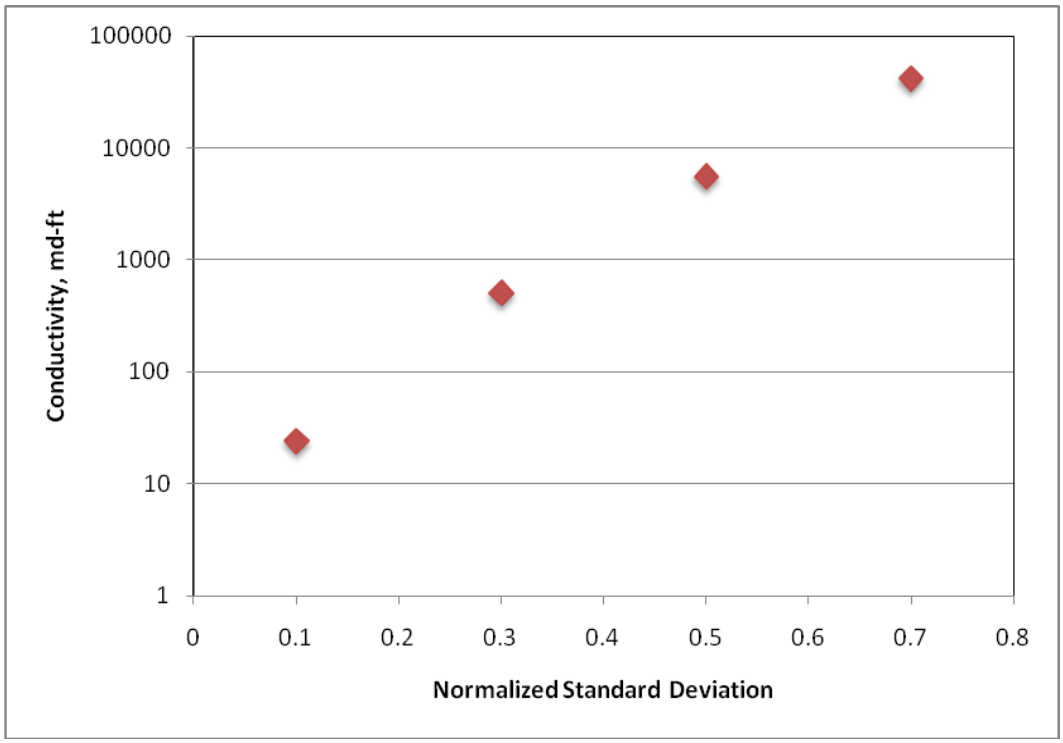

Fig. 3.34—Effect of normalized vertical correlation length on fracture conductivity.

3.2.4 Effect of Mineralogy Distribution

Mineralogy distribution is another principal input in the model. Acid fracturing is essentially a stimulation method implemented in carbonate reservoir. The carbonate rock mainly consists of limestone and dolomite. So in this study, we consider just limestone and dolomite and neglect other kinds of rock. Mineralogy determines the acid/rock reaction rate. Limestone reacts with acid faster than dolomite, so rock is dissolved more for limestone than dolomite. The various reaction rates yield rough fracture surfaces.

According to Blatt (1980), most carbonate sediments show laminations. It indicates that the mineralogy distribution has a high correlation length in the bedding direction. The mineralogy will be changed abruptly without transition. Therefore, we use a strong horizontal correlation length to generate mineralogy distributions. As a result, the channels form easily when mineralogy distribution dominates the surface etching patterns.

Mou (2009) suggested that the vertical correlation length of mineralogy distribution does not affect conductivity at zero closure stress. Instead, the percentage of limestone and dolomite affects the etching patterns because of the variation of the reaction rates. The higher percentage of limestone leads to the larger average fracture width for a certain acid contact time. Thus, I follow Mou's steps and investigate the effect of limestone percentage on fracture overall conductivity.

Mou (2009) did not perform simulation with limestone percentage lower than 20% because small limestone percentage gives discontinuous channels that result in little conductivity. Therefore, two examples shown below have limestone percentage 20% and

40%, respectively. They have a high horizontal correlation length and a low vertical one for the mineralogy distributions. **Fig. 3.35** shows the width profile after acid treatment when the limestone percentage is 20%, while **Fig. 3.36** is the width profile after the fracture is closed under the closure stress of 3,000 psi. The case with higher limestone percentage of 40% is shown in **Fig. 3.37** and **Fig. 3.38**, respectively.

The variation of reaction rates initiates the formation of channels. The intense etching happens where limestone is present because it reacts faster than dolomite. As the limestone percentage increases, more channels are created. Consequently, more channels are open for fluid flow after deformation caused by the closure stress. Therefore, higher conductivity can occur for the case with higher limestone percentage.

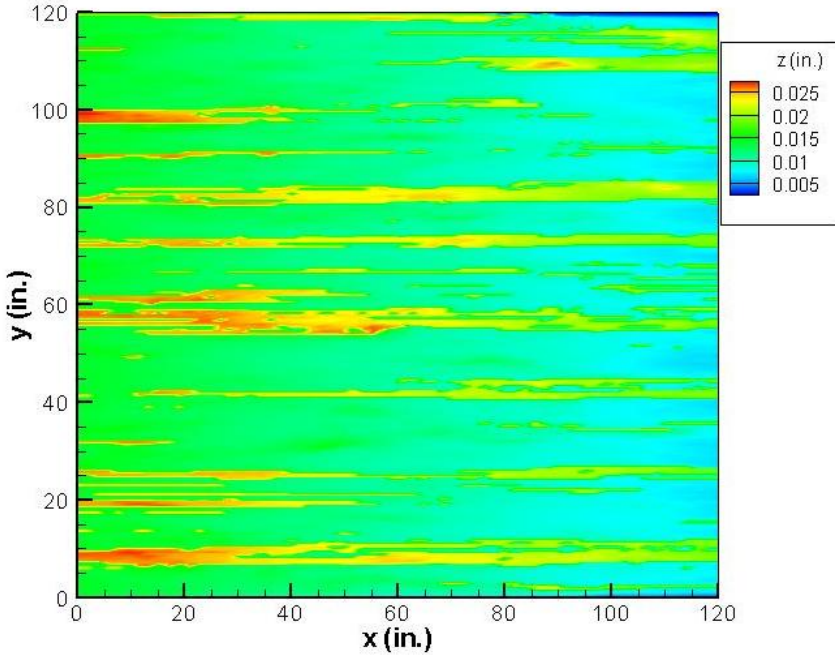

Fig. 3.35—Width profile after acidizing with a low limestone percentage at zero closure stress.

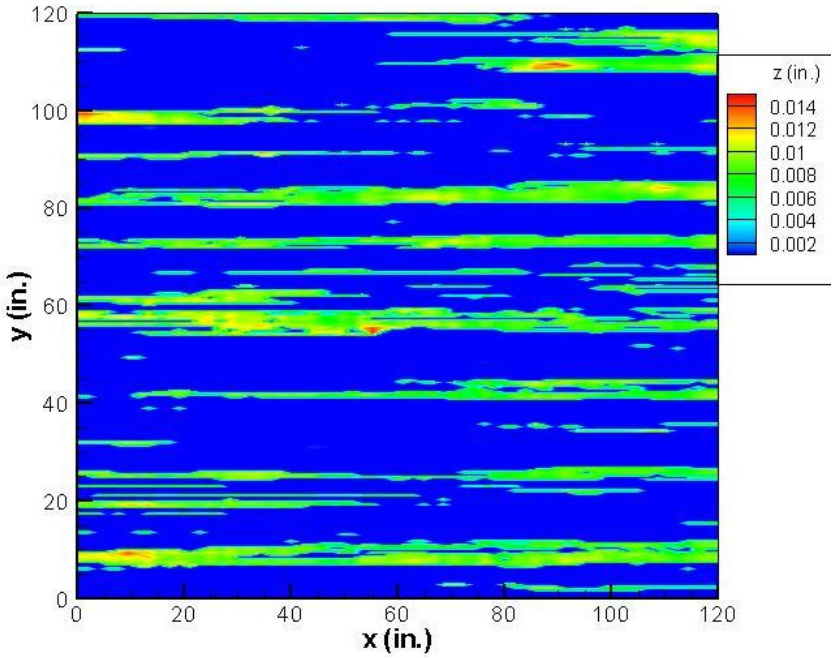

Fig. 3.36—Width profile under the closure stress 3,000 psi with a low limestone percentage.

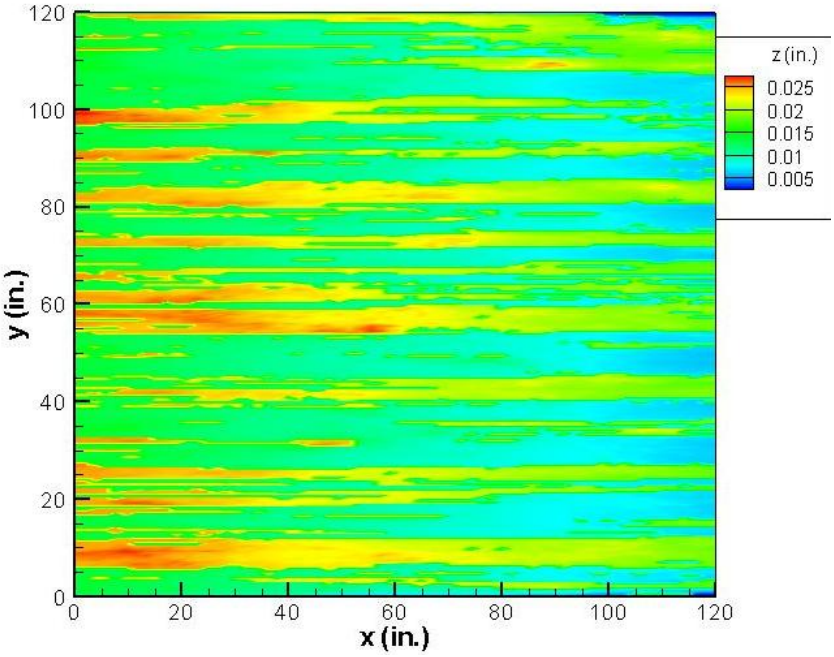

Fig. 3.37—Width profile after acidizing with a high limestone percentage at zero closure stress.

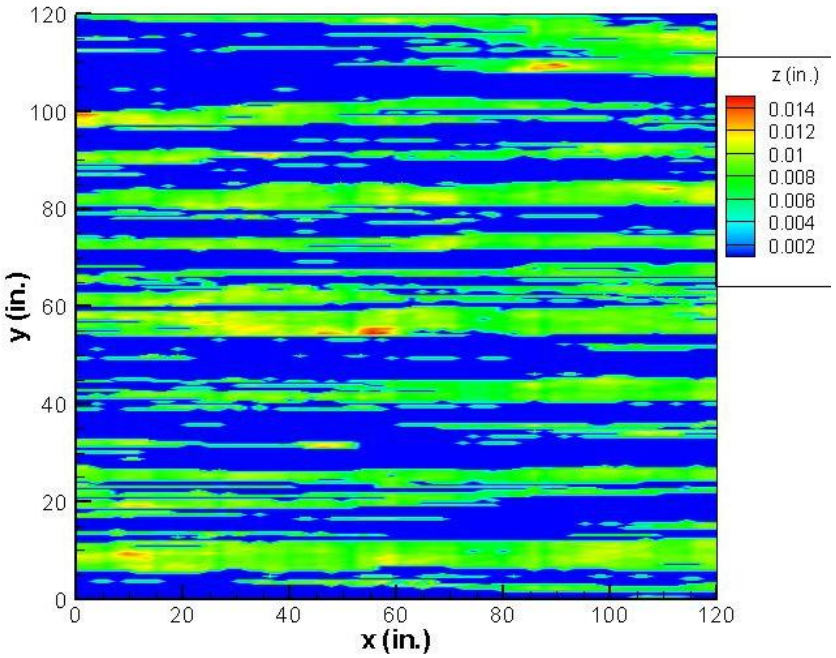

Fig. 3.38—Width profile under the closure stress 3,000 psi with a high limestone percentage.

In **Fig. 3.39**, conductivity for both cases above is presented with respect to closure stress. As the previous estimation, higher limestone percentage yields higher fracture conductivity at the same closure stress. Observe that the closure behavior for both examples is very similar because the trend for both curves is nearly the same. It indicates that the amount of channels, but not the deformation of channels, is the main factor for the conductivity calculation. And the amount of channels highly depends on the mineralogy percentage.

In order to study the effect of mineralogy on fracture conductivity, I plotted conductivity as limestone percentage increases (**Fig. 3.40**). For each data point, all other parameters are the same except the limestone percentage. From 10% to 50%, the conductivity increases almost linearly with respect of the limestone percentage. The

conductivity curve trend may reach the peak and go down after the limestone percentage is higher 50%. We can imagine that the etching pattern will be dramatically even when the fracture surface consists of limestone only (100%). In this case, no channel will appear and contribute to the overall conductivity. In this study, the model simulates the cases with limestone percentage less than 50%. The deformation behavior and overall conductivity for a fracture with limestone percentage higher than 50% still needs further study.

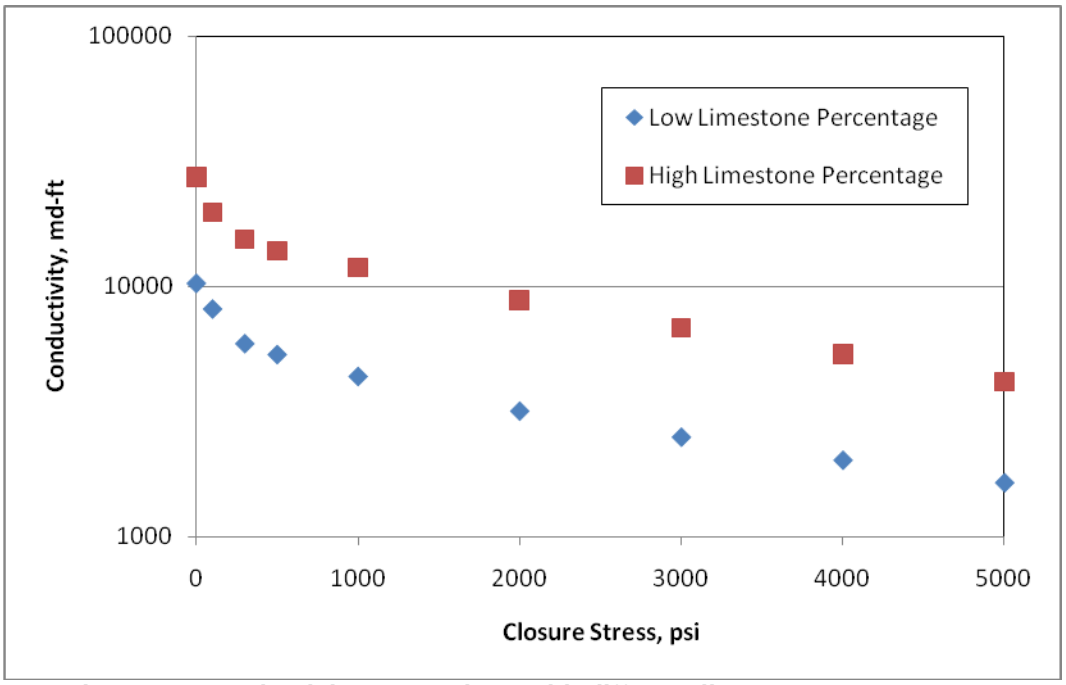

Fig. 3.39—Conductivity comparison with different limestone percentages.

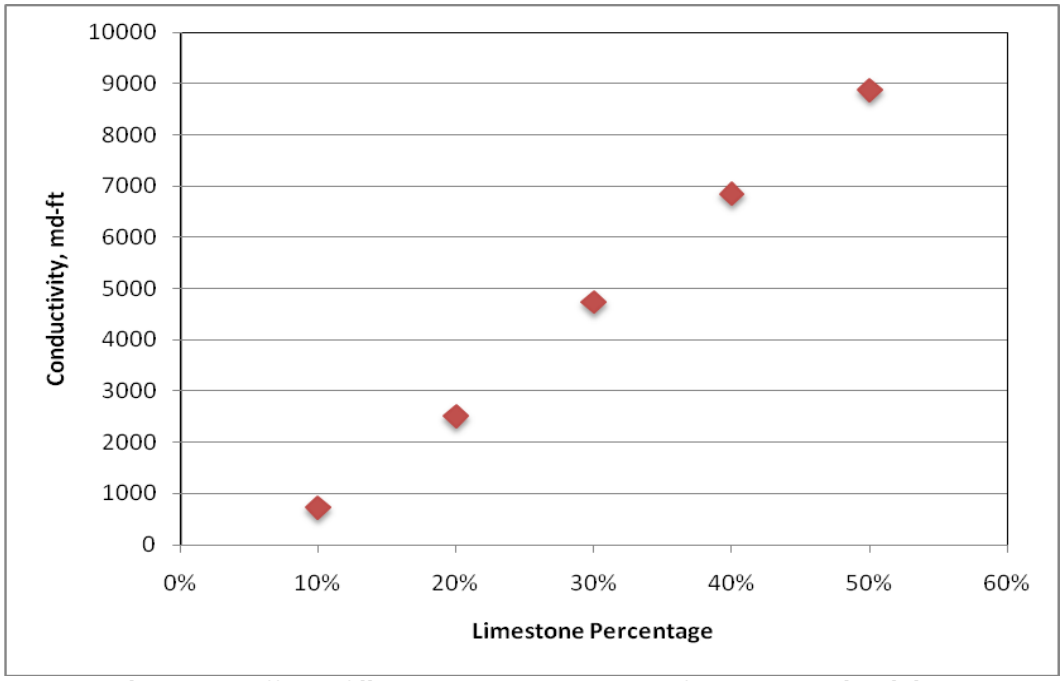

Fig. 3.40—Effect of limestone percentage on fracture conductivity.

3.2.5 Effect of Rock Properties

With the assumption of elasticity, two parameters represent the rock properties: Poisson's ratio and Young's modulus. In this section, I study the effect of these two parameters on fracture overall conductivity.

Poisson's ratio, ν, is the ratio of the contraction or transverse strain (perpendicular to the applied load) to the extension or axial strain (along the applied load). Gercek (2007) investigated Poisson's ratio values for rocks. The typical range of Poisson's ratio for dolomite is about from 0.1 to 0.35, while the normal range for limestone is roughly from 0.1 to 0.33, which is very close to dolomite. Therefore, the Poisson's ratio for carbonate in this study is higher than 0.1, but lower than 0.4.

In order to study the effect of Poisson's ratio, I set up an example and keep all the parameters the same except the Poisson's ratio. The permeability distribution for this

case has a high horizontal correlation length, a low vertical correlation length and a high standard deviation. With the constant Young's modulus 3 Mpsi, fracture overall conductivity is plotted with respect to Poisson's ratio in **Fig. 3.41**.

Although the Poisson's ratio changes from 0.1 to 0.4, the observation reveals that the results of conductivity are very close to each other at a certain closure stress. Some slight difference can be found under high closure stress such as 7,000 psi in this case. From the analysis, Poisson's ratio of carbonate does not affect fracture overall conductivity significantly. In this study, I ignore the effect of Poisson's ratio and set a typical value, 0.3, for it in the numerical experiments.

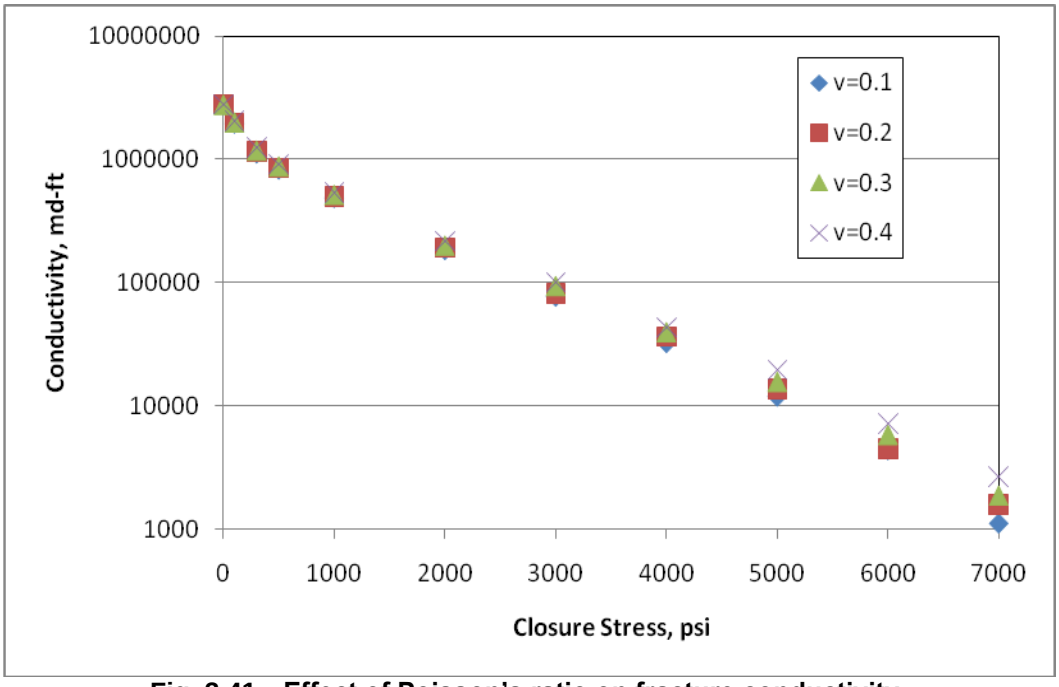

Fig. 3.41—Effect of Poisson's ratio on fracture conductivity.

Similar to rock embedment strength in experiments, Young's modulus is a measure of the strength of rock in the quantitative analysis and calculation. The

definition of Young's modulus is the ratio of the uniaxial stress over the uniaxial strain when the material is elastic. It can be determined from the slope of a stress-strain curve created during tensile tests conducted on a rock sample.

Young's modulus plays an important role during the fracture closure process. When the Young's modulus is high, the rock is strong and not easy to deform under closure stress. Then many openings lead to high fracture conductivity. For demonstration, one acid fracture below deforms with different Young's moduli. It is the same example as shown in the Poisson's ratio section. But the Young's modulus changes instead of the Poisson's ratio.

The width profile after acidizing is shown in **Fig. 3.42**. Some deep channels appear and go through the fracture domain. Under the same closure stress 5,000 psi, **Fig. 3.43** shows the width profile of the fracture with a low Young's modulus of 2 Mpsi, while **Fig. 3.44** shows the case with a high Young's modulus of 4 Mpsi. With the purpose of more straightforward illustration, I also list the average width information as follow. The average width before closure is 0.0635 inches. With the low Young's modulus, the average width after closure becomes 0.0127 inches. In contrast, the average width for the high Young's modulus case is 0.0176 inches. Therefore, the rock with the higher Young's modulus stands more strongly and retains more openings under the same closure stress when the average width is approximately 38% more than the other one with the lower rock strength. According to the cubic law or other models, fracture conductivity is very sensitive to fracture width, so the fracture with greater width will have greater conductivity.

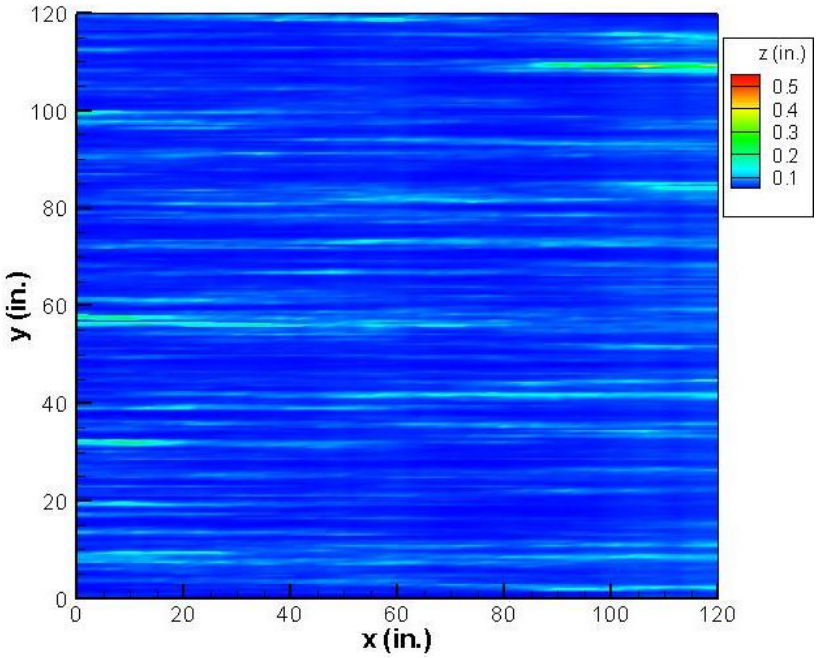

Fig. 3.42—Width profile after acidizing at zero closure stress.

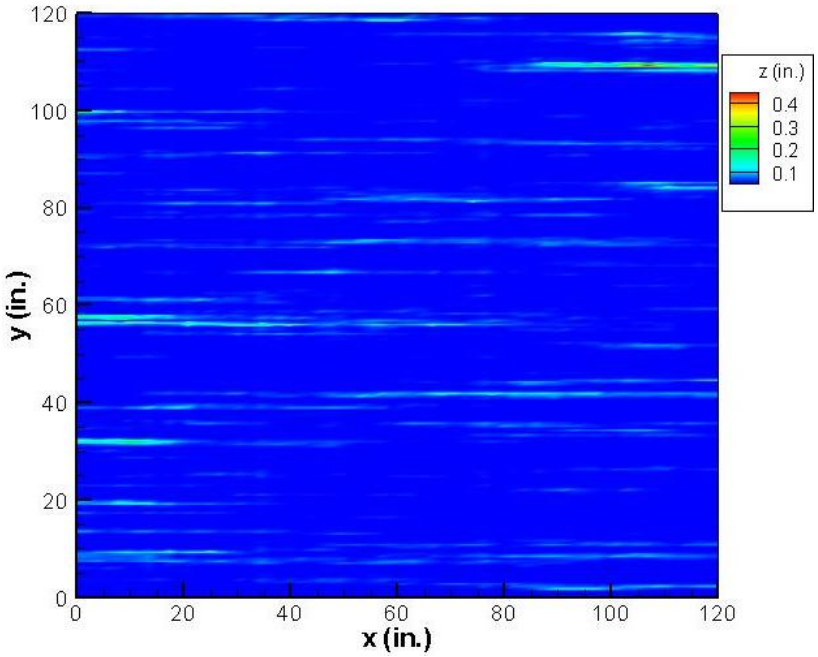

Fig. 3.43—Width profile under the closure stress 5,000 psi with a low Young's modulus.

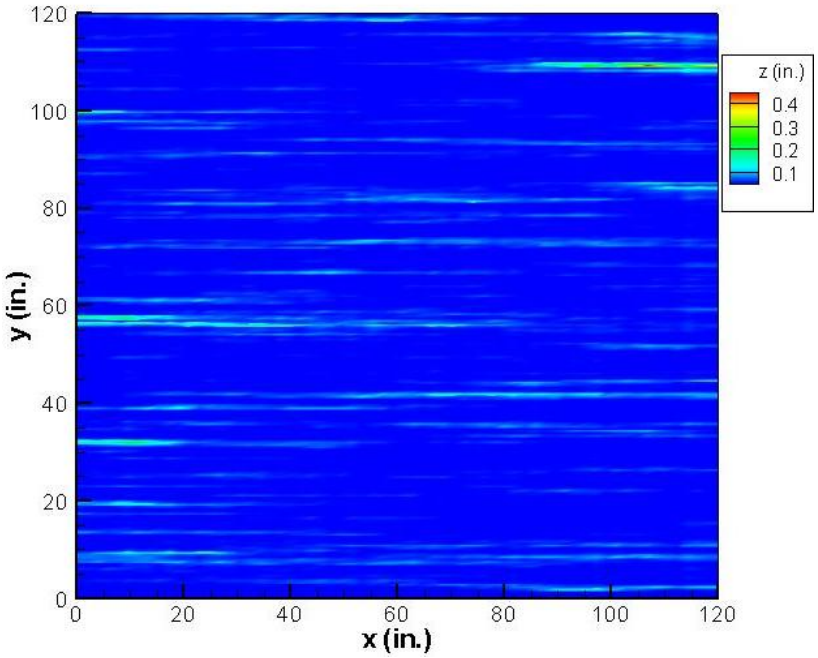

Fig. 3.44—Width profile under the closure stress 5,000 psi with a high Young's modulus.

From **Fig. 3.45** below, I can confirm the conclusion discussed previously. For the same example shown in Fig. 3.42, the Young's modulus ranges from 2 Mpsi to 4.5 Mpsi. The *y* axis of conductivity is a logarithmic scale. When the closure stress is low, the difference does not look tremendous and results are at the same order of magnitude. As the closure stress increases, the curves diverge and the variation becomes large. Especially for the soft rock with the Young's modulus 2 Mpsi, the conductivity drops much faster than other cases. Also, the rising closure stress reveals noticeable variations among the cases with different Young's modulus.

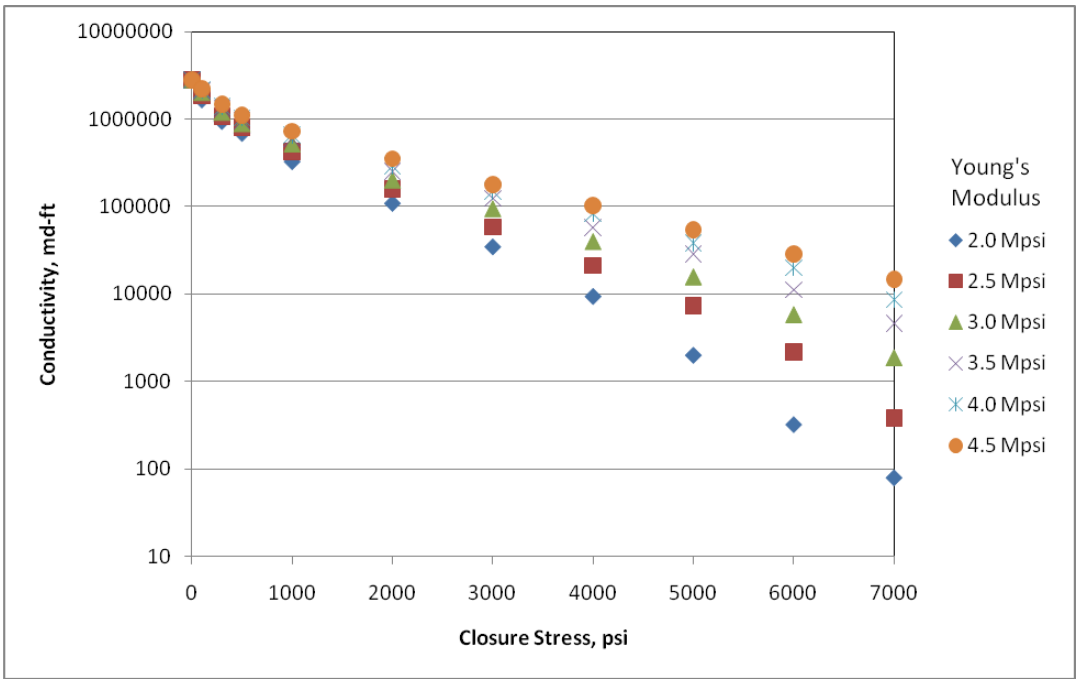

Fig. 3.45—Conductivity calculation with different Young's moduli.

To clarify the effect of Young's modulus more, **Fig. 3.46** plots the relationship between the conductivity and the Young's modulus under the same closure stress 7,000 psi. The convex curve implies the significant effect of Young's modulus. In particular, the high Young's modulus, which means the strong rock, gives more openings for fluid flow and yields high fracture conductivity. In general, dolomite is stronger than limestone. If the etching pattern is the same, dolomite will have a better performance to flow petroleum fluid than limestone. But percentage of limestone in rock has positive feedback on conductivity as discussed previously. Thus, more limestone in rock leads to more etching and deeper channels, but softer asperities that resist the closure stress weakly. This dilemma about conductivity needs further study.

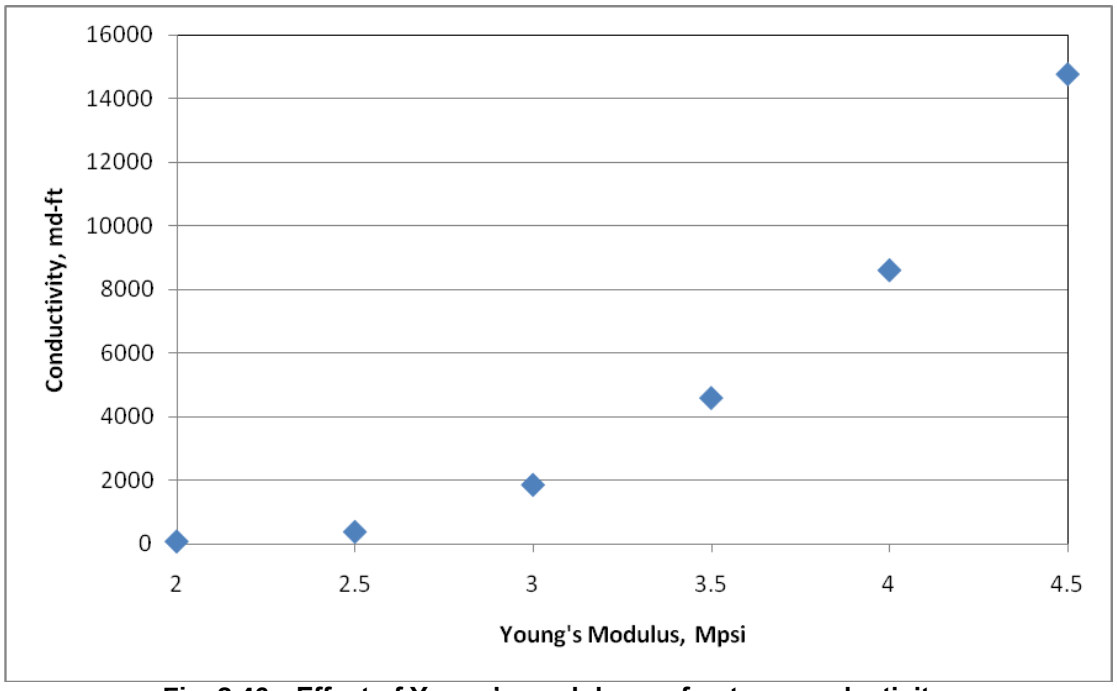

Fig. 3.46—Effect of Young's modulus on fracture conductivity.

In this chapter, I implemented the theoretical models to study the fracture closure behavior and the consequent conductivity. The relatively good agreement with the experimental results validates the numerical simulation. After the introduction of base conductivity, I investigated the model application at the intermediate scale, which is 10 by 10 feet for the calculation domain. Overall fracture conductivity at this scale is also relevant to the permeability distribution, mineralogy distribution and rock properties. The correlations will be developed based on these results.

CHAPTER IV

DEVELOPMENT OF CONDUCTIVITY CORRELATIONS

One of the main objectives in this study is to develop a new set of correlations to estimate conductivity for an acid fracture at the intermediate scale. Numerous simulations have been performed based on the methods introduced in the previous chapters. I will present the correlations for different scenarios and compare them with other correlations in this chapter. Before that, the correlations of conductivity at zero closure stress developed by Mou et al. (2010) will provide the vision of etching patterns for three categories. The correlations for overall fracture conductivity follow the same categorization and include the fracture closure behavior.

4.1 Correlations of Conductivity at Zero Closure Stress

When developing the correlations of conductivity at zero closure stress, Mou (2009) classified fracture surface etching profiles into three categories: permeability distribution dominant cases, mineralogy distribution dominant cases, and competing effect of permeability and mineralogy distributions. In this section, I will briefly introduce and list these correlations by Mou et al. (2010a, 2010b), because they serve as the beginning point of my study.

(1) Permeability distribution dominant cases.

When the leakoff coefficient is greater than about 0.004 ft/(min)$^{0.5}$, or is about 0.001 ft/(min)$^{0.5}$ with uniform mineralogy distributions (100% limestone or dolomite),

leakoff distribution that highly depends on permeability distribution dominates etching patterns. Mineralogy distribution has little effect that is negligible for the cases with a high leakoff rate.

In practice, ideal fracture width, w_i, is easy to obtain. But Mou's correlations use average fracture width, $\overline{w}$, instead. Both definitions of the width were presented when I discussed base conductivity. Therefore, the relationship between them is necessary to demonstrate first. For the high leakoff cases,

$$\overline{w} = 0.56 erf(0.8\sigma_D) w_i^{0.83}, \tag{4.1}$$

where σ_D is normalized standard deviation. The units for width are both in inch. For medium leakoff cases with uniform mineralogy distribution,

$$\overline{w} = 0.2 erf(0.78\sigma_D) w_i^{0.81}. \tag{4.2}$$

Subsequently, the correlation of conductivity at zero closure stress for permeability distribution dominant cases is,

$$\left(wk_f\right)_0 = 4.48\times10^9 \overline{w}^3 \left[1+\left(a_1 erf(a_2(\lambda_{D,x}-a_3)) - a_4 erf(a_5(\lambda_{D,z}-a_6))\right)\sqrt{(e^{\sigma_D}-1)}\right],$$

$$a_1 = 1.82 \qquad a_2 = 3.25 \qquad a_3 = 0.12 \qquad a_4 = 1.31 \qquad a_5 = 6.71 \qquad a_6 = 0.03 \tag{4.3}$$

where $(wk_f)_0$ is conductivity at zero closure stress in md-ft, and $\overline{w}$ is average width in inch.

(2) Mineralogy distribution dominant cases.

When the leakoff coefficient is less than about 0.0004 ft/(min)$^{0.5}$ under typical operation conditions, mineralogy distribution dominates etching patterns and

corresponding conductivity. In this scenario, permeability is low, and horizontal correlation length for the mineralogy distribution is high because of the laminated characteristic of sedimentary carbonate. Limestone and dolomite are the only two types of rock considered in this study. As discussed in the previous chapter, limestone percentage in rock is the key parameter that affects average width and conductivity of an acid fracture. Therefore, the relationship between ideal fracture width, w_i, and average fracture width, $\overline{w}$, is,

$$\overline{w} = 0.13(f_{\text{limestone}})^{0.56} w_i^{0.48}, \tag{4.4}$$

where $f_{\text{limestone}}$ is percentage of limestone in rock. Then, the correlation of conductivity at zero closure stress for mineralogy distribution dominant cases is,

$$\left(k_f w\right)_0 = 4.48\times 10^9 \overline{w}^3 \left[1 + 2.97\left(1 - f_{\text{limestone}}\right)^{2.02}\right]. \tag{4.5}$$

(3) Competing effect of permeability and mineralogy distributions.

If the leakoff coefficient is medium, about 0.001 ft/(min)$^{0.5}$, both permeability and mineralogy distributions have competing effects on etching patterns and corresponding conductivity. The correlation for average fracture width, $\overline{w}$, and ideal fracture width, w_i, is,

$$\overline{w} = \left(0.1(f_{\text{limestone}})^{0.43} + 0.14\sigma_D\right) w_i^{0.84}. \tag{4.6}$$

Both normalized standard deviation of permeability distribution, σ_D, and percentage of limestone, $f_{\text{limestone}}$, appear in the equation above. However, Mou (2009) suggested that conductivity changes little in terms of mineralogy no matter what kind of

permeability distribution. Thus, the correlation of conductivity he developed for this scenario excludes mineralogy distribution parameters as,

$$\left(wk_f\right)_0 = 4.48\times10^9\,\overline{w}^3\left[1+a_1+\left(a_2 erf\left(a_3(\lambda_{D,x}-a_4)\right)-a_5 erf\left(a_6(\lambda_{D,z}-a_7)\right)\right)\sqrt{(e^{\sigma_D}-1)}\right]$$

$$a_1 = 0.2 \qquad a_2 = 1.0 \qquad a_3 = 5.0 \qquad a_4 = 0.12 \qquad a_5 = 0.6 \qquad a_6 = 3.5 \qquad a_7 = 0.03 \tag{4.7}$$

Compared to the correlation for the permeability dominant cases, the format for the competing effects cases is similar, but one more constant is used.

4.2 Overall Conductivity of Acid Fracture

Based on the correlations of conductivity at zero closure stress developed by Mou et al. (2010a, 2010b), overall fracture conductivity at the intermediate scale incorporates closure stress and rock property as well. The classification remains the same as defined above: permeability distribution dominant cases, mineralogy distribution dominant cases, and competing effects of permeability and mineralogy distributions.

In the literature review, many researchers suggest their correlations in different models, such as the exponential function, the logarithm function, the power function, or multiple functions combined. In this study, the correlations of acid fracture conductivity will utilize an exponential function as the essential model that is,

$$wk_f = \alpha\exp\left(-\beta\sigma_c\right). \tag{4.8}$$

The parameter, α, contains conductivity at zero closure stress, $(wk_f)_0$, that is calculated by the correlations by Mou. The parameter, β, incorporates Young's modulus, E, and other influential factors. The most important reason to use the exponential function is because the base conductivity is calculated by the Nierode and Kruk correlation (Eq. 1.6), which is an exponential function also. But the exponential function is not necessarily the best model to fit all the data. A large amount of numerical simulations leads to the correlations of overall fracture conductivity presented as follows.

4.2.1 Permeability Distribution Dominance

When leakoff coefficient is high, the permeability distribution determines fracture surface etching patterns. The effect of mineralogy distribution can be negligible. So the parameters used in the correlation are relevant to the permeability distribution, including dimensionless horizontal and vertical correlation length, $\lambda_{D,x}$, $\lambda_{D,z}$, dimensionless standard deviation of the natural logarithm of the permeability distribution, σ_D. Obviously, conductivity at zero closure stress, $(wk_f)_0$, which is calculated by Mou's correlation, is another important input. By the linear regression in log-log plot, the correlation for permeability dominant cases is,

$$wk_f = \alpha \exp\left[-\beta\sigma_c\right], \tag{4.9a}$$

$$\alpha = \left(wk_f\right)_0\left[0.22\left(\lambda_{D,x}\sigma_D\right)^{2.8} + 0.01\left(\left(1-\lambda_{D,z}\right)\sigma_D\right)^{0.4}\right]^{0.52}, \tag{4.9b}$$

$$\beta = \left[14.9 - 3.78\ln\left(\sigma_D\right) - 6.81\ln\left(E\right)\right]\times 10^{-4}. \tag{4.9c}$$

In the equation above, σ_c is closure stress in psi, σ_D is normalized standard deviation ($0<\sigma_D<1$), and E is Young's modulus in Mpsi (million psi). The unit of Young's modulus is not compatible with the conductivity unit, but the regression for these empirical correlations is based on it. In addition, Young's modulus is required to be greater than 1 Mpsi. In general, soft rock with Young's modulus less than 2 Mpsi is not a good candidate for acid fracturing. The restrictions on σ_D and E also apply to the following correlations.

Notice that the normalized horizontal correlation length, $\lambda_{D,x}$, and the normalized vertical correlation length, $\lambda_{D,z}$, have the opposite effects on the conductivity. It is corresponding to what I presented previously. Low vertical correlation length and high horizontal correlation length favor the formation of long and narrow channels that leads to high fracture conductivity. Also, the normalized standard deviation appears in the factor, β, which accounts for the closure behavior of a fracture. Because the roughness highly depends on the standard deviation of the permeability field, high standard deviation gives greatly uneven surface that yields high conductivity.

Fig. 4.1 compares the fracture conductivity calculated by the correlation with the conductivity by the numerical models. The red solid line is $y=x$. The ideal situation is that all points fall on the line. The R^2 value indicates the proportion of variability in the data set. It provides a measure of how well the prediction is likely to be by the model. The R^2 value for Mou's correlation (2009) is higher for conductivity at zero closure stress. The correlation of overall conductivity that incorporates Mou's correlation

accumulates the inaccuracy during the regression. Thus, the R^2 value becomes lower, but still acceptable.

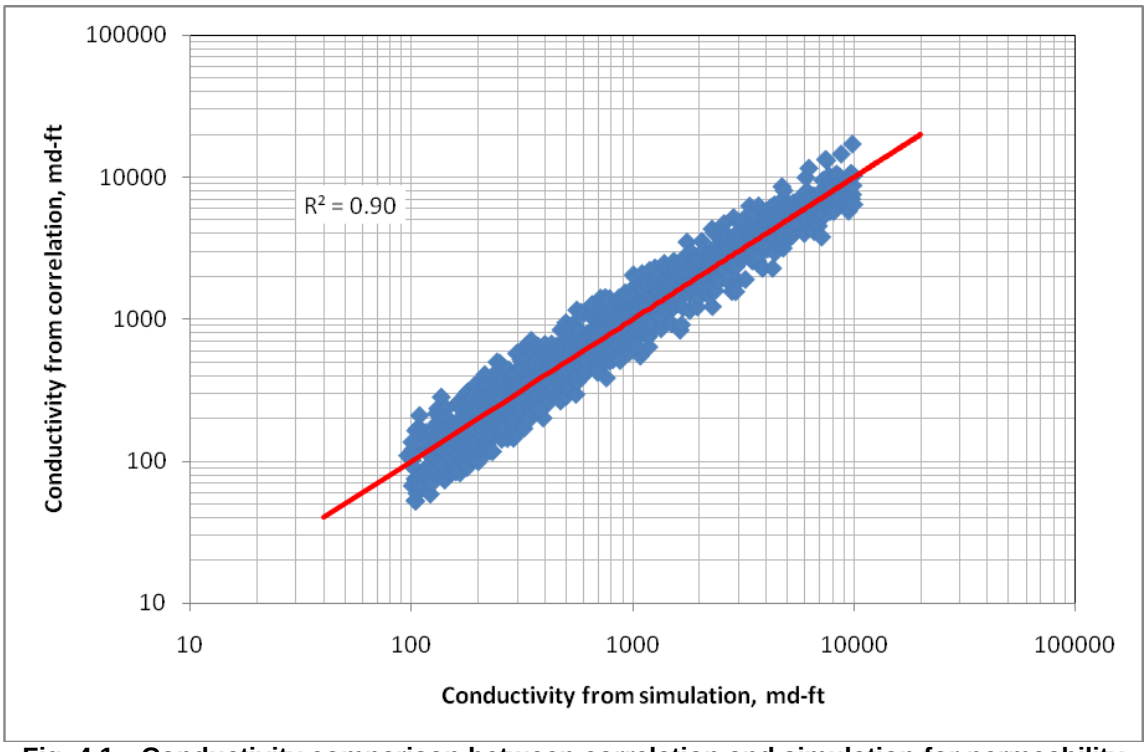

Fig. 4.1—Conductivity comparison between correlation and simulation for permeability distribution dominance.

Generally, the vertical correlation length of permeability distribution is low, because the sedimentary carbonate has the feature of lamination. When the dimensionless vertical correlation length is low enough, for example, $\lambda_{D,z}$<0.02, I ignore its effect and simplify the correlation as,

$$wk_f = \alpha \exp\left[-\beta\sigma_c\right], \tag{4.10a}$$

$$\alpha = 0.12\left(wk_f\right)_0\left(\lambda_{D,x}\sigma_D\right)^{0.1}, \tag{4.10b}$$

$$\beta = \left[15.6 - 4.5\ln\left(\sigma_D\right) - 7.8\ln\left(E\right)\right]\times 10^{-4}. \tag{4.10c}$$

This correlation is simpler and more practical. The R^2 value reaches 0.9 when the linear regression is performed in the log-log plot (Fig. 4.2).

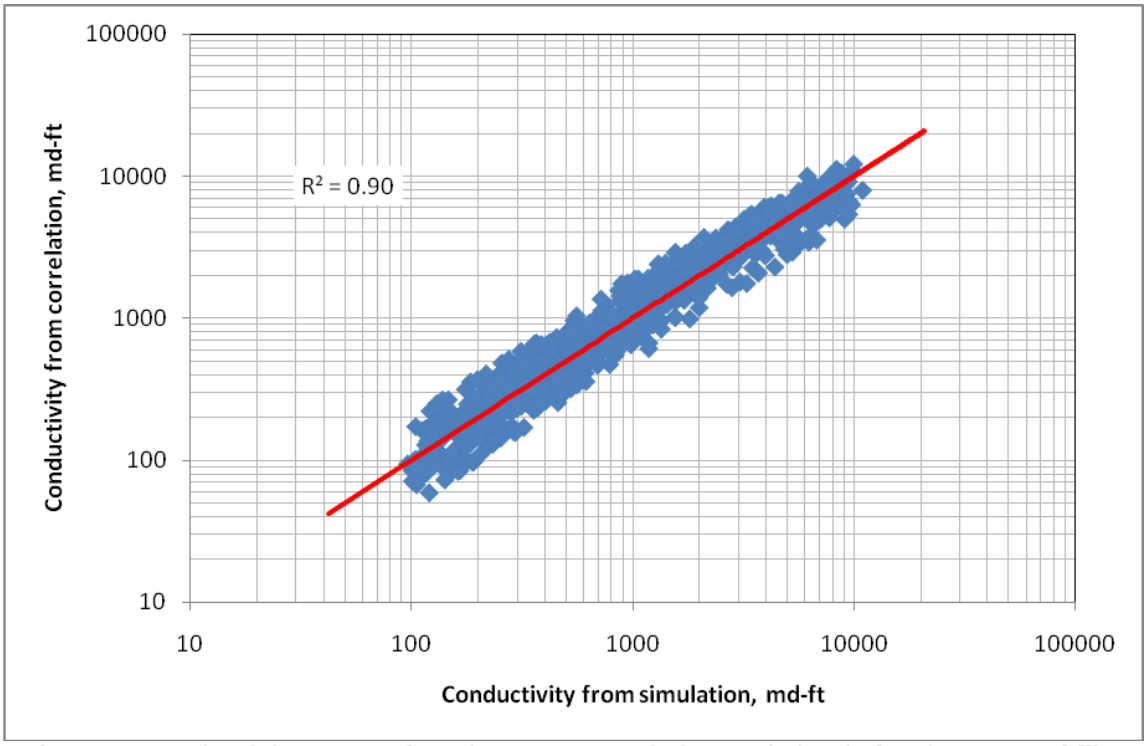

Fig. 4.2—Conductivity comparison between correlation and simulation for permeability distribution dominance without $\lambda_{D,z}$.

4.2.2 Mineralogy Distribution Dominance

For the reservoir with low permeability, leakoff is so small that its effect on surface etching patterns is insignificant. We call this scenario as mineralogy distribution dominant. In this study, limestone and dolomite are the only two types of carbonate that are considered. Mou's work shows that only limestone percentage affects the corresponding conductivity drastically. Therefore, in addition to the conductivity at zero closure stress, the correlation of overall fracture conductivity includes only three

parameters, limestone percentage, $f_{\text{limestone}}$ (dolomite percentage is equal to 1 minus limestone percentage), Young's modulus, E, and closure stress, σ_c.

$$wk_f = \alpha \exp\left[-\beta \sigma_c\right], \tag{4.11a}$$

$$\alpha = \left(wk_f\right)_0 \left(0.811 - 0.853 f_{\text{limestone}}\right), \tag{4.11b}$$

$$\beta = \left[1.2 \exp\left(0.952 f_{\text{limestone}}\right) + 10.5 E^{-1.823}\right] \times 10^{-4}. \tag{4.11c}$$

The negative signs before the limestone percentages reveal that this parameter has negative feedback on the overall conductivity. If the conductivity at zero closure stress is taken into account as well, it becomes difficult to clarify what kind of feedback from the limestone percentage. According to the previous discussion, the limestone percentage greater than 50% or less may have different impact on fracture conductivity. It needs further study.

For the comparison of simulation and correlation, **Fig. 4.3** shows the linear regression. Though the data points are fewer than permeability dominant cases, the R^2 value is higher, which means the model is better.

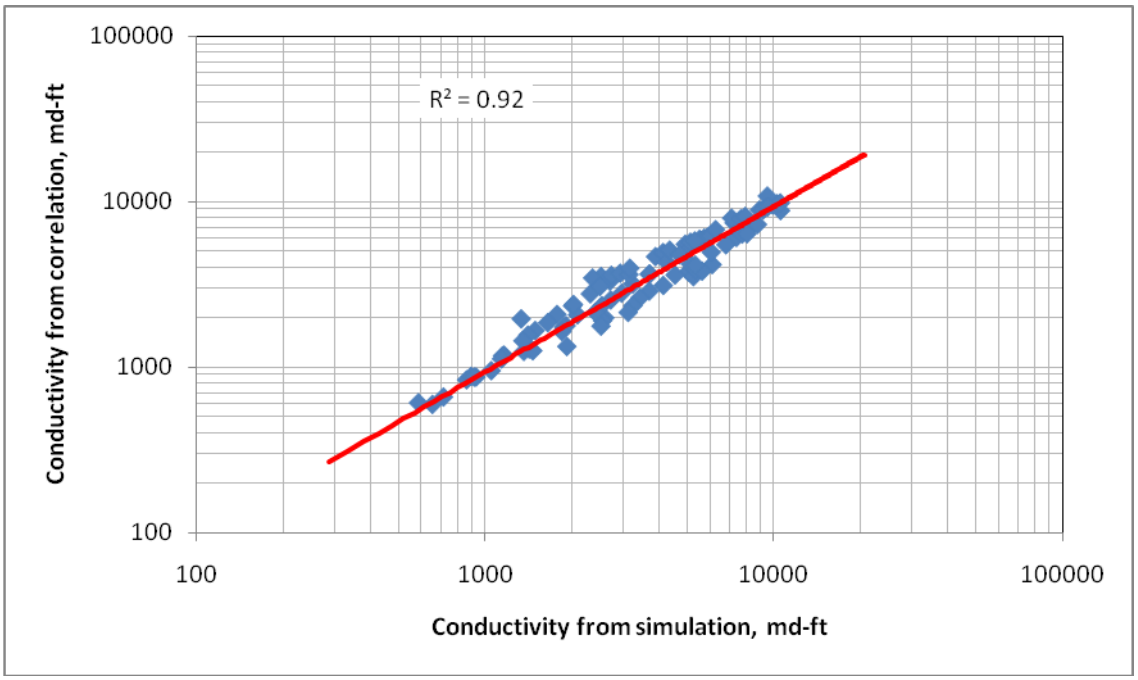

Fig. 4.3—Conductivity comparison between correlation and simulation for mineralogy distribution dominance.

4.2.3 Competing Effects of Permeability and Mineralogy Distribution

When leakoff is medium, both permeability and mineralogy distribution influence fracture etching patterns. Mou (2009) suggested that the correlation does not explicitly include the parameters of mineralogy distribution, though they do have impacts. The contribution from mineralogy distribution is channeling fracture surfaces because of high horizontal correlation length. Therefore, the following correlation includes only statistical parameters from the permeability distribution.

$$wk_f = \alpha \exp\left[-\beta\sigma_c\right], \quad (4.12a)$$

$$\alpha = \left(wk_f\right)_0\left[0.21\lambda_{D,x}{}^{0.16} + 0.046\ln\left(\sigma_D\right) + 0.15\lambda_{D,z}{}^{-0.17}\right], \quad (4.12b)$$

$$\beta = \left[53.8 - 4.58\ln\left(E\right) + 18.9\ln\left(\sigma_D\right)\right]\times 10^{-4}. \quad (4.12c)$$

The correlation is in the similar form as the one for permeability distribution dominant cases. The vertical correlation length, $\lambda_{D,z}$, still has the opposite impact with the negative power against the effect of the horizontal correlation length, $\lambda_{D,x}$. But the dimensionless standard deviation, σ_D, in the factor β has a different sign. Thus, the influence of standard deviation on fracture closure behavior is different when permeability and mineralogy distribution have competing effect.

In **Fig. 4.4**, the comparison of conductivity from correlation and numerical simulation is presented. It is not as good as the previous cases, but the R^2 value is still acceptable.

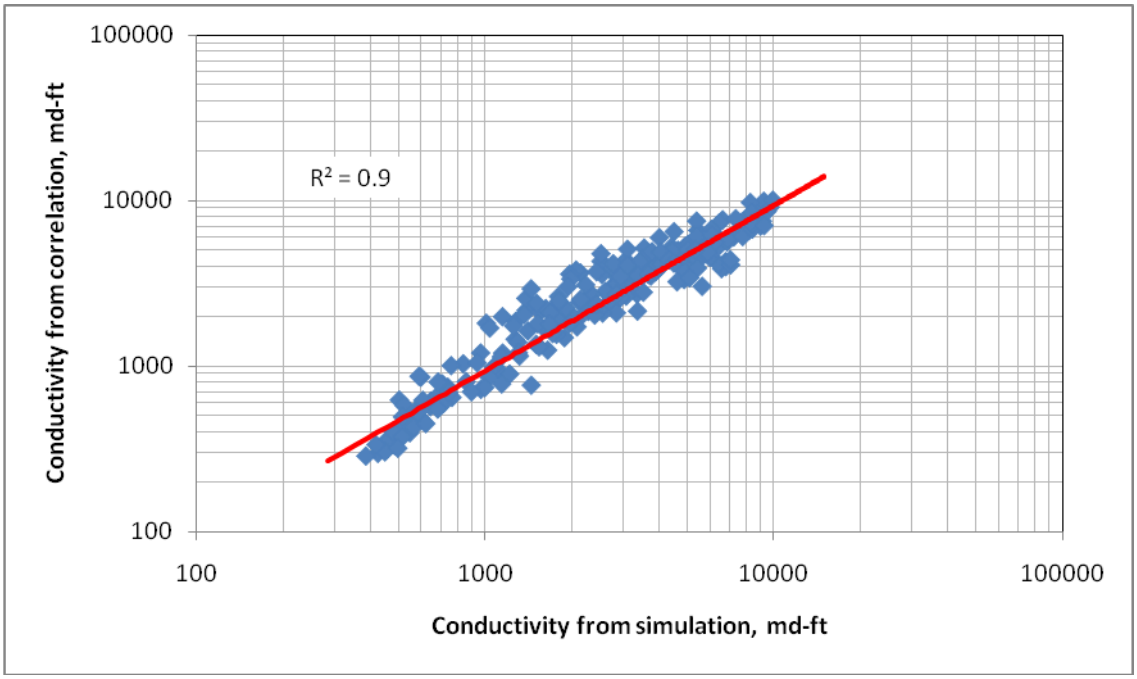

Fig. 4.4—Conductivity comparison between correlation and simulation for competing effects.

4.3 Discussion

To evaluate the new correlations more, I will discuss and compare them in this section. Among the three scenarios, the permeability distribution dominant one is a common and typical case. Thus, the following discussion is based on this situation with a high leakoff coefficient. In addition, suppose the vertical correlation length is small enough to neglect. Therefore, Eqs. 4.1, 4.3, and 4.10 will provide the calculation results that will be compared to other models.

Essentially, the correlation of overall fracture conductivity is an exponential function with factors α and β that are functions of statistical parameters and rock properties. If drawn in a semi log plot, the curve is a straight line. The α determines the intercept, and the β determines the slope. So I will discuss the α, β, and relationship between overall conductivity and closure stress, respectively.

In the new correlations, the intercept, α, is a strong function of horizontal correlation length and standard deviation as vertical correlation length is assumed small. The semi log plot (**Fig. 4.5**) shows the relationship among them. In this case, the ideal fracture width, w_i, is 0.2 inches. The dimensionless horizontal correlation length ranges from 0.1 to 1, and dimensionless standard deviation ranges from 0.1 to 0.7. The results by the Nierode and Kruk model are also presented for the purpose of comparison.

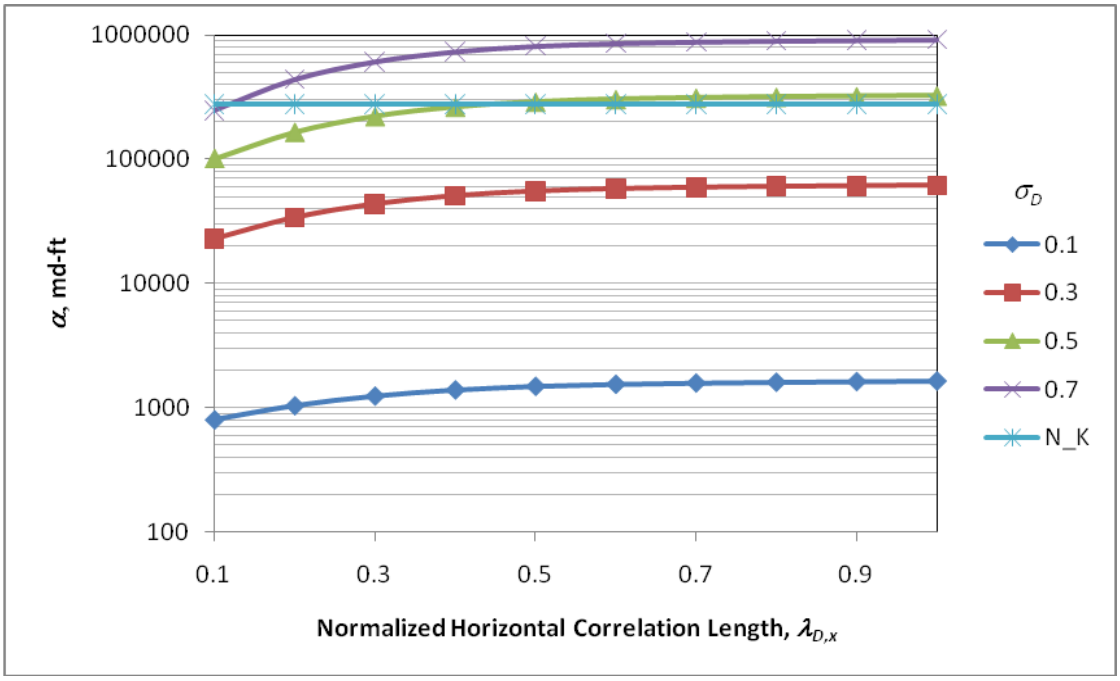

Fig. 4.5—Intercept α for different horizontal correlation lengths and standard deviations.

The intercept, α, increases as the horizontal correlation length approaches 1. After the horizontal correlation length is greater than 0.7, the increment is not dramatic. But α drops fast if the correlation length is less than 0.3. The high standard deviation also results in the high α, especially on the logarithm scale of the axis y. The α in the correlation developed by Nierode and Kruk doesn't account for the effect of permeability or mineralogy distribution. Thus, it is only one straight line in the plot. The observation indicates that the data points by the new correlation are basically below the straight line of the Nierode and Kruk model. **Fig. 4.6** explains why the new correlation underestimates the intercept of the conductivity curve.

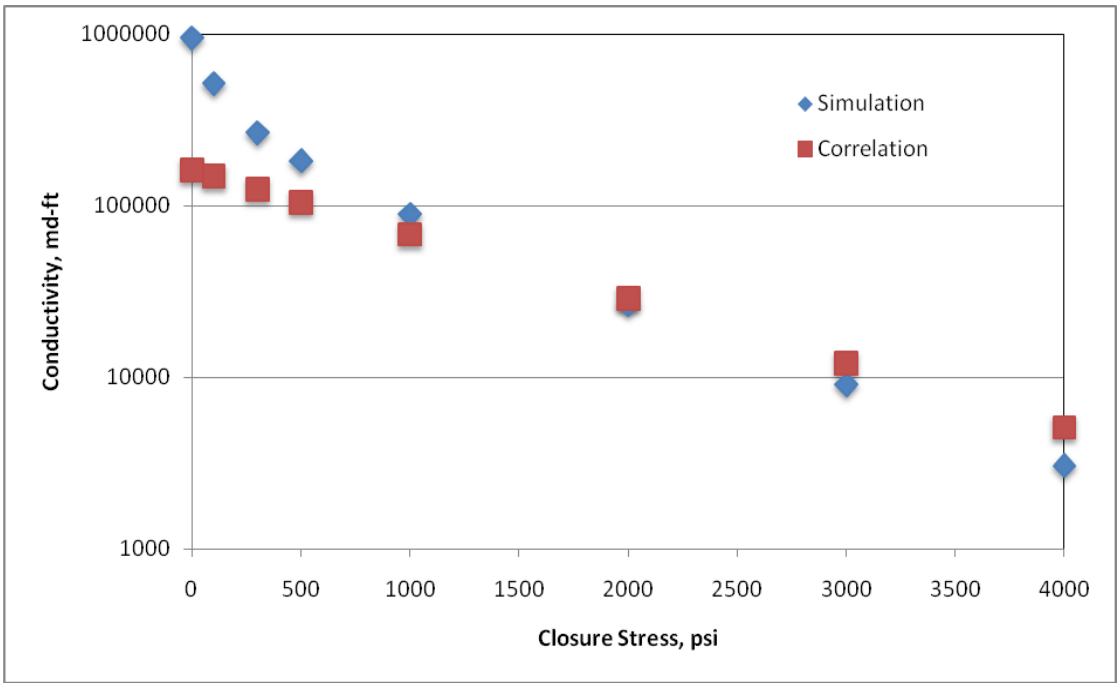

Fig. 4.6—Comparison of conductivity curves between simulation and correlation.

The example has a high horizontal correlation length and a medium standard deviation. Both results from simulation (blue diamonds) and correlation (red squares) are presented in the semi log plot. For the simulation, the conductivity drops quickly when the closure stress is low. After that, the curve tends to be a straight line. The correlation approaches this curve by employing an exponential function, which is a straight line in the semi log plot. Therefore, a compromise occurs at the low closure stress, because the closure stress higher than 1,000 psi is more common and important. I tried to match the conductivity at high closure stress better. The conductivity at low closure stress that determines the intercept is inevitably underestimated by the new correlation. However, the Mou's model is still able to conduct a good prediction of conductivity at zero closure stress.

The factor, β, in the new correlation is relevant to the closure behavior of an acid fracture. The deformation is intensive if a steep slope, β, is obtained. According to Eq. 4.10, β is a function of Young's modulus and normalized standard deviation. I plotted the relationship among them in **Fig. 4.7**. High standard deviation and high Young's modulus yield small β, which indicates that the fracture is difficult to close. The slope for the Nierode and Kruk's correlation is a function of only rock strength. The curve basically locates between the curves with σ_D 0.5 and 0.7. With respect to the rock strength, it decreases more slowly than other curves based on the new correlation. At the intermediate scale, closure behavior of channels plays an important role as well as roughness. But experiments in a lab mainly capture the feature of roughness caused by rock's heterogeneity. That is the reason why they have different slopes in Fig. 4.7.

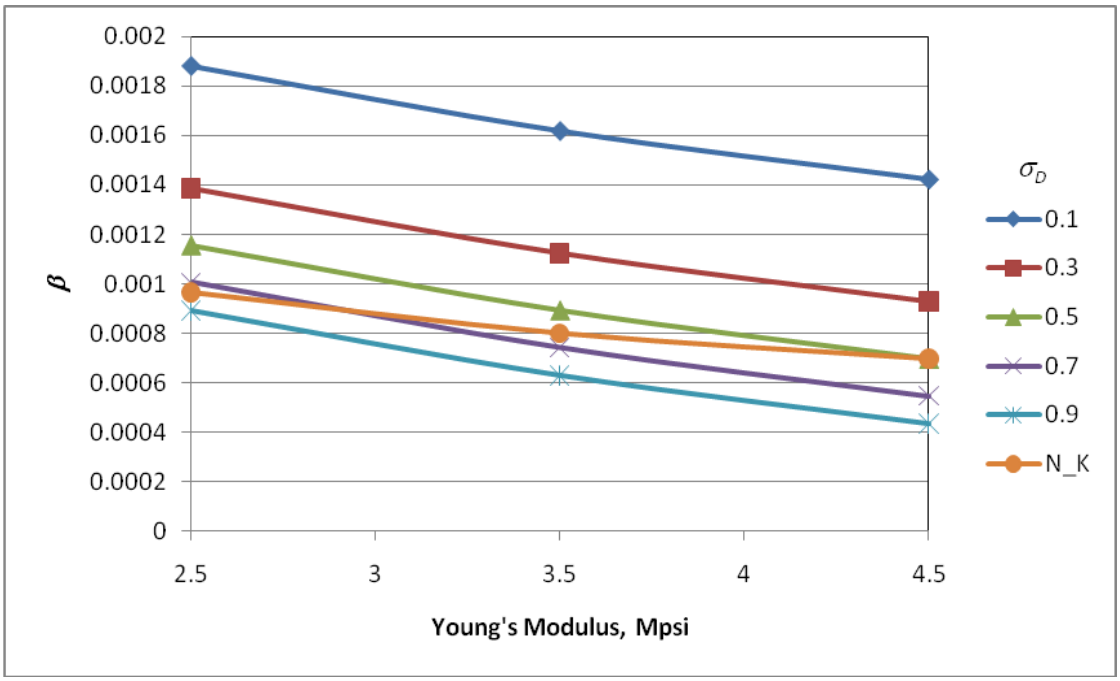

Fig. 4.7—Intercept β for different Young's moduli and standard deviations.

After investigation of α and β in the new correlation, I calculate the conductivity under different closure stresses in terms of dimensionless horizontal correlation length (**Fig. 4.8**), dimensionless standard deviation (**Fig. 4.9**), and Young's modulus (**Fig. 4.10**), respectively. Essentially, all curves in these semi log plots are monotone decreasing straight lines for the reason that the new correlation is built by the exponential function.

In Fig. 4.8, the straight lines are parallel to each other, because the dimensionless horizontal correlation length has little impact that is neglected on the slope. In addition, the curves with $\lambda_{D,x}$ 0.5 or higher are close to each other. It reveals that conductivity decrease dramatically if normalized horizontal correlation length is lower than 0.5.

In Fig. 4.9, the dimensionless standard deviation that represents the permeability heterogeneity affects both the conductivity at zero closure stress and the closure behavior. The intercepts and the slopes are obviously different. The line with σ_D=0.1 is far from the others because the etching pattern is too uniform to produce good conductivity for this case.

In Fig. 4.10, all straight lines start from the same conductivity at zero closure stress. The strong rock with a high Young's modulus is difficult to close, so the slope of the straight line is smaller than the soft rock with a low one.

Fig. 4.8—Conductivity curves with respect to normalized horizontal correlation length.

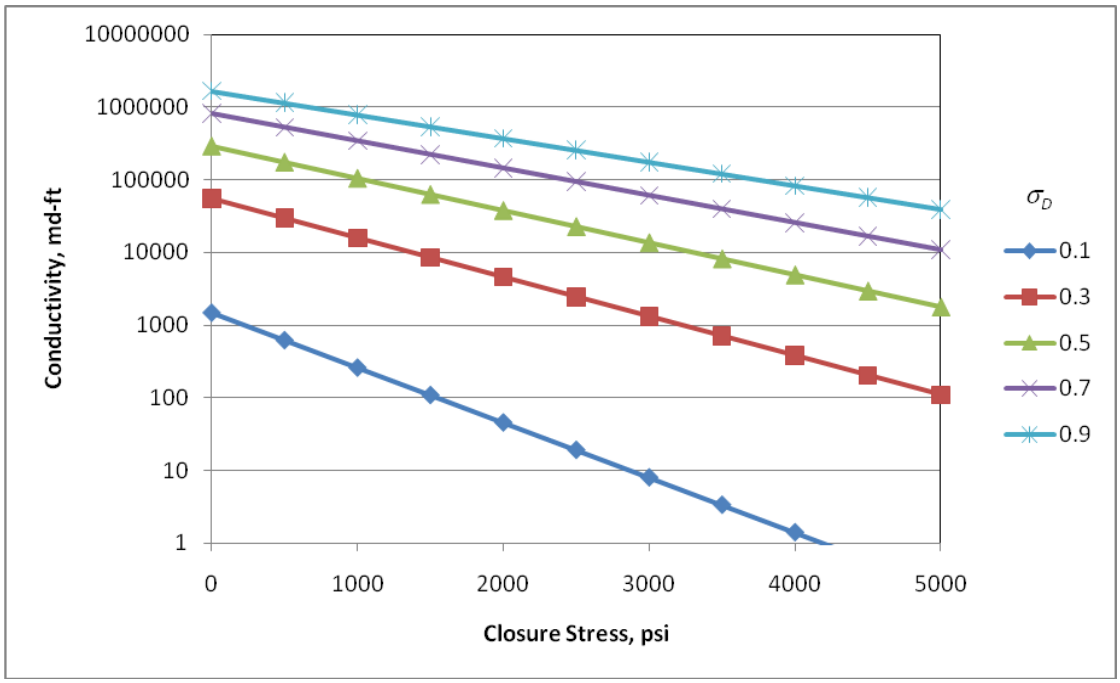

Fig. 4.9—Conductivity curves with respect to normalized standard deviation.

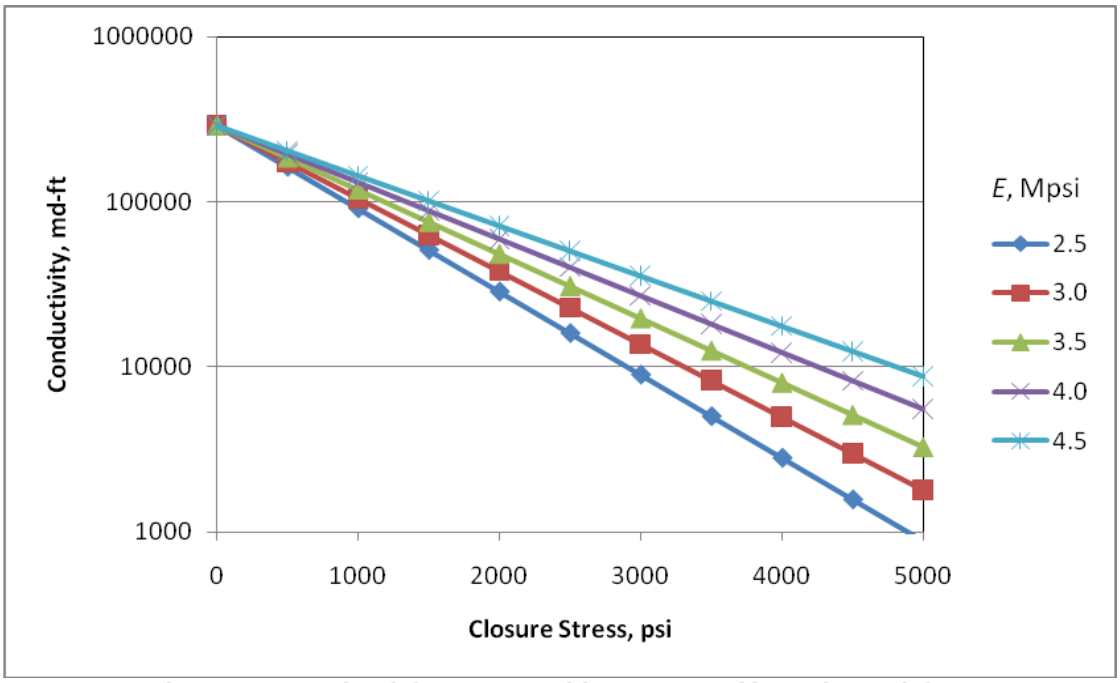

Fig. 4.10—Conductivity curves with respect to Young's modulus.

CHAPTER V

CONCLUSIONS AND RECOMMENDATIONS

5.1 Conclusions

The intermediate scale simulation of acid fracturing captures the heterogeneous feature such as channels that the experiments fail to see. It can close the gap between the macro scale simulator and the micro scale experiments. Beginning with fracture width profiles by acid dissolution and conductivity at zero closure stress, I have modeled the deformation of the fracture surfaces as closure stress increases. At any cross-section along the fracture, I approximate the fracture shape as being a series of elliptical openings. The analytical solutions act as the criteria to determine how many ellipses remain open. By assigning base conductivity to closed regions, the overall fracture conductivity is obtained as a result of numerically applying the local cubic law to model the flow through the heterogeneous system. Based on the comparisons and discussions above, this study reveals the following important conclusions:

1. The application of the analytical solutions on the experimental cases yields the reasonable conductivity that has a good agreement with the measurements in the lab. It validates the approach that is capable of giving acceptable estimates of fracture conductivity.
2. Because the grids of the intermediate scale domain are not fine enough to capture roughness information, the calculation need to incorporate the empirical correlations such as the Nierode and Kruk correlation, which give

base conductivities. The correlations based at the experimental scale mainly account for the effect of roughness, while the numerical simulations at the intermediate scale fractures capture more features of channel deformation.

3. The permeability distribution of the formation affects the closure behavior of an acid fracture. Low vertical correlation length and high horizontal correlation length lead to narrow and long channels that are difficult to be closed and favorable to overall conductivity. High standard deviation results in uneven etchings that also contribute significantly to the fracture conductivity.
4. Limestone and dolomite are the only two types of rock in this study. The percentage of each is the main aspect that affects fracture conductivity. Higher limestone percentage leads to more channels that result in higher overall conductivity.
5. Young's modulus representing the rock strength plays an important role in fracture closure. Strong rock with high Young's modulus is able to resist the closure stress effectively and allow much space for fluid flow. On the contrary, another rock property, Poisson's ratio, has negligible effect on conductivity calculation.
6. The relationship between conductivity and closure stress is not exactly the exponential function according to the simulation results in this study. The deformation of channels results in quick conductivity reduction under low

closure stresses. As the closure stress is increasing, the trend of overall conductivity curve is getting close to the trend of base conductivity curve.

7. I conducted the extensive numerical experiments and developed the new correlations for overall conductivity of acid fracture. They apply for three categories respectively: permeability distribution dominance, mineralogy distribution dominance, and competing effect of permeability and mineralogy distributions. The exponential function is fundamental for the correlations that incorporate conductivity at zero closure stress, statistical parameters of permeability and mineralogy distributions, Young's modulus, and closure stress.

5.2 Recommendations

During this research, some problems still necessitate further study. I investigated the major effects on overall conductivity of acid fracture, but several aspects that I neglected may require more consideration. In addition, a few recommendations will be list as follows:

1. The relationship (Eq. 3.9) between Young's modulus, E, and rock embedment strength, S_{RE}, is based on the data set measured in our laboratory and a service company. The core samples are not adequate or universal to fully determine the general relationship. In practice, a better way is to measure both E and S_{RE} in the lab and apply into the model.

2. Nasr-El-Din et al. (2008) pointed out that carbonate rock can be softened depending on acid system choice. The parameters of rock strength used in the closure model should be measured after acid treatment. But the measurements of rock embedment strength conducted by Pournik (2008) did not show any obvious softening effects. Thus, we need to be cautious when coping with the rock strength for the model.
3. For mineralogy distribution dominant cases, we considered only limestone percentage, but neglected the effects of statistical parameters of mineralogy distribution according to the Mou's model. Actually, the vertical correlation length of the mineralogy distribution may not be low enough to ignore. The high vertical correlation length can yield wide channels that result in low conductivity because wide channels tend to be closed easily.
4. Another concern for mineralogy distribution dominant cases is about the effect of limestone percentage. Mou (2009) showed that conductivity at zero closure stress increases with limestone percentage. I confirmed that overall conductivity has the same trend when the limestone percentage is less than 50% (Fig. 3.40). If the limestone percentage reaches 100%, the corresponding conductivity should be very low because of the even etching. Thus, study on cases with limestone percentage higher than 50% is one of recommendations.

5. The model considered rock consisting of just limestone and dolomite that are the main components of carbonate. A better model should include effects of other types of rocks present in real formations, such as anhydride.
6. The new correlations are easy to apply in practice. But they have some assumptions in the input that are not suitable for certain acid fracturing cases. If the programs that are summarized in Appendix C can be organized and combined as a package, users may be able to input the particular parameters and calculate the resulting conductivity for a specific case. The models will be more helpful for acid fracturing design.
7. I implemented the analytical solutions for ellipses in the closure model. They are 2D models, so the deformation of every cross-section is calculated separately. The closure of the whole fracture, then, consists of the results from every single cross-section. But the ideal simulation is fully three dimensional. I tried several simple ellipse cases in Appendix D. However, many difficulties still exist for the fully 3D numerical simulation on rough surfaces. Furthermore, the solution to fracture closure behavior ought to be an explicit function of time. Even after the transient closure, closure stress has long-term effects on the deformation of fracture surfaces. This unsteady phenomenon needs further study.
8. Bale et al. (2010) propose a revolutionary approach for carbonate stimulation that combines acid fracturing with proppant (CAPF). The model presented in

this study may be applicable to this new idea. That would be an interesting topic to explore in the future.

REFERENCES

Anderson, M.S., and Fredrickson, S.E. 1989. Dynamic Etching Tests Aid Fracture-Acidizing Treatment Design. *SPE Production Engineering* **4**(4): 443-449. SPE-16452.

Antelo, L.F., Pournik, M., Zhu, D., and Hill, A.D. 2010. Surface Etching Pattern and its Effect on Fracturing Conductivity in Acid Fracturing. Paper SPE-119743 presented at the 2009 SPE Hydraulic Fracturing Technology Conference, The Woodlands, Texas, USA, 19-21 January 2009.

Bale, A., Smith, M.B., and Klein, H.H. 2010. Stimulation of Carbonates Combining Acid Fracturing with Proppant (CAPF): A Revolutionary Approach for Enhancement of Sustained Fracture Conductivity and Effective Fracture Half-length. Paper SPE-134307 presented at the SPE Annual Technical Coference and Exihibition, Florence, Italy, 19-22 September 2010.

Beatty, C.V. 2010. Characterization of Small Scale Heterogeneity for Prediction of Acid Fracture Performance. MS thesis. Texas A&M University, College Station.

Beg, M.S., Kunak, A.O., Gong, M., Zhu, D., and Hill, A.D. 1998. A Systematic Experimental Study of Acid Fracture Conductivity. *SPEPF* **13**(4): 267-271. SPE-52402.

Blatt, H., Middleton, G., and Murray, R. 1980. *Origin of Sedimentary Rocks*. Englewood Cliffs, New Jersey: Prentice-Hall.

Brown, S.R., and Scholz, C.H. 1985. Closure of Random Elastic Surfaces in Contact. *J. of Geophysical Research* **90**(B7): 5531-5545.

Brush, D.J., and Thomson, N.R. 2003. Fluid Flow in Synthetic Rough-Walled Fractures: Navier-Stokes, Stokes, and Local Cubic Law Simulations. *Water Resources Research* **39**(4): 1085-1099.

Cook, N.G.W. 1992. Natural Joints in Rock: Mechanical, Hydraulic and Seismic Behaviour and Properties under Normal Stress. *International J. of Rock Mechanics, Mining Sciences, and Geomechanics Abstract* **29**(3): 198-223.

Coulter, A.W., Alderman, E.N., Cloud, J.E., and Crowe, C.W. 1974. Mathematical Model Simulates Actual Well Conditions in Fracture Acidizing Treatment Design. Paper SPE-5004 presented at the SPE_AIME 49th Annual Fall Meeting, Houston, Texas, USA, 6-9 October 1974.

Fjaer, E., Holt, R.M., Horsrud, P., Raaen, A.M., and Risnes, R. 2008. *Petroleum Related Rock Mechanics*. Amsterdam and London: Elsevier.

Gangi, A.F. 1978. Variation of Whole and Fractured Porous Rock Permeability with Confining Pressure. *International J. of Rock Mechanics, Mining Sciences, and Geomechanics Abstract* **15**(5): 249-257.

Gercek, H. 2007. Poisson's Ratio Values for Rocks. *International J of Rock Mechanics and Mining Sciences* **44**: 1-13.

Gomaa, A.M., and Nasr-El-Din, H.A. 2009. Acid Fracturing: the Effect of Formation Strength on Fracture Conductivity. Paper SPE-119623 presented at the 2009 SPE Hydraulic Fracturing Technology Conference, The Woodlands, Texas, USA, 19-21 January 2009.

Gong, M. 1997. Mechanical and Hydraulic Behavior of Acid Fractures - Experimental Studies and Mathematical Modeling. PhD dissertation. University of Texas at Austin, Austin, Texas, USA.

Gong, M., Lacote, S., and Hill, A.D. 1999. New Model of Acid-Fracture Conductivity Based on Deformation of Surface Asperities. *SPEJ* **4**(3): 206-214. SPE-57017.

Greenwood, J.A., and Williamson, J. 1966. Contact of Nominally Flat Surfaces. *Proc*., the Royal Society of London, Series A, Mathematical and Physical Sciences. London. **295:** 300-319.

Hakami, E., and Larsson, E. 1996. Aperture Measurements and Flow Experiments on a Single Natural Fracture. *International J of Rock Mechanics and Mining Sciences* **33**(4): 395-404.

Hardy, H.H., and Beier, R.A. 1994. *Fractals in Reservoir Engineering*. River Edge, New Jersey: World Scientific Publishing Co. Pte. Ltd.

Hopkins, D.L. 1990. The Effect of Surface Roughness on Joint Stiffness, Aperture, and Acoustic Wave Propagation. PhD dissertation. University of California at Berkeley, Berkeley, California, USA.

Isaaks, E.H., and Srivastava, R.M. 1989. *An Introduction to Applied Geostatistics*. New York: Oxford University Press, Inc.

Jaeger, J.C., Cook, N.G.W., and Zimmerman, R.W. 2007. *Fundamentals of Rock Mechanics*. Malden, Massachusetts: Blackwell Pub.

Kalfayan, L.J. 2007. Fracture Acidizing: History, Present State, and Future. Paper SPE-106371 presented at the 2007 SPE Hydraulic Fracturing Technology Conference, College Station, Texas, USA, 29-31 January 2007.

Konzuk, J.S., and Kueper, B.H. 2004. Evaluation of Cubic Law Based Models Describing Single-Phase Flow Through a Rough-Walled Fracture. *Water Resources Research* **40**(2): 39-55.

Lee, S.D., and Harrison, J.P. 2001. Empirical Parameters for Non-Linear Fracture Stiffness From Numerical Experiments of Fracture Closure. *International J. of Rock Mechanics and Mining Sciences* **38**(5): 721-727.

Malagon, C., Pournik, M., and Hill, A.D. 2008. The Texture of Acidized Fracture Surfaces--Implications for Acid Fracture Conductivity. *SPE Production & Operations* **23**(3): 343-352. SPE-102167.

Malama, B., and Kulatilake, P.H.S.W. 2003. Models for Normal Fracture Deformation Under Compressive Loading. *International J. of Rock Mechanics and Mining Sciences* **40**: 893-901.

Maugis, D. 1992. Stresses and Displacements around Cracks and Elliptical Cavities: Exact Solutions. *Engineering Fracture Mechanics* **43**(2): 217-255.

Melendez, M.G., Pournik, M., Zhu, D., and Hill, A.D. 2007. The Effects of Acid Contact Time and the Resulting Weakening of the Rock Surfaces on Acid-Fracture Conductivity.

Paper SPE-107772 presented at the 2007 SPE European Formation Damage Meeting, Scheveningen, Netherlands, 30-1 May-June 2007.

Mou, J. 2009. Modeling Acid Transport and Non-Uniform Etching in a Stochastic Domain in Acid Fracturing. PhD dissertation. Texas A&M University, College Station.

Mou, J., Hill, A.D., and Zhu, D. 2007. The Velocity Field and Pressure-Drop Behavior in a Rough-Walled Fracture. Paper SPE-105182 presented at the 2007 SPE Hydraulic Fracturing Technology Conference, College Station, Texas, USA, 29-31 January 2007.

Mou, J., Zhu, D., and Hill, A.D. 2009. Acid-Etched Channels in Heterogeneous Carbonates--a Newly Discovered Mechanism for Creating Acid Fracture Conductivity. Paper SPE-119619 presented at the 2009 SPE Hydraulic Fracturing Technology Conference, The Woodlands, Texas, USA, 19-21 January 2009.

Mou, J., Zhu, D., and Hill, A.D. 2010a. A New Acid-Fracture Conductivity Model Based on the Spatial Distributions of Formation Properties. Paper SPE-127935 presented at the 2010 SPE International Symposium and Exhibition on Formation Damage Control, Lafayette, Louisiana, USA, 10-12 February 2010.

Mou, J., Zhu, D., and Hill, A.D. 2010b. New Correlations of Acid Fracture Conductivity at Low Closure Stress Based on the Spatial Distributions of Formation Properties. Paper

SPE-131591 presented at the CPS/SPE International Oil & Gas Conference and Exhibition, Beijing, China, 8-10 June 2010.

Myer, L.R. 2000. Fractures as Collections of Cracks. *International J. of Rock Mechanics and Mining Sciences* **37**: 231-243.

Nasr-El-Din, H.A., Al-Driweesh, S.M., Metcalf, A.S., and Chesson, J.B. 2008. Fracture Acidizing: What Role Does Formation Softening Play in Production Response? *SPE Production & Operations* **23**(2): 184-191. SPE-103344.

Nierode, D.E., and Kruk, K.F. 1973. An Evaluation of Acid Fluid Loss Additives, Retarded Acids, and Acidized Fracture Conductivity. Paper SPE-4549 presented at the 48th Annual Fall Meeting of Society of Petroleum Engineering of AIME, Las Vegas, Nevada, USA, 1973.

Nierode, D.E., Williams, B.B., and Bombardieri, C.C. 1972. Prediction of Stimulation from Acid Fracture Treatments. *J. Cnd. Pet. Tech*: 31-41.

Pournik, M. 2008. Laboratory-Scale Fracture Conductivity Created by Acid Etching. PhD dissertation. Texas A&M University, College Station, Texas, USA.

Pournik, M., Zou, C., Malagon, C. et al. 2007. Small-Scale Fracture Conductivity Created by Modern Acid-Fracture Fluids. Paper SPE-106272 presented at the 2007 SPE Hydraulic Fracturing Technology Conference, College Station, Texas, USA, 29-31 January 2007.

Roberts, L.D., and Guin, J.A. 1975. The Effects of Surface Kinetics in Fracture Acidizing. *SPEJ* **8**: 385-395. SPE-4349.

Royle, A., Clark, I., Brooker, P.I. et al. 1980. *Geostatistics*. New York: McGraw-Hill: 20-21.

Ruffet, C.S., Fery, J.J., and Onaisi, A. 1997. Acid-Fracturing Treatment: A Surface-Topography Analysis of Acid-Etched Fractures to Determine Residual Conductivity. Paper SPE-38175 presented at the SPE European Formation Damage Conference, The Hague, The Netherlands, 2-3 June 1997.

Skjetne, E., Hansen, A., and Gudmundsson, J.S. 1999. High-Velocity Flow in a Rough Fracture. *J. of Fluid Mechanics* **383**: 1-28.

Swan, G. 1983. Determination of Stiffness and Other Joint Properties From Roughness Measurements. *Rock Mechanics and Rock Engineering* **16**(1): 19-38.

Tsang, Y.W., and Witherspoon, P.A. 1981. Hydromechanical Behavior of a Deformable Rock Fracture Subject to Normal Stress. *J of Geophysical Research* **86**(B10): 9287-9298.

Van Domelen, M.S. 1992. Optimizing Fracture Acidizing Treatment Design by Integrating Core Testing, Field Testing, and Computer Simulation. Paper SPE-22393 presented at the SPE International Meeting on Petroleum Engineering, Beijing, China, 24-27 March 1992.

van Domselaar, H.R., Schols, R.S., and Visser, W. 1973. An Analysis of the Acidizing Process in Acid Fracturing. *SPEJ* **8**: 239-250. SPE-3748.

Walsh, J.B. 1965. The Effect of Cracks on the Uniaxial Elastic Compression of Rocks. *J of Geophysical Research* **70**(2): 399-411.

Walsh, J.B. 1981. Effect of Pore Pressure and Confining Pressure on Fracture Permeability. *International J. of Rock Mechanics, Mining Sciences, and Geomechanics Abstract* **18**(5): 429-435.

Williams, B.B., Gidley, J.L., and Schechter, R.S. 1979. *Acidizing Fundamentals*. New York: SPE of AIME: 55.

Williams, B.B., and Nierode, D.E. 1972. Design of Acid Fracturing Treatments. *JPT* **24**(7): 849-859. SPE-3720.

Yeo, I.W., DeFreitas, M.H., and Zimmerman, R.W. 1998. Effect of Shear Displacement on the Aperture and Permeability or a Rock Fracture. *International J. of Rock Mechanics, Mining Sciences, and Geomechanics Abstract* **35**(8): 1051-1070.

Zimmerman, R.W., and Bodvarsson, G.S. 1996. Hydraulic Conductivity of Rock Fractures. *Transport in Porous Media* **23**(1): 1-30.

Zou, C. 2005. Development and Testing of an Advanced Acid Fracture Conductivity Apparatus. M.S. Thesis. Texas A&M University, College Station.

Supplemental Sources Consulted

Airy, G.B. 1863. On the Strains in the Interior of Beams. *Philosophical Trans. Royal Society of London* **153**: 49-79.

Griffith, A.A. 1921. The Phenomena of Rupture and Flow in Solids. *Philosophical Trans. Royal Society of London. Series A* **221**: 163-198.

Irwin, G.R., and Kies, J.A. 1952. Fracturing and Fracture Dynamics. *Welding J* **31**(2): 95-100.

Kolosov, G.V. 1909. O the Application of the Theory of Functions of a Complex Variable to a Plane Problem in the Mathematical Theory of Elasticity. PhD dissertation. Dorpat University, Russia.

Muskhelishvili, N.I. 1963. *Some Basic Problems of the Mathematical Theory of Elasticity: Fundamental Equations, Plane Theory of Elasticity, Torsion, and Bending*. Groningen: P. Noordhoff.

Tada, H., Paris, P.C., and Irwin, G.R. 2000. *The Stress Analysis of Cracks Handbook*. New York: ASME Press: 1.7, 7.1, Appendix B.

APPENDIX A

AIRY STRESS FUNCTION AND COMPLEX VARIABLE METHOD

Airy stress function is a stress-based method for solving 2D elastic problem simply. It reduces the governing equations to a single partial differential equation. By developing complex variable method, Kolosov (1909) and Muskhelishvili (1963) expressed Airy stress function in term of two analytical functions of a complex variable, and solved for the displacements and stresses. I introduce the methods in this appendix.

A.1 Airy stress function

The derivation starts with the strain compatibility equation,

$$2\frac{\partial^2 \varepsilon_{xy}}{\partial x \partial y} = \frac{\partial^2 \varepsilon_{xx}}{\partial y^2} + \frac{\partial^2 \varepsilon_{yy}}{\partial x^2}, \tag{A.1}$$

where ε_{xy}, ε_{xx}, and ε_{yy} are strain components. Substitution of 2D stress-strain relations into Eq. A.1 yields,

$$(\kappa+1)\left[\frac{\partial^2 \tau_{xx}}{\partial y^2} + \frac{\partial^2 \tau_{yy}}{\partial x^2}\right] + (\kappa-3)\left[\frac{\partial^2 \tau_{xx}}{\partial x^2} + \frac{\partial^2 \tau_{yy}}{\partial y^2}\right] = 8\frac{\partial^2 \tau_{xy}}{\partial x \partial y}, \tag{A.2}$$

where κ is Muskhelishvili's coefficient, τ_{xy}, τ_{xx}, and τ_{yy} are stress components.

Two equilibrium equations are,

$$\frac{\partial \tau_{xx}}{\partial x} + \frac{\tau_{yx}}{\partial y} + \rho F_x = 0, \tag{A.3a}$$

$$\frac{\partial \tau_{xy}}{\partial x} + \frac{\tau_{yy}}{\partial y} + \rho F_y = 0\,, \tag{A.3b}$$

where ρ is the density, F_x and F_y are body forces in each direction. Differentiation of two equilibrium equations yields,

$$-8\frac{\partial^2 \tau_{xy}}{\partial x \partial y} = 4\left[\frac{\partial^2 \tau_{xx}}{\partial x^2} + \frac{\partial^2 \tau_{yy}}{\partial y^2}\right] + 4\rho\left[\frac{\partial F_x}{\partial x} + \frac{\partial F_y}{\partial y}\right]. \tag{A.4}$$

Substitution of Eq. A.4 into Eq. A.2 yields,

$$\left(\frac{\partial^2}{\partial y^2} + \frac{\partial^2}{\partial x^2}\right)\left[\tau_{xx} + \tau_{yy}\right] = -\frac{4\rho}{\kappa + 1}\left(\frac{\partial F_x}{\partial x} + \frac{\partial F_y}{\partial y}\right). \tag{A.5}$$

Assuming no body forces, the stress equilibrium equations will automatically be satisfied if we define the three independent stress components in terms of some function, U, as follows,

$$\tau_{xx} = \frac{\partial^2 U}{\partial y^2},\ \tau_{yy} = \frac{\partial^2 U}{\partial x^2},\ \tau_{xy} = -\frac{\partial^2 U}{\partial x \partial y}. \tag{A.6}$$

Substitution of Eq. A.6 into Eq. A.5 yields the biharmonic equation,

$$\nabla^4 U = 0\,. \tag{A.7}$$

The biharmonic function, U, is known as an Airy stress function, after Airy, G. B. (1863), the British astronomer who first suggested this approach.

A. 2 Complex variable method

The complex variable method represents the displacement and stresses in terms of two analytic functions of a complex variable. In this project, I introduce the main results of displacements which are more important than the stresses.

The expression of Airy stress function, U, in terms of two analytic functions, $\phi(z)$ and $\chi(z)$, are,

$$U = \frac{1}{2}\left\{\bar{z}\phi(z) + z\overline{\phi(z)} + \chi(z) + \overline{\chi(z)}\right\}, \tag{A.8}$$

where $z = x + iy$, $\bar{z} = x - iy$

Making use of stress-strain relationship and the definition of strain (Jaeger et al., 2007), the displacement vector with respect to a complex number is,

$$2G(u + iv) = \kappa\phi(z) - z\overline{\phi'(z)} - \overline{\chi'(z)}, \tag{A.9}$$

where G is the shear modulus.

Noting that only $\chi'(z)$ appears in the expressions for the complex displacement, we can define a new function, $\psi(z)$,

$$\psi(z) = \chi'(z), \tag{A.10}$$

allowing Eq. A.9 to be rewritten as,

$$2G(u + iv) = \kappa\phi(z) - z\overline{\phi'(z)} - \overline{\psi(z)}. \tag{A.11}$$

Then, the problem is how to obtain the potentials $\phi(z)$ and $\psi(z)$. Many researchers have found the potentials for different scenarios, including the elliptical case (Maugis, 1992) in this project.

APPENDIX B

DEFORMATION FOR AN ARRAY OF CRACKS

Myer (2000) presented the excess deformation occurring if a collection of coplanar interacting cracks is subjected to load **(Fig. B.1)**. If a remote closure stress applies on an element containing a crack, the deformation, ΔL, at a large distance from the crack will be larger than the deformation of an element without crack. The additional deformation due to the crack is,

$$\delta = \frac{-4\sigma_c l}{\pi G}(1-\nu)\left[\ln\cos\frac{\pi a}{2l}\right], \qquad \text{(B.1)}$$

where δ is the additional deformation, a is the major radius of the ellipse or the half length of crack, and $2l$ is the length of element. The units used in this appendix are SI units.

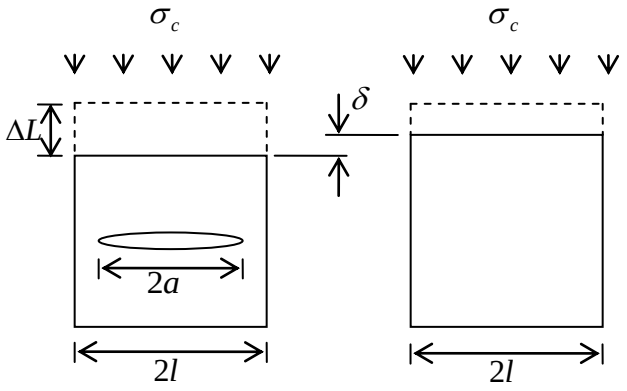

Fig. B.1—Deformation of elemental volume with and without a crack. (From Myer.)

To derive Eq. B.1, I introduce some basic concepts of fracture mechanics. The Griffith-Irwin theory (Griffith, 1921; Irwin and Kies, 1952) made use of energy rate analysis to approach crack problems. The total elastic energy available per unit increase in crack surface area is denoted by *Q*. Physically, *Q*, is "the energy made available for the crack extension processes at the crack tip as a result of the work from displacements of loading forces and/or reductions in strain energy in a body accompanying a unit increase in crack area" (Tada et al., 2000). For the linear elastic case, the expression of *Q* (Irwin and Kies, 1952) is,

$$Q = \frac{\partial U_T}{\partial A_a}, \tag{B.2}$$

where U_T is the total strain energy, and A_α is the area of a crack. With Castigliano's theorem, certain displacement is in the form of Eq. B.3 according to the Appendix B of the handbook by Tada et al. (2000),

$$\Delta L = \frac{\partial U_T}{\partial P} = \frac{\partial U_n}{\partial P} + \frac{\partial}{\partial P}\int_0^{A_a} Q dA, \tag{B.3}$$

where $P = 2l\sigma_c$. In the expression above, U_n is the strain energy without crack, and ΔL is the total deformation. Thus, the additional deformation due to the cracks is,

$$\delta = \frac{\partial}{\partial P}\int_0^{A_a} Q dA. \tag{B.4}$$

The total elastic energy, *Q*, is the summation of energy for three modes shown in **Fig. B.2**,

$$Q = Q_I + Q_{II} + Q_{III}. \tag{B.5}$$

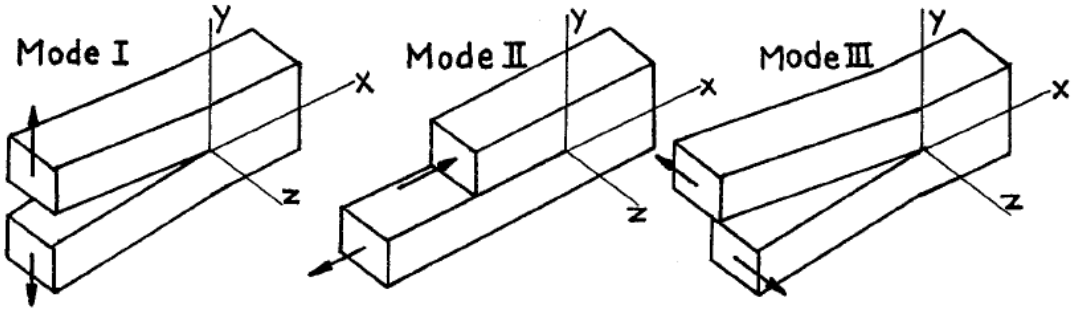

Fig. B.2—Basic modes of crack surface displacements. (From Tada.)

With the plane strain assumption, the elastic energy for each mode is,

$$Q_I = \frac{(1-\nu^2)K_I^2}{E}, \tag{B.6a}$$

$$Q_{II} = \frac{(1-\nu^2)K_{II}^2}{E}, \tag{B.6b}$$

$$Q_{III} = \frac{(1+\nu)K_{III}^2}{E}, \tag{B.6c}$$

where K_I, K_{II}, and K_{III} are the crack tip stress intensity factors for three modes. Their specific expressions for a collection of cracks are,

$$K_I = \sigma_c \sqrt{2l \tan\left(\frac{\pi a}{2l}\right)}, \tag{B.7a}$$

$$K_{II} = \tau \sqrt{2l \tan\left(\frac{\pi a}{2l}\right)}, \tag{B.7b}$$

$$K_{III} = \tau_l \sqrt{2l \tan\left(\frac{\pi a}{2l}\right)}, \tag{B.7c}$$

where τ and τ_l are shear stresses for Modes II and III, respectively.

For our case, only Mode I applies because the fracture propagates normally to the minimum in-situ stress. Therefore, substitution of Eq. B.7a and B.6a into Eq. B.5 leads to Eq. B.8,

$$Q = Q_I = \frac{2l\sigma_c^2\left(1-\nu^2\right)}{E}\tan\left(\frac{\pi a}{2l}\right) = \frac{\sigma_c^2 l(1-\upsilon)}{G}\tan\left(\frac{\pi a}{2l}\right). \qquad \text{(B.8)}$$

Substitution of Eq. B.8 into Eq. B.4 yields,

$$\begin{aligned}
\int_0^{A_a} QdA &= \int_{-a}^{a} \frac{\sigma_c^2 l(1-\nu)}{G}\tan\left(\frac{\pi a}{2l}\right)da \\
&= \frac{\sigma_c^2 l(1-\nu)}{G}\frac{2l}{\pi}\int_{-a}^{a}\tan\left(\frac{\pi a}{2l}\right)d\left(\frac{\pi a}{2l}\right) \\
&= -\frac{2\sigma_c^2 l^2(1-\nu)}{\pi G}\ln\left[\cos\left(\frac{\pi a}{2l}\right)\right]_{-a}^{a} \\
&= -\frac{2\sigma_c^2 l^2(1-\nu)}{\pi G}\left\{\ln\left[\cos\left(\frac{\pi a}{2l}\right)\right]_{-a}^{0} + \ln\left[\cos\left(\frac{\pi a}{2l}\right)\right]_{0}^{a}\right\} \\
&= -\frac{2\sigma_c^2 l^2(1-\nu)}{\pi G}\left\{2\ln\left[\cos\left(\frac{\pi a}{2l}\right)\right]_{0}^{a}\right\} \\
&= -\frac{4\sigma_c^2 l^2(1-\nu)}{\pi G}\ln\left[\cos\left(\frac{\pi a}{2l}\right)\right] \\
&= -\frac{P^2(1-\nu)}{\pi G}\ln\left[\cos\left(\frac{\pi a}{2l}\right)\right] \qquad . \qquad \text{(B.9)}
\end{aligned}$$

Then, the additional deformation is not difficult to show in Eq. B.10, which is the same as Eq. B.1,

$$\delta = \frac{\partial}{\partial P}\int_0^{A_a} Q dA = \frac{\partial}{\partial P}\left\{-\frac{P^2(1-\nu)}{\pi G}\ln\left[\cos\left(\frac{\pi a}{2l}\right)\right]\right\}$$
$$= -\frac{2P(1-\nu)}{\pi G}\ln\left[\cos\left(\frac{\pi a}{2l}\right)\right] \quad . \qquad \text{(B.10)}$$
$$= -\frac{4\sigma_c l}{\pi G}(1-\nu)\ln\left[\cos\left(\frac{\pi a}{2l}\right)\right]$$

Taking the leading terms in the expansion of the trigonometric and natural logarithm functions gives, for $l >> a$,

$$\cos\left(\frac{\pi a}{2l}\right) \cong 1 - \frac{1}{2}\left(\frac{\pi a}{2l}\right)^2 = 1 - \frac{\pi^2 a^2}{8l^2}, \qquad \text{(B.11)}$$

$$\ln\left[\cos\left(\frac{\pi a}{2l}\right)\right] \cong \ln\left(1 - \frac{\pi^2 a^2}{8l^2}\right) \cong -\frac{\pi^2 a^2}{8l^2}. \qquad \text{(B.12)}$$

Thus, if the cracks do not interact, that is $l >> a$, we approximate the additional deformation as,

$$\delta = -\frac{4\sigma_c l}{\pi G}(1-\nu)\left(-\frac{\pi^2 a^2}{8l^2}\right) = \frac{\sigma_c \pi a^2 (1-\upsilon)}{2Gl}. \qquad \text{(B.13)}$$

Distributing the volumetric deformation over the length of a crack yields the average displacement of the crack surfaces, or crack closure,

$$\bar{v} = \frac{2l\delta}{2a} = \frac{l}{a}\delta, \qquad \text{(B.14)}$$

where $\bar{v}$ is the average crack closure.

The cracks caused by acid fracturing treatment are of varying size. For using the analytical solution discussed above, the average crack half-length, $\bar{a}$, is defined by,

$$\bar{a} = \frac{\sum_{i=1}^{n} a_i}{n}, \tag{B.15}$$

where n is the number of cracks over the entire length, L. Then the contact ratio, α_c, is,

$$\alpha_c = 1 - \frac{\sum_{i=1}^{n} 2a_i}{L}. \tag{B.16}$$

Rewriting Eq. B.10 and Eq. B.13 yields the average additional displacement, $\bar{\delta}$, in terms of average crack half-length and contact ratio,

$$\bar{\delta} = \frac{4\sigma_c \bar{a}}{\pi G} \frac{\nu - 1}{1 - \alpha_c} \left\{ \ln \left[\cos \frac{(1 - \alpha_c)\pi}{2} \right] \right\}, \tag{B.17}$$

$$\bar{\delta} = \frac{\pi \sigma_c \bar{a}}{2G} (1 - \nu)(1 - \alpha_c). \tag{B.18}$$

Notice that the constants in Eq. B.16 and Eq. B.18 are different from the constants in the original publication by Myer (2000). The constants given here are correct ones. Finally, we have the average crack closure with respect to contact ratio shown in Eq. B.19,

$$\bar{v} = \frac{\bar{\delta}}{1 - \alpha_c}. \tag{B.19}$$

APPENDIX C

COMPUTATIONAL PROCEDURE OF MODELS

The new correlations give the general scenario of the conductivity calculation for acid fracturing. When we consider some particular cases with unusual conditions, the simulation programs will yield the better results than the correlations. Thus, I summarize the computational procedure as follows. It consists of several modules that perform different functions. If they can be combined and organized in one package, I believe it would be more helpful in practice.

As a whole project, the simulation includes two parts: the acid transportation by Mou and the fracture closure in this study. Mou (2009) gave an input example in the Appendix D of his dissertation. It defines the calculation domain, acid properties, pumping schedule, reservoir properties, and so on. In addition, the closure model requires the rock strength as inputs. Both Young's modulus and rock embedment strength are used in the program. The rock embedment strength is for the calculation of base conductivity. If only one of the rock strength properties is available, the relationship between them mentioned previously can give an estimate of the other. The default value of another rock property, Poisson's ratio, is 0.3 in the program. It can be set differently for some specific cases also.

The procedure shown in **Fig. C.1** includes Mou's models. The distributions of permeability and mineralogy serve as the inputs to the acid flow simulation that outputs the width profile after acidizing. The next conductivity module provides the initial

conductivity and fracture width analysis. The description of these modules can be found in the Appendix D of Mou's dissertation.

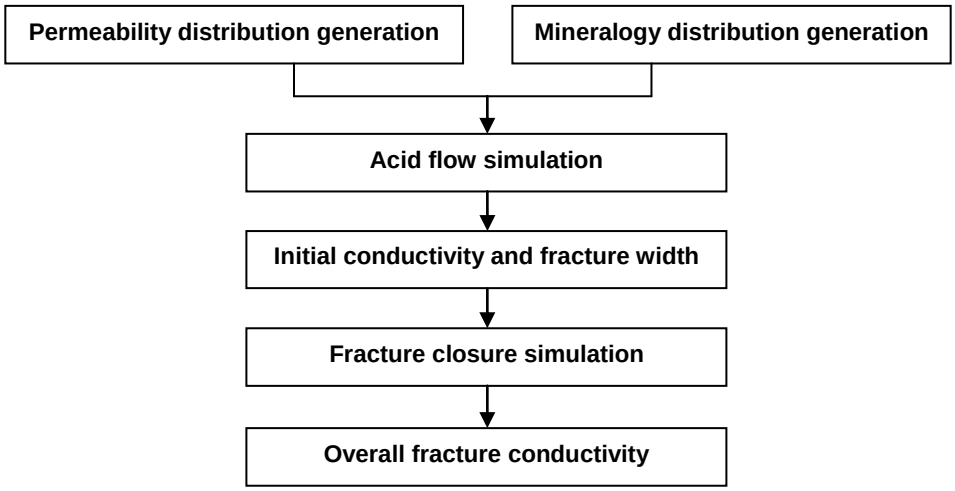

Fig. C.1—Computational procedure of models.

With the width profile produced by Mou's models, the fracture closure module simulates the rock deformation process and yields the fracture width profile after closure. Based on the initial conductivity, fracture width analysis, and width profile after closure, the last module calculates the base conductivity and predicts the overall fracture conductivity.

All of the six modules in Fig. C.1 are written in C language. It would not be difficult to combine them and develop a package. The main challenge is to incorporate the GSLIB that is another package Mou used to generate spatially correlated random number by specifying correlation length in two directions. They serve as inputs for both permeability and mineralogy distribution generation.

APPENDIX D

3D SIMULATION OF ELLIPSE CLOSURE

The closure model in this study uses the analytical methods for ellipse closure to approach every cross-section of an acid fracture. The combination of the results from every cross-section yields the width profile after closure. And the effects among the cross-sections are neglected. They may not be, though, significant because the rock properties are correlated laterally. Fully 3D simulation of deformation between two rough surfaces can account for the effects, and the corresponding width profile can be more accurate. I try some simple cases for ellipse and summarize them as follows.

I employed some commercial software packages according to our current conditions. Solidworks™ is used to generate geometry. Patran™ reads output from Solidworks™ and generates geometry models, elements, material properties, and loads. Next, Abaqus™ reads output from Patran™ and performs computation. Finally, Patran™ reads outputs from Abaqus™ and performs analysis. The procedure is shown below in **Fig. D.1**.

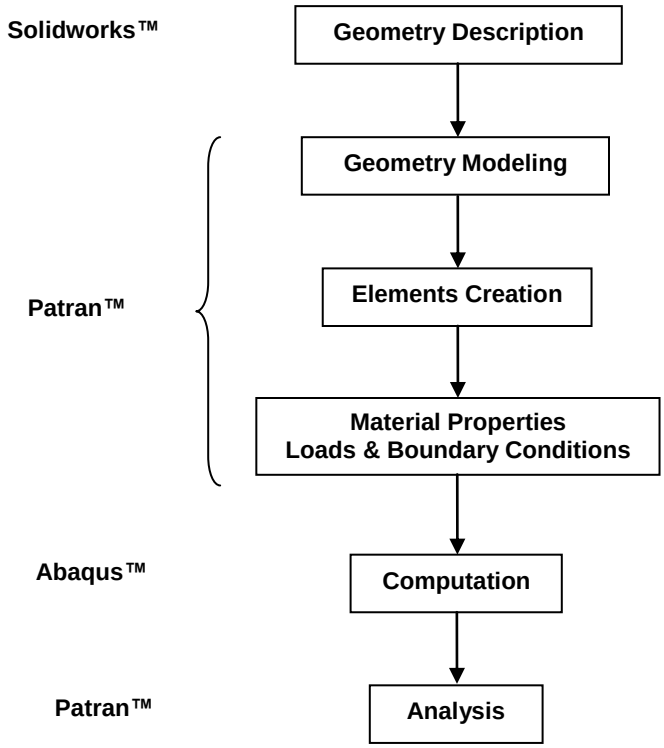

Fig. D.1—Procedure of 3D simulation.

The try starts with a simple case: an ellipse in rock mass under closure stress. As shown in **Fig. D.2**, the size of the rock is 1 meter by 1 meter by 1 meter. And the ellipse has a=0.1 meters (m), b=1 millimeters (mm). Because the geometry is symmetric, the simulation on half of the original one (**Fig. D.3**) saves the computational time without sacrificing any precision.

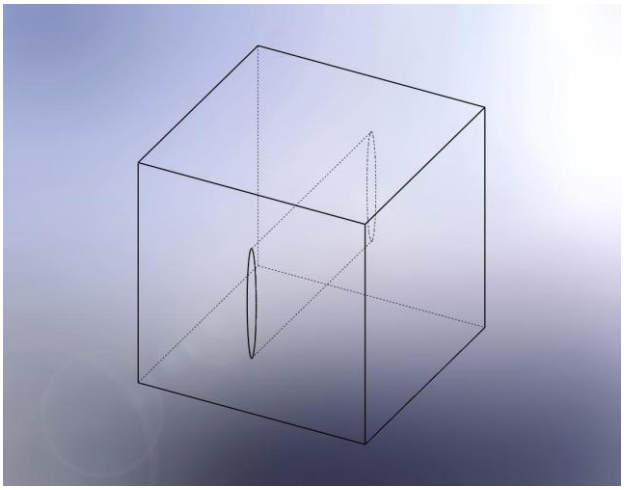

Fig. D.2—Ellipse in rock mass.

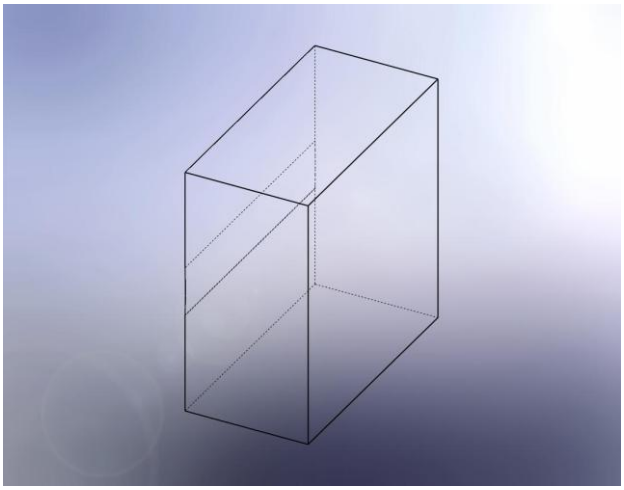

Fig. D.3—Simulation on half of original geometry.

After the generation of the geometry, the elements are created and the rock properties are defined. As shown in **Fig. D.4**, the number of elements is 3879; the number of nodes is 6056; the Young's modulus is 7×10^9 Pa (10^6 psi); the Poisson's ratio is 0.3; the closure stress is 20 MPa (2,900 psi).

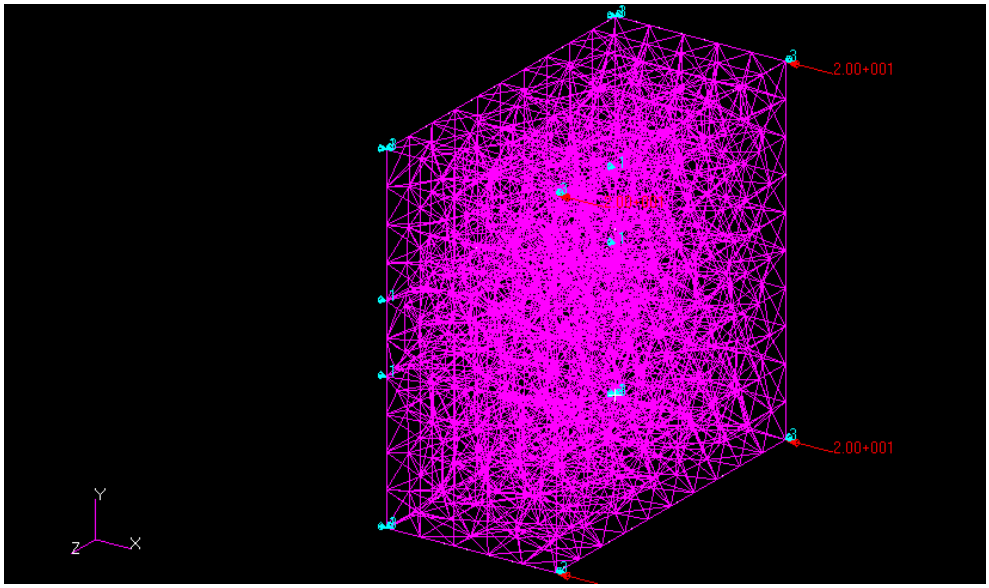

Fig. D.4—Definition of elements, loads, and properties.

After the computation by Abaqus™, Patran™ analyzes the output and plots the contour as shown in **Fig. D.5**. The output file of data gives the deformation for every node. For example, the deformation of the node at the minor semi axis is 0.5157 mm.

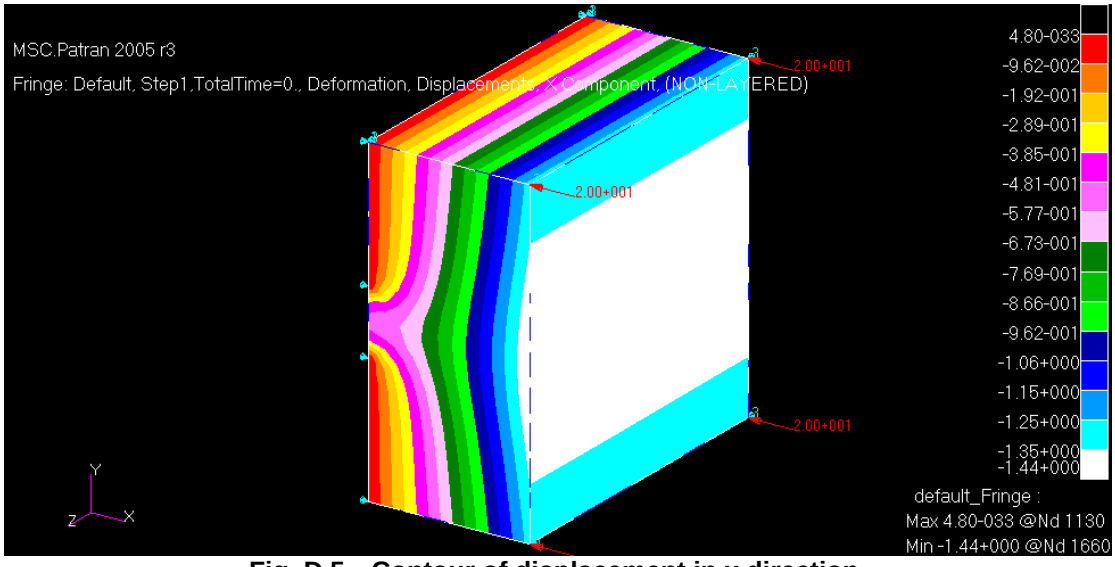

Fig. D.5—Contour of displacement in x direction.

In order to increase the precision, I can refine the local grids around the ellipse. That is even more important if we cope with rough surfaces in the future. I still use the same example above with local grid refinement. The geometry consists of two parts shown in **Fig. D.6**. The elements are created separately for each part (**Fig. D.7**). The grids around the ellipse are finer than the grids far from the ellipse. The number of elements is 3225. The number of nodes is 4882. Both of these numbers are less than the previous example. Other than those, the rock properties and loads are the same.

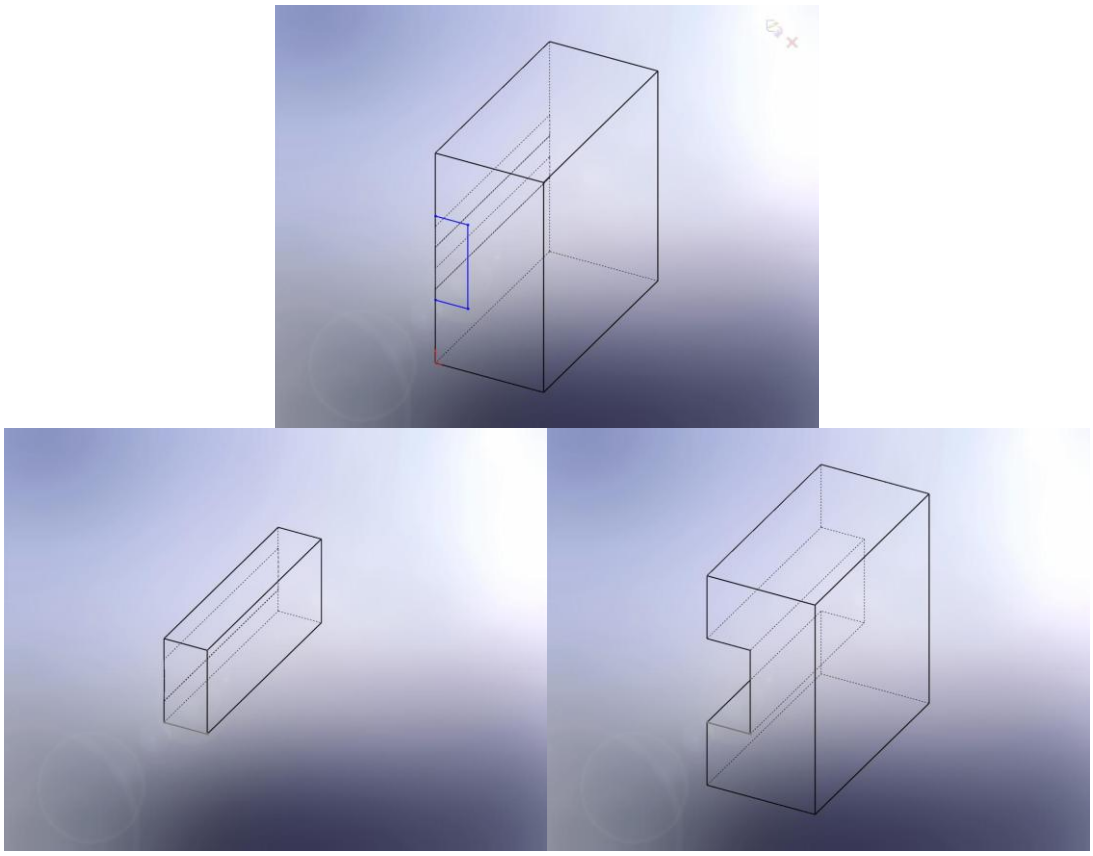

Fig. D.6—Geometry for local grid refinement.

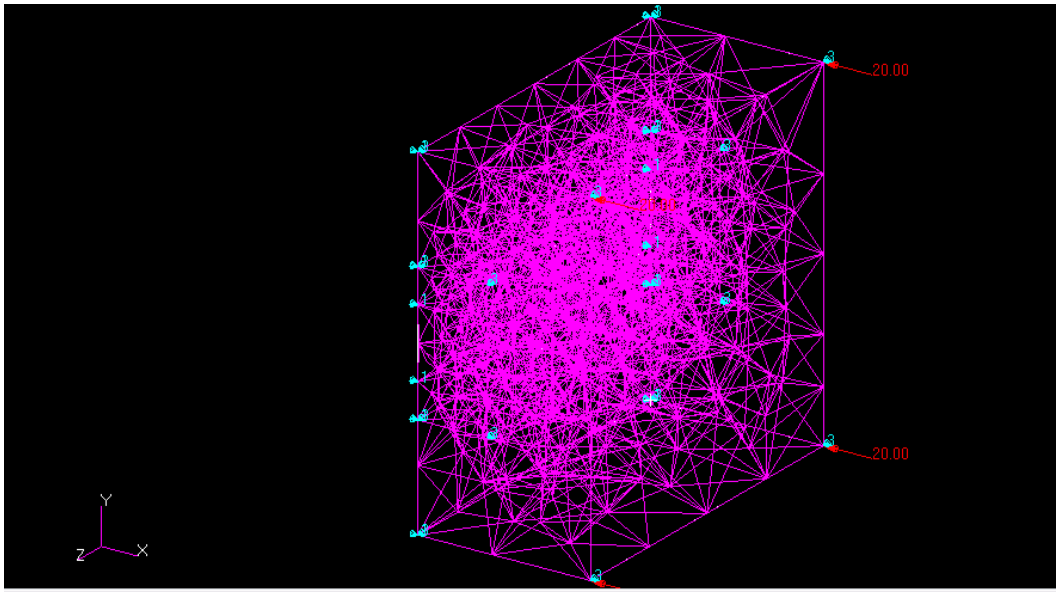

Fig. D.7—Definition of elements, loads, and properties.

The contour of the displacement in *x* direction is shown in **Fig. D.8**. The deformation of the node around the minor semi axis is 0.5227 mm.

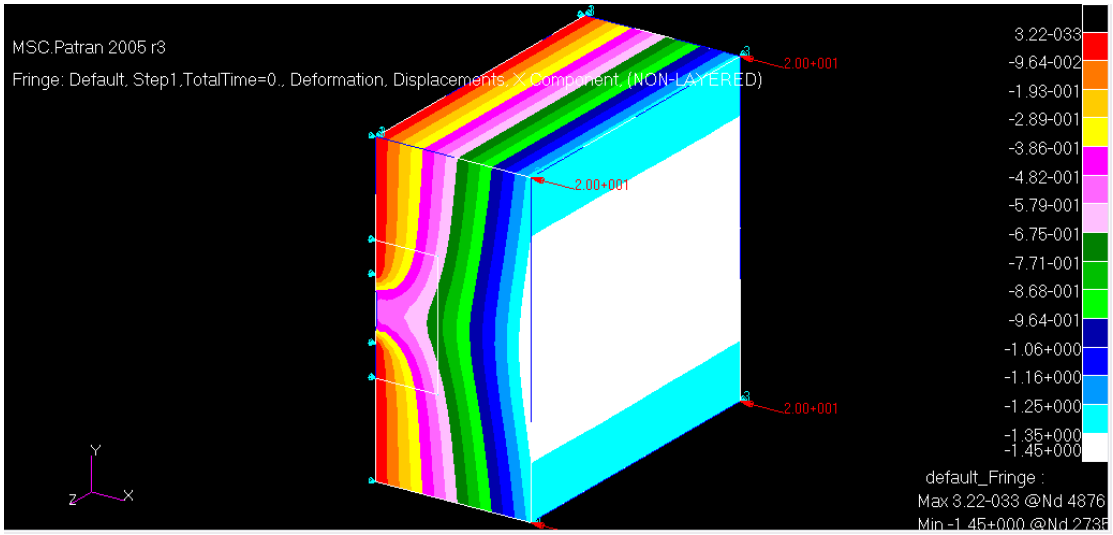

Fig. D.8—Contour of displacement in x direction.

The last example investigates the effect between two ellipses. **Fig. D.9** shows the geometry. Two ellipses have the same size with a=50 mm, b=0.5 mm. The center-to-center distance is 200 mm. I also conduct the local grid refinement around the two ellipses.

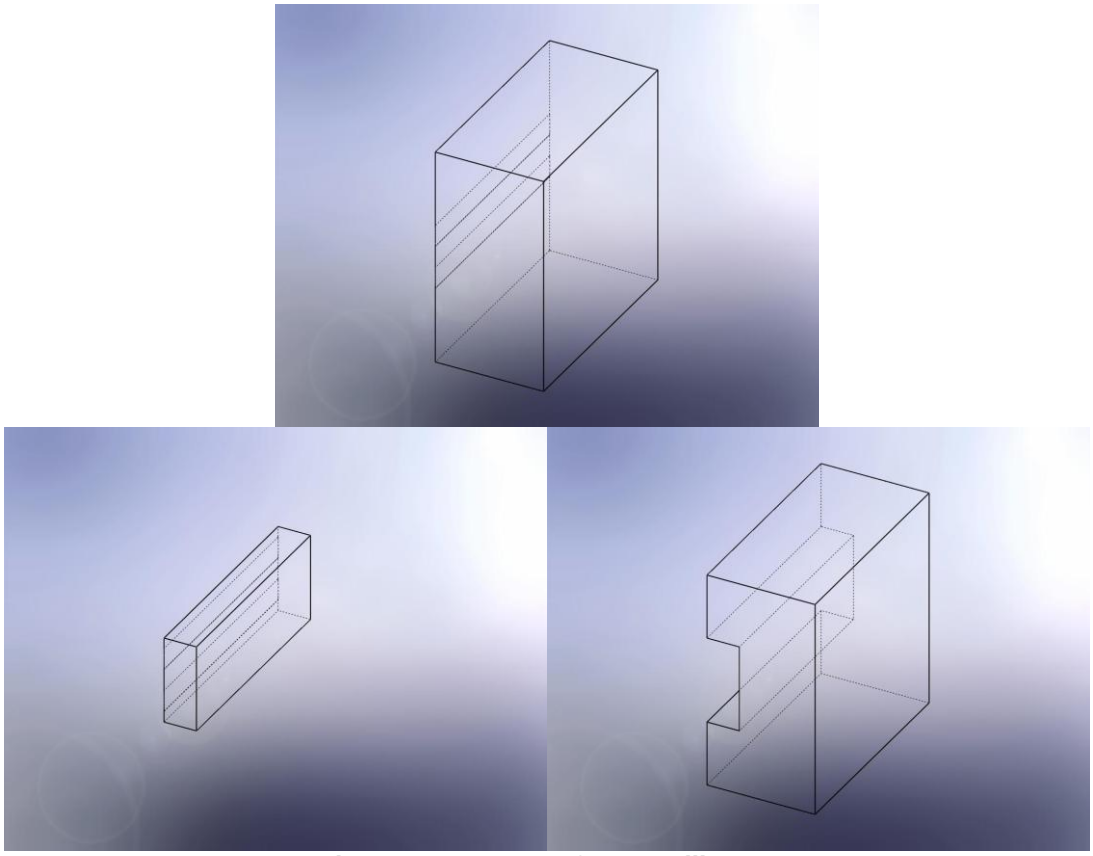

Fig. D.9—Geometry for two ellipses.

The geometry modeling, element creation, rock properties, loads, and boundary conditions are set up similarly in Patran™. After the simulation, the contour of the displacement in x direction is shown in **Fig. D.10**. These two ellipses are exactly the

same. Thus, the deformation of the node around the minor semi axis for either ellipse is 0.2155 mm.

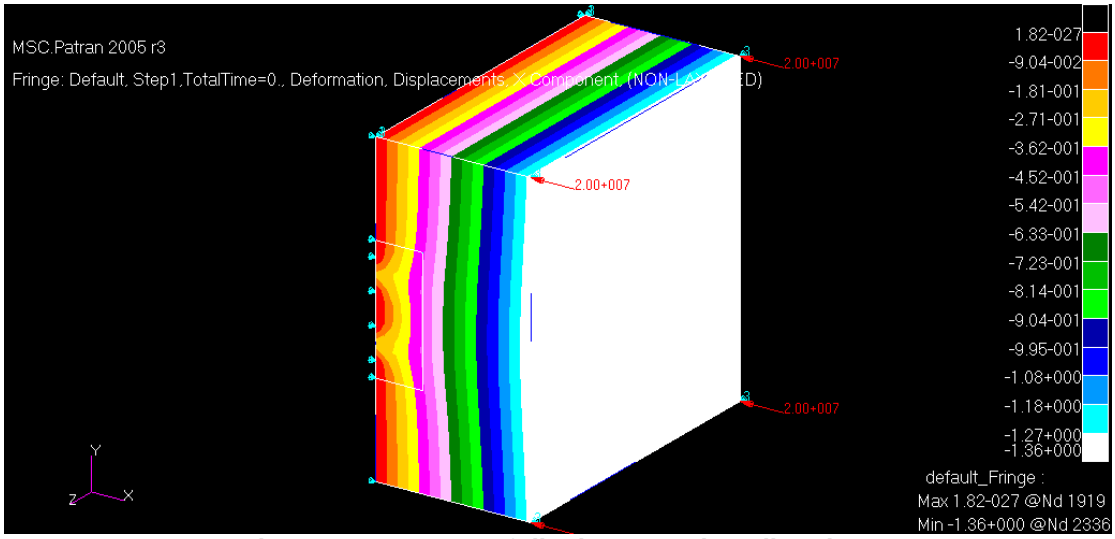

Fig. D.10—Contour of displacement in x direction.

To evaluate these 3D simulations, I compare the results with the analytical ones for regular geometry. From the previous discussion, the analytical solution for a single ellipse is,

$$v = \frac{c(1-\nu)}{2G}\sigma_h \sin\eta\left(2\cosh\xi_0 + \sinh\xi_0\right). \qquad \text{(D.1)}$$

And the analytical solution for multiple ellipses is,

$$v = \frac{-4\sigma_c l}{\pi G}(1-\nu)\left[\ln\left(\cos\frac{\pi a}{2l}\right)\right]. \qquad \text{(D.2)}$$

The symbols in the equations have been defined in previous chapter.

Substitution of the proper parameters into the equations can yield the displacement at the minor semi axis for the examples. Comparison with the numerical

results is presented in **Table D.1**. Basically, the numerical results have good agreement with the analytical ones. Especially when the grids are refined, the precision is improved effectively.

TABLE D.1—COMPARISON BETWEEN ANALYTICAL AND NUMERICAL RESULTS

	Single Ellipse	Grid Refinement	Multiple ellipses
Analytical	0.5226	0.5226	0.229
Numerical	0.5157	0.5227	0.2155

The examples for ellipses are simple and straightforward because the geometry is regular. If 3D simulation applies on rough surfaces of an acid fracture, many challenges still exist. First, the topology for width profiles is difficult. The output of the acidizing simulator provides only the width for every node on the fracture surface. When the geometry is generated, the topology from points to surfaces needs further study. Secondly, the rough surface requires very fine grids. Local grid refinement increases the precision in the example above. But much more grids will be necessary for rough surfaces with thousands of nodes. Even if enough grids can be generated, it is still a big challenge for computational capacity. At least, our current condition (the supercomputer facility for students in Texas A&M University) in these examples is not able to deal with this problem. My recommendation is to conduct the 2D numerical simulation on one cross-section of a fracture next. Compare the results with the present analytical models and determine the necessity and methodology for fully 3D simulation in the future.

VITA

Name: Jiayao Deng

Email Address: dengjy@gmail.com

Education: B.S., Mechanical Engineering, Tsinghua University, China, 2003
M.S., Mechanical Engineering, Tsinghua University, China, 2006
Ph.D., Petroleum Engineering, Texas A&M University, 2010

TAMU Address: Department of Petroleum Engineering
c/o Dr. Hill or Dr. Zhu
Texas A&M University
College Station, TX 77843-3116